

THREE-DIMENSIONAL  
ELECTRONIC SURFACES

PAI-HUI IRIS HSU

A DISSERTATION  
PRESENTED TO THE FACULTY  
OF PRINCETON UNIVERSITY  
IN CANDIDACY FOR THE DEGREE  
OF DOCTOR OF PHILOSOPHY

RECOMMENDED FOR ACCEPTANCE  
BY THE DEPARTMENT OF  
ELECTRICAL ENGINEERING

NOVEMBER 2003

© Copyright by PAI-HUI IRIS HSU, 2003.

All rights reserved.

# Abstract

Novel large-area electronics, such as electronic paper, sensor skin, and electrotiles, requires building electronic devices on flexible and deformable substrates. Substrates such as organic polymers and stainless steel foils can be deformed into arbitrary shapes, but inorganic semiconductor device materials, such as amorphous silicon and silicon nitride, are brittle, and crack easily when substrates are deformed. Therefore, it is desirable to reduce the strain in such device structure on deformable substrates, and to further understand the relationship between the electrical performance of the devices and the applied mechanical strain for strain below the point where failure occurs.

In this thesis, we explore the ability to plastically deform thin film semiconductor structures on deformable substrates to spherical cap shapes without cracking the semiconductor layers. To achieve electronics on a spherical dome, thin-film transistors were first fabricated with conventional processes in islands on a flat polyimide substrate. Next, the substrate was plastically deformed into a spherical dome. With this approach, the strain in the device island was drastically reduced. Interconnects between the device island could be made by lift-off methods. Other interconnect schemes such as direct printing were also discussed. The results demonstrate that the concept of stiff circuit islands fabricated on deformable foil substrates is a promising approach to electronics on surfaces with arbitrary shapes.

# Acknowledgement

I would like to take this opportunity to thank my advisor, Prof. Sturm, who guided me through graduate school and challenged me constantly to be an independent researcher. I deeply appreciated his help during these years. I would also like to thank Prof. Wagner, Dr. Gleskova, and Prof. Suo. I learned so much from this project, and I am glad that I had the chance to be a part of it. Dr. Min Huang contributed greatly on the planar islands, and Dr. Zhichen Xi did extensive work on the mesa islands. I sincerely thank them for their help in the mechanical section of the project.

I would like to gratefully acknowledge Princeton University for receiving the Gordon Wu Fellowship and Princeton Plasma Physics Lab for a student fellowship. I would also like to thank I-chun Cheng, Amanda Cheng, Ke Long, and the rest of Prof. Sturm's group. I am very grateful for their friendship. Also, I would like to thank my parents and my sister for their love and encouragement. I couldn't accomplish my goal without their support. Finally, I would like to thank my husband, David Brooks, for his patience and assistance from the first day we met. I truly cherish his presence.

# Contents

<b>Abstract</b>	<b>iii</b>
<b>Acknowledgement</b>	<b>iv</b>
<b>1 Introduction.....</b>	<b>1</b>
1.1 Motivation.....	1
1.2 Challenge .....	3
1.3 Outline .....	4
<b>2 Deformable Electronics .....</b>	<b>6</b>
2.1 Introduction.....	6
2.2 Cylindrical Deformation.....	7
2.3 Spherical Deformation.....	10
2.4 Chapter Summary .....	15
<b>3 Spherical Deformation of the Thin Foil Substrate.....</b>	<b>16</b>
3.1 Introduction.....	16
3.2 Steel Substrates .....	17
3.3 Polyimide Substrates .....	19
3.4 Strain Distribution in the Substrates .....	22
3.5 Chapter Summary .....	27
<b>4 Amorphous Silicon Islands on Spherical Domes .....</b>	<b>28</b>
4.1 Introduction.....	28
4.2 Island Concept .....	29

4.2.1 Planar Device Islands on Polyimide Substrates .....	32
4.2.2 Mesa Device Islands on Polyimide Substrates .....	37
4.3 Strain Distributions in Island Structures .....	39
4.3.1 Modeling of Strain Distribution in the Islands .....	39
4.3.2 Strain Distribution in Planar Islands .....	42
4.3.3 Strain Distribution in Mesa Islands .....	48
4.4 Chapter Summary .....	53
<b>5 Thin Film Transistors on Spherical Domes .....</b>	<b>54</b>
5.1 Introduction .....	54
5.2 Properties of Thin-film Transistor .....	55
5.3 Thin-film Transistor Fabrication .....	59
5.4 Amorphous Silicon Thin-Film Transistors on Spherical Domes .....	65
5.4.1 TFTs on Planar Islands .....	65
5.4.2 TFTs on Mesa Islands .....	70
5.5 Discussion of TFT Electrical Performance under Mechanical Strain .....	76
5.5.1 Amorphous Silicon TFTs under Uniaxial Strain .....	76
5.5.2 Amorphous Silicon TFTs under Biaxial Strain .....	78
5.5.2.1 Planar Devices and Tensile Strain .....	79
5.5.2.2 Mesa Devices and Compressive Strain .....	81
5.5.2.3 Elastic Deformation of TFTs under Biaxial Strain .....	83
5.6 Chapter Summary .....	85
<b>6 Circuits on Spherical Domes .....</b>	<b>86</b>
6.1 Introduction .....	86
6.2 Interconnect Patterning by Lift-off Process Using Deformed Photoresist .....	88
6.3 Other Schemes for Interconnect Fabrication .....	91
6.3.1 X-Y crossovers .....	91
6.3.2 Direct Printing onto Spherical Surfaces .....	93
6.3.3 Stretchable Interconnects .....	94
6.4 Chapter Summary .....	96

<b>7 Conclusion .....</b>	<b>97</b>
7.1 Summary.....	97
7.2 Future Work: Active Matrix Display or Sensor Arrays on Arbitrary Shaped Surfaces.....	99
<b>Bibliography .....</b>	<b>103</b>
<b>Appendix A: Kapton<sup>o</sup> Polyimide Substrate Preparation .....</b>	<b>111</b>
<b>Appendix B: Recipes for Thin-Film Transistor Fabrication .....</b>	<b>115</b>
<b>Appendix C: Back Support for Spherical Dome Electrical Measurement.....</b>	<b>118</b>
<b>Appendix D: Publications and Presentations Resulting from this Work .....</b>	<b>120</b>

## Introduction

### 1.1 Motivation

The applications of traditional large-area electronics, such as displays, are limited by the fact that glass substrates are rigid and easily breakable. Future large-area electronics should be more lightweight and “portable”. A straightforward example would be a flat panel display that could be rolled up like a traditional paper map [1-3]. A more complex example is an artificial “sensitive skin”, which is a large-area flexible array of sensors with data-processing capabilities. It could be used to cover the entire surface of a machine or even a part of a human body for applications such as a medical monitoring device [4]. Undoubtedly, there are enormous drivers for curved products on flexible substrates.

Nearly all work to date on curved substrates has focused on rolling the substrate into a cylindrical shape [1-3, 5-6]. For such cylindrical deformation, the mechanical strain in the devices can be kept low simply by reducing the substrate thickness. Newer concepts, however, require the fabrication of electronics on "non- developable" surfaces,



(a)



(b)



(c)



(d)

Fig. 1.1 Examples of flexible electronics: (a) Electronic ink display on steel (E Ink Corp.) [1], (b) OLED display on plastic substrate (Universal Display Corp.) [2], (c) Pentacene TFTs on plastic substrate (Penn State Univ.) [3], and (d) Sensitive skin (Motorola Advanced Technology Center) [4]

such as a spherical cap, which can be made from a flat sheet only by plastic deformation (permanent deformation). An application of such spherical deformation is image sensor arrays. For focal plane array imagers with a large field-of-view, the optics to provide a spherically curved focal “plane” array is far smaller than that required to provide a conventional flat focal plane, translating into a smaller, lighter, and lower cost system [7]. In this thesis, we concentrate on how to achieve electronics on three-dimensional electronic surfaces such as a spherical dome. Deformation of a flat sheet to a spherical shape is inherently more difficult than to a cylindrical one: In spherical deformation the strain is determined by the shape and cannot be reduced by thinning the substrate. In the following chapters, we will present the first amorphous silicon thin-film transistors (TFTs) and circuits on a spherical dome. We will also discuss the relationship between the device electronic characteristics and mechanical strain in semiconductor layers.

## 1.2 Challenge

To achieve flexible electronics, current semiconductor device fabrication processes designed for rigid substrates have to be modified. One approach towards electronics on curved surfaces involves direct fabrication on curved or spherical surfaces [8]; however, it is difficult to adapt conventional process tools to this approach. Another approach is to first fabricate devices on a silicon wafer and dice the finished wafer into small “tiles” [9]. The device tiles are then bonded to flexible substrates such as a PMMA (Polymethylmethacrylate) film. In this method, the interconnects between individual tiles are complicated, and such a “cut-and-paste” approach is not ideal for future mass production. Therefore, our approach here is to fabricate devices on flat deformable substrates (plastic or stainless steel foils), then permanently deform the final device

structure into a spherical dome. This approach has the benefit of relatively straightforward device fabrication on a planar surface, but the deformation can damage the fabricated components or interconnects. We will demonstrate how to overcome these difficulties and present various fabrication techniques including direct printing to achieve interconnects on spherical-shape substrates.

From the previous discussion, we learn that novel large-area electronics requires building electronic devices on flexible and deformable substrates. Substrates, such as organic polymers and stainless steel foils, can be deformed into arbitrary shapes, but inorganic semiconductor device materials, such as amorphous silicon and silicon nitride, are brittle and crack easily when substrates are deformed. Therefore, it is essential to reduce the strain in such device structures on deformable substrates. We will discuss how to achieve permanent, plastic deformation in the substrates, without exceeding fracture or buckling limits in the device materials in the thesis.

### 1.3 Outline

Chapter 2 will discuss the applications for the deformable electronics and explain the fundamentals of the cylindrical and spherical deformation. Chapter 3 focuses on how we deform a flexible substrate into a spherical-cap shape. Chapter 4 demonstrates that by patterning uniform layers of brittle semiconductor materials into islands, the mechanical strain in the device layers can be reduced; therefore, devices on single islands can be achieved. Chapter 5 describes amorphous silicon TFTs in these islands and discusses the electrical performance of the TFTs due to applied mechanical strain. Chapter 6 describes how to achieve interconnects between islands on a spherical dome. Chapter 7 will

summarize the major contributions of this thesis, offer conclusions, and discuss areas of future research.

# Deformable Electronics

## 2.1 Introduction

The conventional goal of the semiconductor industry is to make things small. However, there is an emerging market for “macroelectronics,” which can be defined as large-area and low-cost electronics for real world interfaces such as flat panel displays, large-area sensor arrays (e.g. X-ray imaging plates), MicroElectroMechanical Systems (MEMS) arrays, etc. Current generations of these products are made on glass substrates using amorphous or polycrystalline semiconductor technology. For future products, it is highly desirable that they be lightweight, flexible, and rugged. For example, bendable displays made on thin stainless steel substrates are of great interest for applications in electronic newspapers and smart identity cards [10], and flexible tactile sensor skin made on polyimide substrates has great potential in medical and industrial applications [11]. These applications require stretching and relaxing the flexible substrates multiple times. In this thesis we focus on deforming a flat sheet into a spherical dome. The deformation is permanent, and the substrate will be deformed only once. The major challenge involves contending with the large strain due to extreme deformation that will

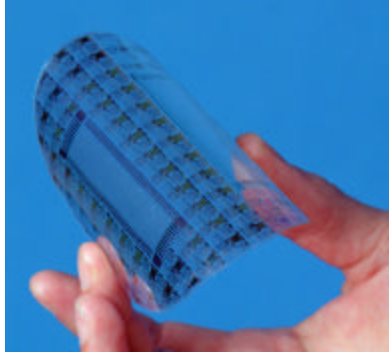
crack inorganic materials such as silicon or metal interconnect. In this chapter, we will examine the relationship between the deformed shape and the strain in the substrate.

## 2.2 Cylindrical Deformation

Most of the work to date on flexible substrates has focused on cylindrical deformation of thin film devices on polymer or metal foils [5-6,12-16] (Fig. 2.1 (a), (b)). For cylindrical deformation, the strain is one-dimensional. The semiconductor films on the inside of the deformed surface are in compression and those on the outside are in tension, while there exists a plane between these two with no strain (neutral plane) [6]. Assuming the film thickness is negligible and the neutral plane is at the mid-surface of the substrate, the magnitude of strain in the surfaces is given by

$$\mathbf{e}_{uniaxial} = \frac{t}{2r} \quad (2.1)$$

where  $t$  is the substrate thickness, and  $\rho$  is the radius of curvature (Fig. 2.2). Since the surface strain can be decreased by reducing the substrate thickness, tight radii of curvature can be achieved simply by using thinner substrates. Previous work [12,16] has demonstrated that transistors on thin metal or plastic foil substrates can be rolled around a cylinder down to  $\sim 2$  mm radius of curvature with no adverse effects. In fact, crystalline silicon wafers can be cylindrically deformed as well provided the substrate is thin. For example, Fig. 2.1 (c) shows a 10- $\mu\text{m}$ -thick crystalline silicon wafer bent into a cylindrical shape without fracture. Though the displacement is large, the strain in the thin silicon wafer is actually very small (If the radius of curvature is 1 cm, from Eq. 1, the strain in the silicon wafer is only 0.05%, which is about the breaking limit of the silicon).



(a)



(b)



(c)

Fig. 2.1 Cylindrical deformation of flexible substrates: (a) Polyimide TFTs on polyester (Lawrence Livermore National Lab) [17]. (b) TFT on a steel substrate wrapped twice around the end of a pencil (radius of curvature = 2.5 mm) (Princeton University) [12] (c) 10- $\mu\text{m}$  thick crystalline silicon wafer bent into a cylindrical shape (Virginia Semiconductor) [18]

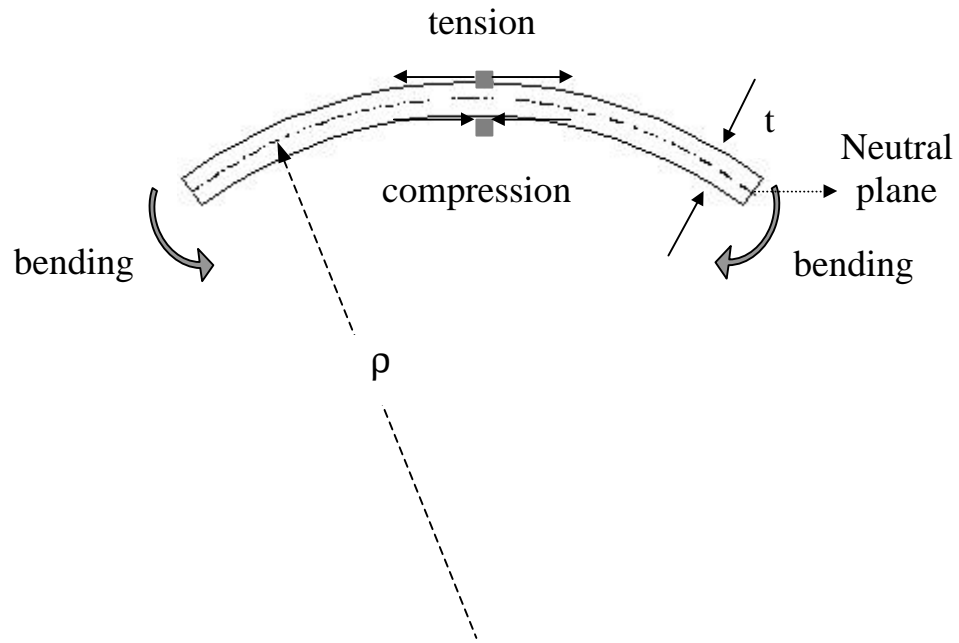


Figure 2.2 Strain distribution in a flexible substrate under cylindrical deformation.  $t$  is the thickness of the substrate, and  $\rho$  is the radius of curvature.

## 2.3 Spherical Deformation

In this thesis we report work aiming towards the permanent deformation of thin film electronics, first fabricated by conventional methods on thin foil substrates, into a spherically-shaped cap. In contrast to rolling, with spherical deformation, the surface is in tension on both the concave and convex sides of the substrate. Thus spherical deformation is fundamentally more difficult than cylindrical deformation because the deformation inherently involves stretching the substrate and devices on it, independent of the substrate thickness.

In our experiments, pressurized nitrogen is used to deform structures on thin-foil stainless steel or Kapton<sup>®</sup> E polyimide substrates, which are clamped at the edges (6 cm in diameter), into spherically-shaped caps [19] (Fig. 2.3 (a)). The average radial strain ( $\mathbf{e}_{r,avg}$ ) in a deformed substrate can easily be calculated geometrically by comparing the increase in length of the initial foil cross section to the final deformed arc (Fig. 2.3(b)):

$$\begin{aligned} \mathbf{e}_{r,avg} &= \frac{\frac{\mathbf{q}}{2} - \sin \frac{\mathbf{q}}{2}}{\sin \frac{\mathbf{q}}{2}} = \frac{\sin^{-1}\left(\frac{2Rh}{R^2 + h^2}\right) - \frac{2Rh}{R^2 + h^2}}{\frac{2Rh}{R^2 + h^2}} \\ &\approx \frac{\mathbf{q}^2}{24} = \frac{2}{3} \left( \frac{Rh}{R^2 + h^2} \right)^2 \end{aligned} \quad (2.2)$$

where  $\theta$  is the field-of-view.

For a spherical dome with 66° field-of-view, which subtends a solid-angle of one steradian, the average radial strain is 5.6%. This level of strain generally exceeds the fracture limit of inorganic device materials (< 1%) such as amorphous silicon films.

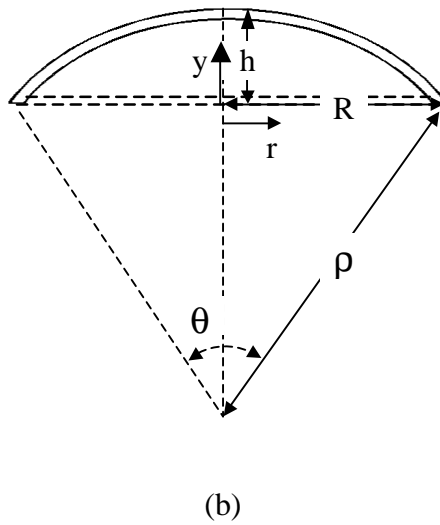
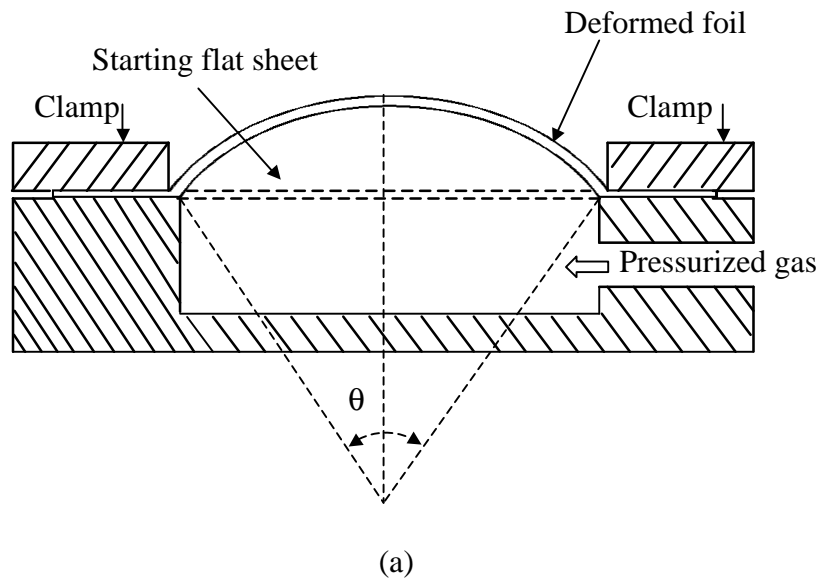


Figure 2.3 (a) Schematic diagram indicating apparatus for deforming substrates. (b) Schematic cross-section of the foil before and after deformation, where  $\theta$  is the field-of-view,  $h$  is the height of the spherical dome,  $R$  is the radius of the clamped substrate, and  $\rho$  is the radius of curvature.

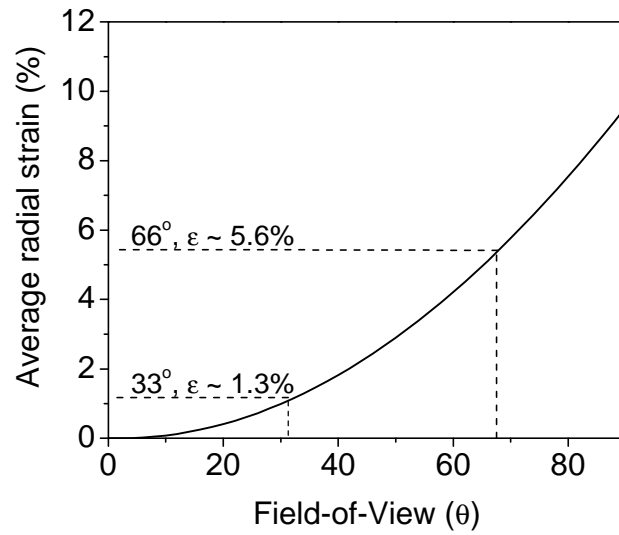
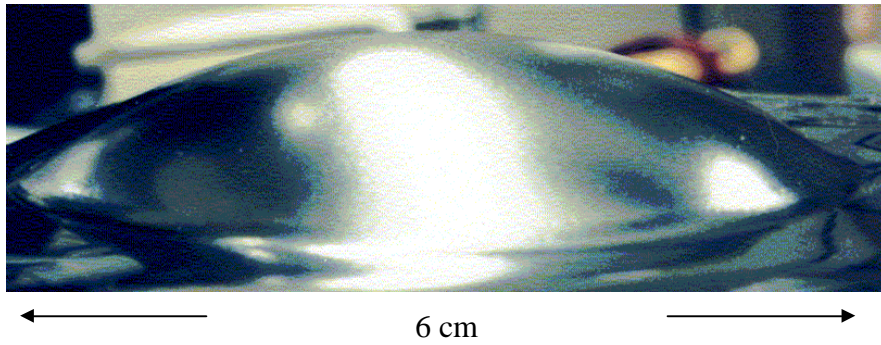


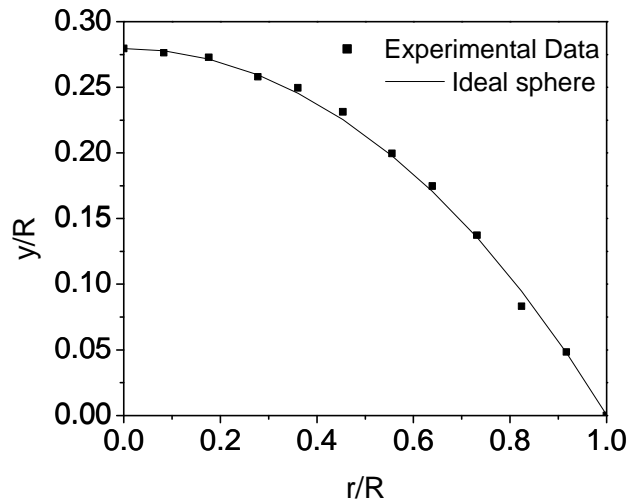
Figure 2.4 Average radial strain by geometric considerations across the foil after deformation as a function of  $\theta$ . A  $66^\circ$  field-of-view corresponds to a solid angle of one steradian.

We measured the height of deformation at the center of the foil ( $h$ ) and its radius ( $R$ ) to estimate the average radial strain in the substrate. For example, a  $66^\circ$  field-of-view spherical dome corresponds to  $h/R = 0.29$ . We use this model benchmark as a goal for most of the work in the following chapters. Fig. 2.5(a) shows a 25- $\mu\text{m}$ -thick stainless steel sheet deformed by pressurized gas up to 50 psi after pressure release. After the pressure was released, the height of the spherical dome is  $\sim 0.85$  cm ( $h/R = 0.28$ , corresponding to a  $63^\circ$  field-of-view). Figure 2.5 (b) shows the shape of the steel after pressure release, which closely matches that of an ideal spherical dome with  $63^\circ$  field-of-view. It demonstrates that pressurized gas is a viable approach to deform a flat sheet into a 3-dimensional shape.

In contrast to previous work on clamped circular membrane deflections [20-21], the substrates in our experiments were deformed plastically. Therefore, the stress-strain equations for our substrates were not linear, and the assumptions made in previous cases (the deflection was assumed to be small) were not valid [22] in our experiments. Consequently, the strain distribution in a spherically deformed sheet cannot be calculated analytically and depends on the material properties of the substrates. In the following chapters, numerical finite element modeling is used to examine the strain profile in the stainless steel or polyimide substrates.



(a)



(b)

Figure 2.5 (a) a 25- $\mu$ m-thick stainless steel sheet deformed by nitrogen pressurized up to 50 psi. Picture is taken after pressure was released. (b) Shape of such stainless steel sheet as a function of radius, with the height and radius normalized by the radius of the deformed region  $R$  (as defined in Fig. 2.3 (b)). The solid line represents an ideal spherical shape cap with the same height at the center of the cap.

## 2.4 Chapter Summary

To date, research on curved electronics has focused on the cylindrical deformation of thin film devices on polymer or metal foils. For cylindrical deformation, the strain is one dimensional and can be reduced by using thinner substrates. For applications such as electronic papers, the cylindrical deformation is usually temporary, and the substrates can be rolled up and flattened many times. In this work, the flexible substrate is deformed into a spherical cap. The deformation is permanent, and the strain in the substrate is determined by its geometry. For a spherical dome with  $66^\circ$  field-of-view, the average strain is  $\sim 6\%$  and cannot be reduced by adapting thinner substrates. This level of strain generally exceeds the fracture limit of inorganic device materials ( $< 1\%$ ), and consequently, flexible electronics on spherical caps is inherently more complicated than cylindrical deformation of rolled electronics.

# Spherical Deformation of the Thin Foil Substrates

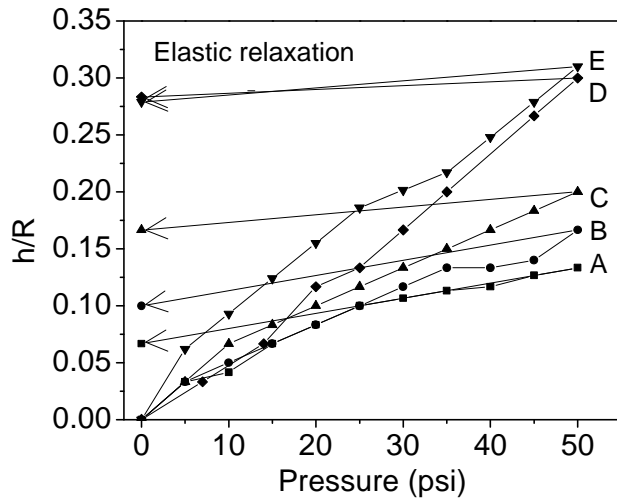
## 3.1 Introduction

In this work we seek to plastically deform a flat compliant substrate into a spherical-shaped cap. Stainless steel foils and plastic substrate are suitable candidates for this purpose. In our experiments, pressurized nitrogen is used to deform thin foil substrates, which are clamped at the edges (6 cm in diameter), into spherically-shaped caps (Fig. 2.3(a)). The *average* radial strain ( $\epsilon_{r,avg}$ ) in a deformed substrate can easily be calculated geometrically (Eq. 2.2). However, the actual strain distribution in a spherically deformed sheet cannot be calculated analytically. To better understand the strain distribution in the substrates, numerical modeling is used to examine the strain profile in the substrates in this chapter. It is done in collaboration with Dr. Min Huang (for planar islands) and Dr. Zhichen Xi (for mesa islands).

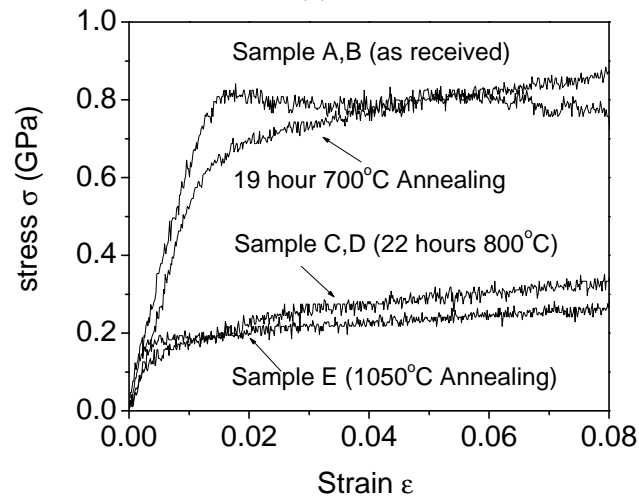
## 3.2 Steel Substrates

One of the advantages of stainless steel substrates is that the processing temperature for steel substrates is higher than that of plastic substrates ( $\sim 900^\circ\text{C}$ ). Devices with higher carrier mobilities, such as polycrystalline silicon TFTs (electron field effect mobility  $\sim 10 - 200 \text{ cm}^2/\text{Vs}$ , compared to  $\sim 1 \text{ cm}^2/\text{Vs}$  of amorphous silicon TFTs), can be fabricated on stainless steel substrates [23,24]. We first experimented with bare stainless steel foils (AISI 316, 12.5- $\mu\text{m}$  or 25- $\mu\text{m}$ -thick), which were plastically deformed by nitrogen pressurized up to 50 psi. At 50 psi, the center of the 12.5- $\mu\text{m}$ -thick foil was raised by  $\sim 0.50 \text{ cm}$  ( $h/R = 0.17$ ) (Fig. 3.1(a), Sample B), corresponding to a spherical dome with  $38^\circ$  field-of-view (as defined in Fig. 2.3(b)). After pressure was released, because of the elastic relaxation of the substrate, the height of the spherical dome was reduced to  $\sim 0.30 \text{ cm}$  ( $h/R = 0.10$ ), corresponding to a  $23^\circ$  field-of-view (indicated as “relaxation” in Fig. 3.1(a)). The 25- $\mu\text{m}$ -thick foil was deformed less (Fig. 3.1(b), Sample A). At 50 psi, the center of 25- $\mu\text{m}$ -thick foil was raised by  $\sim 0.40 \text{ cm}$  ( $h/R = 0.13$ ), corresponding to a spherical dome with  $30^\circ$  field-of-view. After pressure was released, the height of the spherical dome was reduced to  $\sim 0.20 \text{ cm}$  ( $h/R = 0.07$ ), corresponding to a  $15^\circ$  field-of-view. In these two cases, the field-of-view was reduced almost 50% after the elastic relaxation of the steel foils. This was not desirable because our goal was to permanently deform the substrate foil into a set spherical shape.

To reduce such elastic relaxation, it is essential to use substrates with lower yield strength. This was achieved by annealing the steel foils before deformation to create larger polycrystalline grains. Table 3.1 summarizes the annealing conditions used in our experiments (Sample E, AISI 304 stainless steel, was annealed by the supplier).



(a)



(b)

Figure 3.1 (a) Height of deformed stainless steel sheets as a function of applied pressure, with the height at the center of spherical domes normalized by the radius of the deformed region  $R$  (as defined in Fig. 2.3 (b)). The pressure was increased from zero, and the height of the spherical dome decreased after the pressure was released because of the elastic relaxation of the substrate. (b) Measured stress-strain relationship of stainless steel foils after various heat treatments. The stress-strain measurement is done by Instron<sup>®</sup> 8501 testing machine. Table 3.1 gives substrate thickness and annealing conditions.

Sample	Steel standard	Thickness ( $\mu\text{m}$ )	Anneal time (hour)	Anneal condition
A	AISI 316	25	as received	
B	AISI 316	12.5	as received	
C	AISI 316	25	22	800°C in Air
D	AISI 316	12.5	22	800°C in Air
E	AISI 304	25	1	1050°C in N <sub>2</sub>

Table 3.1 Annealing conditions for stainless steel substrates.

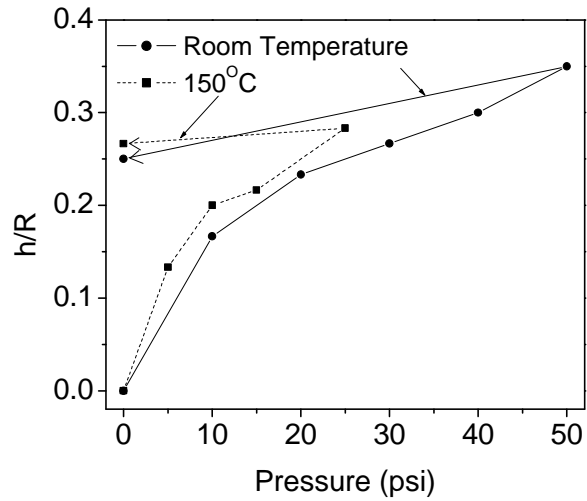
Fig 3.1 (b) demonstrates the effect of annealing on the measured stress-strain curves. Note for annealing at 800°C or higher, the yield strength is reduced from  $\sim 0.8\text{GPa}$  to  $\sim 0.2\text{GPa}$ . Thus, annealed foils can be deformed with little elastic relaxation after pressure release (Fig. 3.1 (a)). For example, Sample E, which is 25- $\mu\text{m}$ -thick (annealed at 1050°C in N<sub>2</sub> for one hour) at 50 psi, the center of the annealed foil was raised by  $\sim 0.93\text{ cm}$  ( $h/R = 0.31$ ), corresponding to a spherical dome with 69° field-of-view. After pressure was released, the height of the spherical dome was reduced to  $\sim 0.85\text{ cm}$  ( $h/R = 0.28$ ), corresponding to a 63° field-of-view. The height of the dome was only reduced by 8% due to the relaxation, which was a great improvement compared to the as-received foils.

### 3.3 Polyimide Substrates

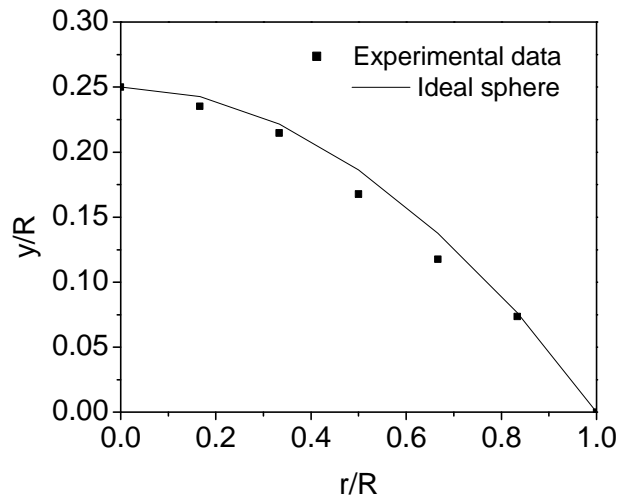
From the previous discussion, we learned that it was easier to permanently deform substrates with lower yield strength. Plastic substrates in general have even lower yield strength compared to stainless steel substrates. In our experiments, we use 50- $\mu\text{m}$ -thick Kapton<sup>®</sup> E polyimide substrates because they work well as a substrate for amorphous TFT fabrication: it is stable to process chemicals, and has a coefficient of thermal expansion of  $12 \times 10^{-6}/^\circ\text{C}$  [25] and an RMS surface roughness of  $\sim 30\text{ nm}$  [14]. A 50- $\mu\text{m}$ -

thick foil shrinks  $\sim 0.04\%$  after 2 hours at  $200^\circ\text{C}$ , it has the relatively low humidity expansion coefficient of  $9 \times 10^{-6}/\% \text{RH}$ , a water permeability of  $4 \text{ g/m}^2/\text{day}$ , and an oxygen permeability of  $4 \text{ cm}^3/\text{m}^2/\text{day}$  [14]. Fig. 3.2(a) shows the height (measured from the center of the deformed foil) of a polyimide substrate (diameter = 6 cm) as a function of applied pressure for both at room temperature and at  $150^\circ\text{C}$  deformation. At room temperature, at 50 psi the center of the annealed foil was raised by  $\sim 1.05 \text{ cm}$  ( $h/R = 0.35$ ). After pressure was released, the height of the spherical dome was reduced to  $\sim 0.75 \text{ cm}$  ( $h/R = 0.25$ ). Compared to the annealed  $25\text{-}\mu\text{m}$ -thick stainless steel foils (Sample E in Fig. 3.1(b)), the polyimide sample at room temperature was deformed more at 50 psi ( $h/R=0.35$  compared to  $h/R=0.31$ ). However, the polyimide substrates have larger elastic relaxation compared to the steel foil (Sample E in Fig. 3.1(b)) after the pressure release (final  $h/R=0.25$  compared to  $h/R=0.28$ ) because the Young's modulus of the polyimide substrate is 40 times smaller than that of the steel foil (Table 3.2). Fig 3.2(b) shows the shape of the polyimide sample deformed at room temperature after pressure released, which closely matches that of an ideal spherical dome with  $56^\circ$  field-of-view.

Heating up the polyimide substrate during deformation reduces its yield strength. For the sample deformed at  $150^\circ\text{C}$ , at 25 psi, the center of the annealed foil was raised by  $\sim 0.85 \text{ cm}$  ( $h/R = 0.28$ ), corresponding to a spherical dome with  $63^\circ$  field-of-view (the sample at room temperature had to be deformed at  $\sim 35 \text{ psi}$  to reach  $h/R=0.28$ ). After pressure was released, the height of the spherical dome was reduced to  $\sim 0.80 \text{ cm}$  ( $h/R = 0.27$ ), corresponding to a  $60^\circ$  field-of-view (Fig 3.2).



(a)



(b)

Figure 3.2 (a) Height of deformed 50- $\mu\text{m}$ -thick polyimide substrates as a function of applied pressure, with the height normalized by the radius of the deformed region  $R$ . (b) Shape of a polyimide substrate as a function of radius (normalized by the radius of the deformed region  $R$ , as defined in Fig. 2.3 (b)). The substrate is deformed to 50 psi then released. The solid line represents an ideal spherical dome with the same height at the center of the dome.

### 3.4 Strain Distribution in the Substrates

We used numerical modeling to examine the strain profile after deformation. The modeling was done in collaboration with Dr. Min Huang and Dr. Zhichen Xi. We modeled both the stainless steel and polyimide substrates used in the previous discussion as elastic-plastic materials with stress ( $\sigma$ )-strain ( $\epsilon$ ) relation as (Fig 3.3)

$$\mathbf{s} = \begin{cases} E\mathbf{e}, & \text{elastic, when } 0 < |\mathbf{e}| < \mathbf{s}_Y/E \\ C\mathbf{e}^n, & \text{plastic, when } \mathbf{s}_Y/E \leq |\mathbf{e}| \end{cases} \quad (3.1)$$

where  $n$  is the hardening index,  $C$  is a materials constant (derived from the curve fitting of the measured stress-strain relation), and  $E$  is the Young's modulus [14].  $\sigma_Y$  is the yield strength of the substrate, and is defined by the intersection of the elastic portion and the plastic portion of Eq. 3.1. We directly measured the stress-strain curves of Kapton<sup>®</sup> E polyimide at room temperature (Fig. 3.3). For the mechanical properties of Kapton<sup>®</sup> E polyimide at 150°C, we scaled the room-temperature properties according to the temperature dependence of the stress-strain relationship of a similar polyimide film (Kapton<sup>®</sup> HN) available in the literature [26]. Table 3.2 summarizes the materials constants used in the numerical analysis.

	E (GPa)	$\sigma_Y$ (GPa)	C(GPa)	n	Poisson ratio $\nu$
steel (Sample E: annealed at 1050°C in N <sub>2</sub> )	200	0.085	0.4	0.2	0.3
Kapton <sup>®</sup> E (Room Temp)	5	0.040	0.7	0.6	0.3
Kapton <sup>®</sup> E (150°C)	3	0.024	0.5	0.7	0.3

Table 3.2: Material parameters used in the numerical analysis.

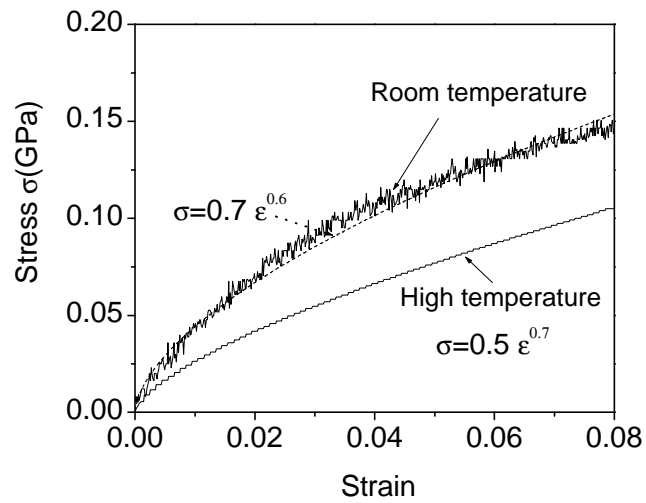
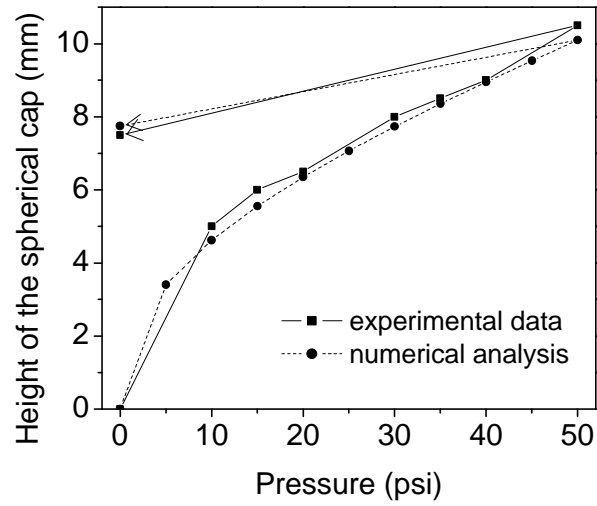


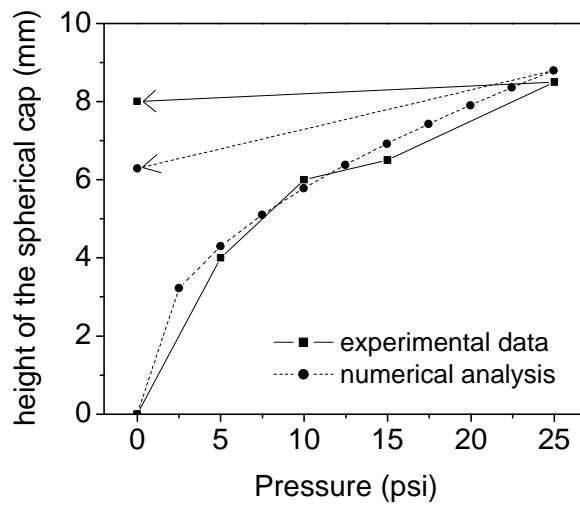
Figure 3.3 Measured and modeled stress-strain curve for polyimide substrate at room temperature, and the derived model of the 150°C stress-strain curve.

Fig. 3.4 (a) and (b) show a comparison between the experimental data and the numerical modeling of height vs. pressure for deformation of polyimide foils at both room temperature and 150°C. The results from numerical analysis closely match the experimental data. This agreement gives us confidence that modeling the polyimide substrates as elastic-plastic materials (Eq. 3.1), and the estimated 150°C stress-strain curve of Fig. 3.3 are good assumptions.

At the top of the spherical dome, the value of the circumferential strain is equal to that of the radial strain because the stretching is uniform in all directions at the apex. Thus at the top the strain is biaxial. The circumferential strain is fixed at zero at the edge of the spherical dome due to the clamping condition at the boundary. Fig. 5.5 shows the numerical modeling of the radial and circumferential strain distribution vs. radius in both stainless steel (sample E in Table 3.1, 25- $\mu\text{m}$ -thick) and polyimide (50- $\mu\text{m}$ -thick, room temperature deformation) substrates deformed into a 66° field-of-view ( $h/R=0.29$ ) spherical dome. The radial strain (Fig. 5.5(a)) for the stainless steel foil is 7.5% at the top and gradually decreases to 2.3% at the clamped edge, with an average of 5.6%. For the polyimide substrate deformed at room temperature, the radial strain is 5.9% at the top and slowly decreases to 5.6% at the clamped edge, with an average of 5.7%. The radial strain is quite uniform across the spherical dome for the polyimide substrate. Note for  $h/R=0.29$ , simple geometric considerations (Eq. 2.2) predicted an average radial strain of 5.6%.



(a)



(b)

Figure 3.4 Height of the spherical dome vs. applied pressure for polyimide substrates: (a) Room temperature deformation. (b) 150°C deformation. The results from numerical analysis closely match the experiment data.

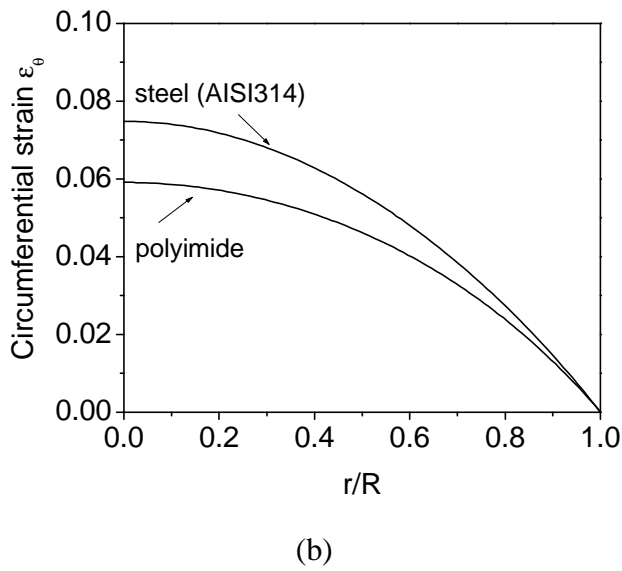
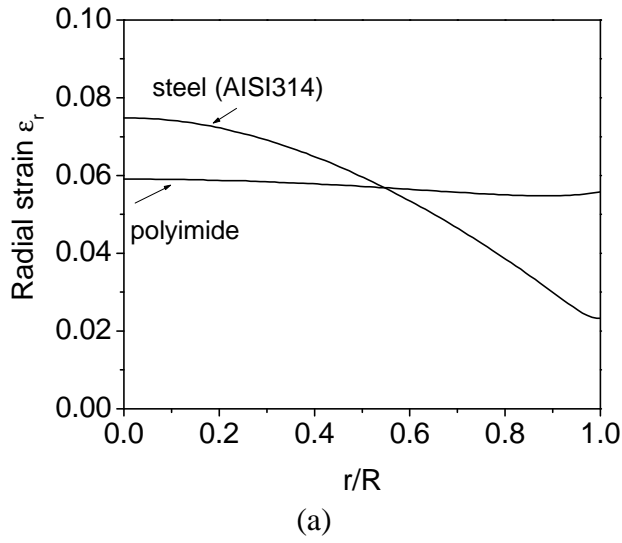


Figure 3.5 (a) Radial strain, and (b) circumferential strain distribution of the substrates (25- $\mu\text{m}$ -thick stainless steel and 50- $\mu\text{m}$ -thick polyimide foil) deformed into a  $66^\circ$  field-of-view ( $h/R=0.29$ ).

### 3.5 Chapter Summary

In this chapter we studied the spherical deformation of stainless steel and polyimide substrates. It was easier to permanently deform substrates with lower yield strength. Annealing the steel foils before deformation at very high temperature ( $\sim 800^\circ\text{C}$ ) lowers their yield strength. For polyimide substrates, lower yield strength is achieved by heating the substrate to  $\sim 150^\circ\text{C}$  during deformation.

We used numerical modeling to study the actual strain distribution in the substrates. Both the radial and circumferential strains are the greatest (and equal) at the apex and gradually decrease towards the edge of the spherical dome. For a substrate deformed into a  $66^\circ$  field-of-view, the radial strain at the top is larger (7.5%) for the stainless steel foil compared to the polyimide substrate deformed at room temperature. Interestingly, the predicted radial strain in the plastic substrate is quite uniform (Fig. 5.6(a)), and the peak strain (5.9%) is close to the average radial strain ( $\mathbf{e}_{r,avg} \sim 5.6\%$ ) predicted by Eq. 2.2. It suggests that  $\mathbf{e}_{r,avg}$  is a good approximation for estimating the peak radial strain of the polyimide substrates.

# Amorphous Silicon Islands on Spherical Domes

## 4.1 Introduction

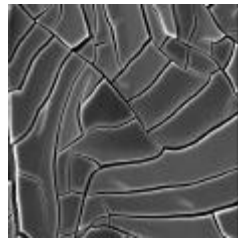
In Chapter 3, we described using pressurized nitrogen to deform thin foil substrates into spherical cap shapes. While polyimide and steel substrates can easily be plastically deformed with 6% strain, inorganic materials such as silicon, silicon dioxide, and silicon nitride, are brittle, and can only be elastically deformed to a much lower value of strain. Beyond  $\sim 0.5\%$  tensile strain, they do not plastically deform – they crack. In this chapter, we study the breaking limit of these semiconductor device materials on thin stainless steel and polyimide foils. We will demonstrate that although uniform blanket device layers crack after the spherical deformation of the substrate, by patterning device materials into isolated islands, “hard” device islands can remain crack-free after deformation. We will discuss the strain distribution in the device islands for two different substrate structures, and why patterning brittle materials into islands suppresses fracture in the devices.

## 4.2 Island Concept

We started by depositing a 0.5- $\mu\text{m}$ -thick silicon dioxide on a flat steel foil by spin casting a precursor and curing. This layer is typically called spin-on-glass (SOG) and serves as a barrier against metal diffusion from the stainless steel foil into the electronic devices. It also planarizes the steel foil surface and insulates the electronic devices from the steel substrate. For polyimide substrates, we deposited 0.4- $\mu\text{m}$ -thick silicon nitride followed by 0.1- $\mu\text{m}$ -thick amorphous silicon onto flat polyimide substrates by plasma-enhanced chemical vapor deposition (PECVD) system at 150°C. These two layers are the typical first layers for amorphous silicon transistor processing.

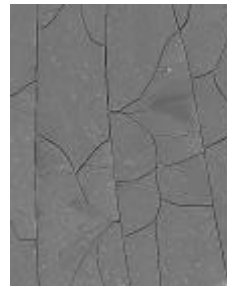
When the structures were then deformed into a 66° field-of-view spherical dome (with ~ 6% average radial strain), both the SOG on stainless steel and the silicon/silicon nitride on the polyimide substrate crack (Fig. 4.1(a), (b)). This confirms that these hard materials cannot be expanded elastically or plastically to ~ 5% strain without failure. Note, however, that the cracked films have intact islands of ~ 3  $\mu\text{m}$  on steel substrates and ~ 10  $\mu\text{m}$  on polyimide substrates. This implies that islands of the silicon dioxide, silicon nitride, or amorphous silicon of this size would survive after deformation.

On another batch of substrates, we then patterned the "hard" device materials into islands onto the "soft" stainless steel or polyimide substrates before deformation with the hope that the large average strain in the substrate would not be transferred to the islands. The qualitative concept is that the soft substrate can flow beneath the island during the deformation so that the island itself might not be excessively strained (Fig. 4.2).



10  $\mu\text{m}$

(a)



100  $\mu\text{m}$

(b)

Figure 4.1 After deformation to  $66^\circ$  field-of-view: (a) SEM photo of blanket silicon oxide/steel structure deformed at room temperature. (b) SEM photo of blanket silicon/silicon nitride/polyimide structure deformed at room temperature.

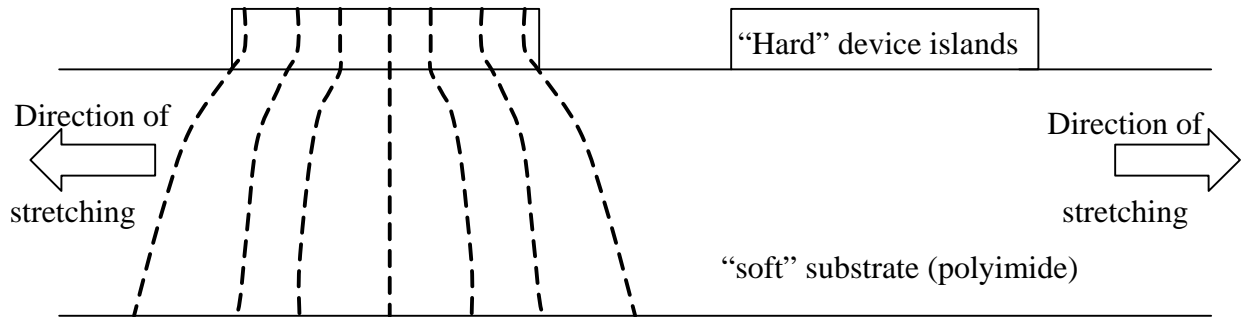


Figure 4.2 Schematic diagram showing “hard” islands on “soft” substrates during deformation. Deformation takes place mostly in the inter-island region to limit the strain in the substrates. The dotted lines represent deformation of originally straight vertical lines in the substrate.

This method was first applied to islands consisting of 0.5- $\mu\text{m}$ -thick silicon dioxide on 25- $\mu\text{m}$ -thick steel foil substrates. Only 5  $\mu\text{m}$  silicon dioxide islands remained intact after room-temperature deformation to a 66° field-of-view spherical dome (Fig. 4.3(a)).

Because 5- $\mu\text{m}$  device islands are too small for device fabrication in our lab, the rest of the paper will focus on device islands on polyimide substrates.

#### 4.2.1 Planar device islands on polyimide substrates

From the previous discussion, we know that by patterning uniform semiconductor layers into isolated islands, small islands can be fracture-free after spherical deformation of the substrate. The blanket film of 0.1- $\mu\text{m}$ -thick amorphous silicon and 0.4- $\mu\text{m}$ -thick silicon nitride on a 50- $\mu\text{m}$ -thick polyimide substrate was patterned before deformation into arrays of 20 to 120  $\mu\text{m}$  square islands, with the surface coverage varying from 4% to 44%. With this method, near the top of the spherical caps, intact square islands with a 20- $\mu\text{m}$ -edge could now be routinely achieved after the substrate was deformed into a spherical dome with 66° field-of-view under pressure (56° field-of-view after pressure is released, corresponding to a height of  $\sim 0.75$  cm). All larger islands cracked [19]. Note that the combined thickness of 0.5  $\mu\text{m}$  is the typical thickness for the thinnest (thus, the most fragile) part of thin-film transistors. The total thickness of all layers for an amorphous silicon transistor is about  $\sim 1$   $\mu\text{m}$  in general [27].

Fig. 4.4 compares the height vs. pressure of the polyimide substrates with and without the islands, with an average surface coverage of 25%. Within experimental errors, the islands have no effect on deformation profiles and the resulting average strain in the substrate.

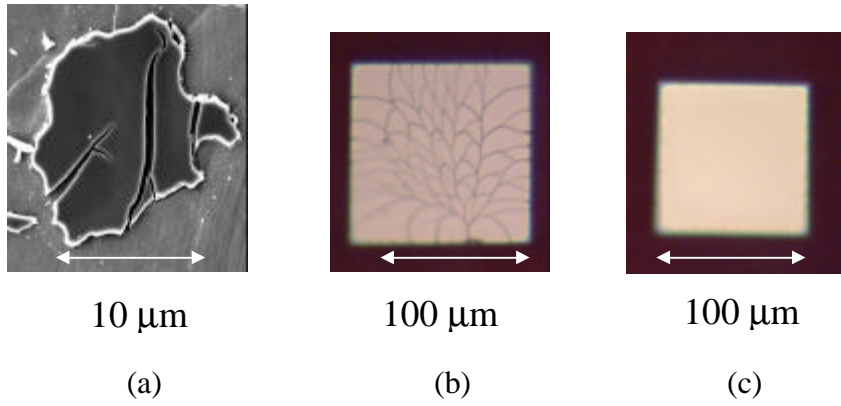
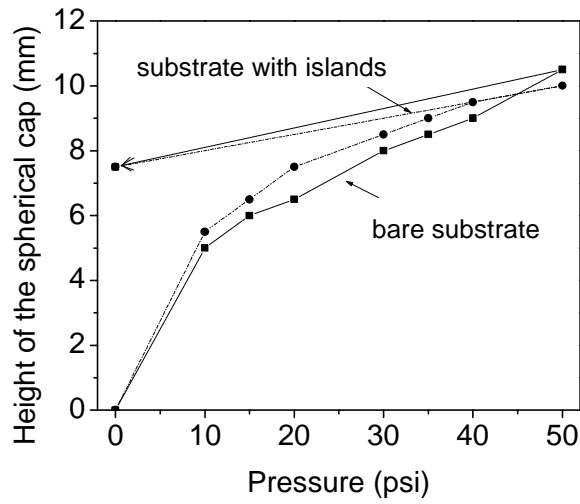
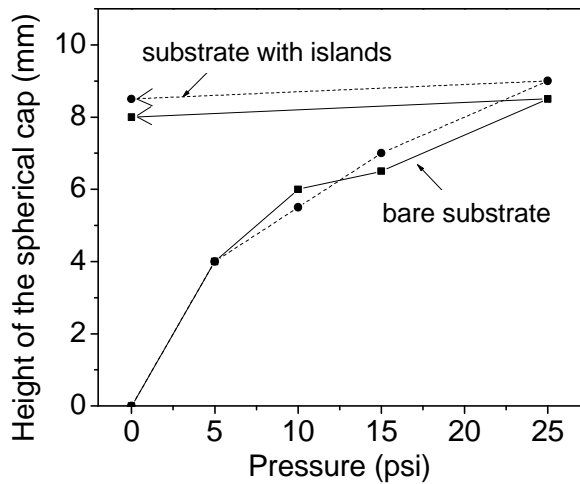


Figure 4.3 After deformation to 66° field-of-view: (a) SEM photo of a 10- $\mu\text{m}$  silicon oxide island on steel substrate deformed at room temperature. (b) Optical micrograph of 120- $\mu\text{m}$  island silicon/silicon nitride islands on polyimide deformed at 150°C. (c) Optical micrograph of similar 100- $\mu\text{m}$  island deformed at 150°C.



(a)



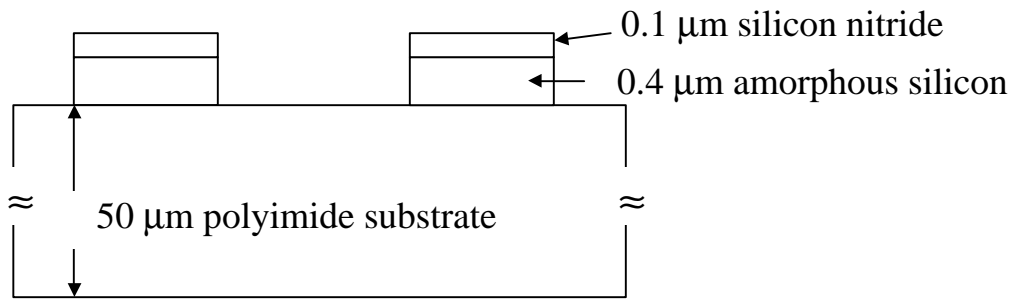
(b)

Figure 4.4 Experimental data of the height of the polyimide substrates with and without the islands as a function of applied pressure. The island size ranges from 20 to 120  $\mu\text{m}$ . (a) Room temperature deformation. (b) 150°C deformation. The islands have little effect on the deformation profile.

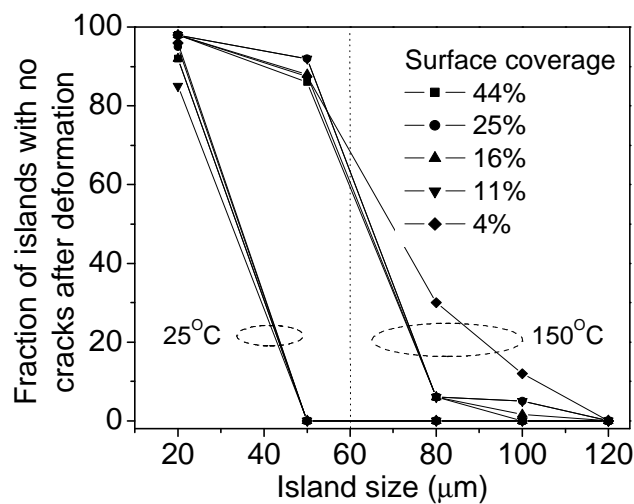
The device island has to be large enough for a transistor and three contact pads (source, drain, and gate) for characterization. We sought 40- $\mu\text{m}$  islands for device fabrication. However, even at low island surface area coverage, it was not possible to realize 40- $\mu\text{m}$  islands at room temperature without cracks. We used two approaches to increase the island size. The first approach was to heat the substrate during deformation, and the second was to etch deep into the polyimide substrate to create a mesa island structure (see Section 4.2.2).

By heating the substrate to 150°C to soften the substrate during the deformation process (Fig.3.3), the maximum island size without cracks for deformation to a 66° field-of-view (before pressure release) was increased to 100  $\mu\text{m}$ . Fig. 4.5(b) shows the yield of the islands without cracks vs. island size near the top of the cap (where the strain is the highest). For a given island size, varying the spacing between the islands to change the island density has little effect on the yield of crack-free islands. It is due to the fact that once the substrate begins to plastically deform, further strain requires very little additional stress. Consequently, the shear load that pulls the island is only weakly dependent on the area of the inter-island region, and the island density is not a substantial factor in the fracture mechanism.

Fig. 4.3(b) and (c) show 120- $\mu\text{m}$  and 100- $\mu\text{m}$  islands on polyimide substrate deformed to a 66° field-of-view under pressure. Note the 120- $\mu\text{m}$  island cracked, but the 100- $\mu\text{m}$  island did not. Transistors and circuits were fabricated in those 100  $\mu\text{m}$  islands [28, 29], and will be described in Chapter 5 and 6.



(a)

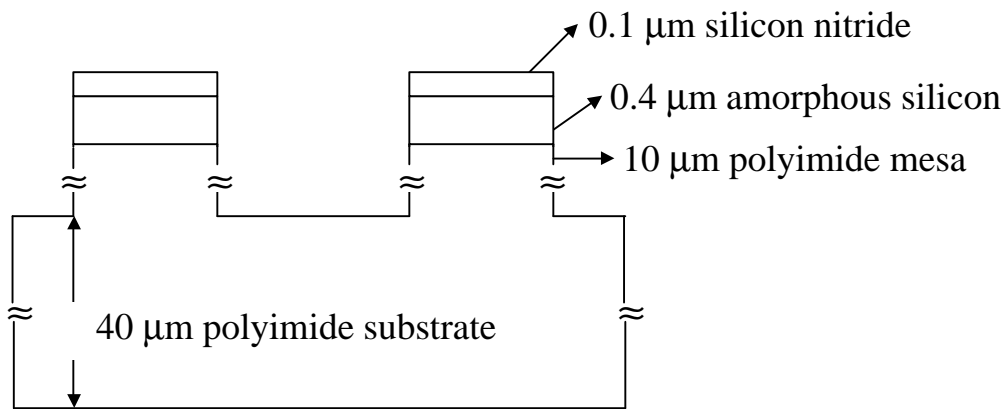


(b)

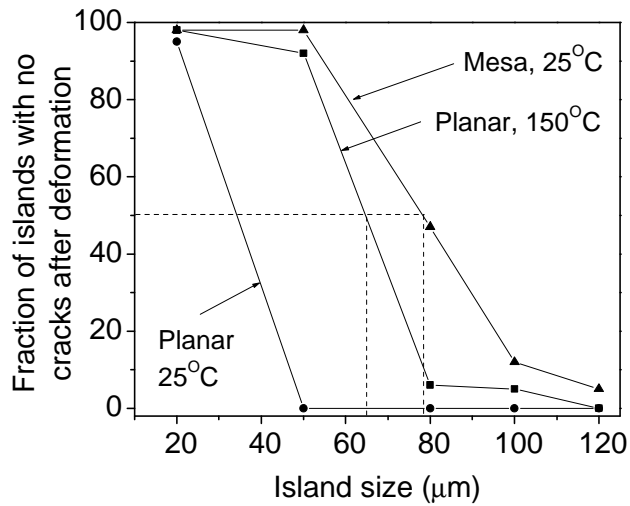
Figure 4.5 (a) Cross-section of planar island structure. (b) Fraction of square amorphous silicon/silicon nitride islands on polyimide with no cracks as a function of the island size, for different surface area coverage. Substrate is deformed to 66° field-of-view at room temperature or 150°C. The data were taken near the center of the cap.

#### 4.2.2 Mesa device islands on polyimide substrates

Though most 50- $\mu\text{m}$  planar islands (with a few 100- $\mu\text{m}$  ones) deformed at 150°C were intact after deformation, because of the instability of amorphous silicon, it was not desirable to deform the final device structure at 150°C. To achieve the maximum island size without fracture after deformation at room temperature, we developed an alternative structure, in which we not only pattern the semiconductor material into individual islands but also etch deep ( $\sim 10\ \mu\text{m}$ ) into the substrate to create the device on a polyimide mesa structure (Fig. 4.6(a)). The tall polyimide mesas decoupled the device islands from the substrate so that the strain in the device islands was reduced. While only 20- $\mu\text{m}$  planar islands were intact after the substrate with planar islands was deformed to a 66° field-of-view spherical dome at room temperature,  $\sim 50\%$  of the 80- $\mu\text{m}$  mesa islands (25% surface area coverage) deformed at room temperature were intact after deformation (Fig. 4.6(b)). Mesa islands deformed at room temperature also have a higher yield compared to the planar islands deformed at 150° C. Only  $\sim 5\%$  of the 80  $\mu\text{m}$  planar islands (with surface area coverage of 25%) deformed at 150° C were intact after deformation.



(a)



(b)

Figure 4.6 (a) Cross-section of mesa island structure. (b) Fraction of square amorphous silicon/silicon nitride islands on polyimide with no cracks as a function of the island size, for 25% surface area coverage. Substrate is deformed to 66 $^{\circ}$  field-of-view at room temperature. The data were taken near the center of the cap.

## 4.3 Strain Distributions in Island Structures

### 4.3.1 Modeling of strain distribution in the islands

In this section, we use numerical modeling to calculate the strain distribution in the islands. This is desired to understand the limits of deformation before cracking, and to understand the performance of the TFTs after deformation in those islands [29]. Four important approximations are made in performing this calculation. First, we seek in detail the strain distribution of one island at the top of the spherical cap, where the strain is the greatest. The effect of the local bending curvature due to the spherical deformation on the strain is negligible at the apex of the dome, because the islands are very small compared to the entire substrate. (These islands are of magnitude of 100- $\mu\text{m}$  wide, and the radius of curvature of the substrate is  $\sim 5$  cm). This corresponds to a field-of-view of  $0.11^\circ$ . Using Eq. 2.2, this causes a strain contribution of only  $2 \times 10^{-5} \%$ . Consequently, nearly all of the strain will come from the biaxial stretching of the substrate caused by expansion in both radial and circumferential directions. The dimension of the numerical modeling is thus reduced to a two-dimensional problem. Second, from experimental data, we learned that the island surface area coverage had little effect on the yield of the intact islands. This suggests that the stress on the island is only weakly dependent on the island spacing. Therefore, for most of the numerical modeling, we only consider one single island and its immediate surrounding substrate (Fig 4.7). Third, from Section 3.4, we concluded that the radial strain in the plastic substrate is quite uniform (Fig. 3.5(a)), and the peak strain is close to the average radial strain predicted by Eq. 2.2. Hence, we model this single island on the top of the dome as an island stretched with a biaxial strain of the value equal to the average radial strain across the spherical cap calculated from the

height of deformation (Eq. 2.2). Finally, for simplicity, we model device islands as a single round (not square as in experiments) island with radius  $R_I$ . The island is surrounded by a circle of bare substrate (radius  $R_S$ ), the edges of which are expanded radially by a fixed amount as a boundary condition of the simulation. The surface area coverage (island density) is thus  $(R_I/R_S)^2$ .

To implement the modeling, we used a commercially-available finite element analysis program, ABAQUS [30], to examine the strain distribution in the thin film island/substrate structure. The “hard” material on planar islands was assumed to be 0.5- $\mu\text{m}$ -thick and mesa islands to be 1- $\mu\text{m}$ -thick, unless otherwise noted. The polyimide substrate is 50  $\mu\text{m}$  thick with the stress-strain relation described in Eq. 3.1 and the material parameters in Table 3.2. We assume the Young’s modulus for the 0.5  $\mu\text{m}$  or 1  $\mu\text{m}$  layers to be 200 GPa [31]. Because silicon nitride and amorphous silicon have similar Young’s moduli, to the first order, we can consider these hard layers as being of either material, or a combination with the total thickness as stated above.

We also assume that the substrate (radius  $R_S$ ) is stretched with 6% strain (corresponding to  $h/R=0.30$ ) in the radial direction when the pressure is on. In our experiments, the height of the spherical dome deformed at room temperature was reduced to  $\sim h/R=0.25$  (corresponding average radial strain ( $\mathbf{e}_{r,avg}$ ) of 4.0% (Eq. 2.2)) after pressure release. At 150°C, these figures were  $h/R=0.27$  and  $\mathbf{e}_{r,avg}=4.7\%$  respectively. Therefore, after stretching the substrate by 6%, in our modeling, we reduced substrate stretching to 4% in the radial direction for room temperature deformation to find the final strain distribution in the islands after pressure release. For 150°C deformation, we relaxed the

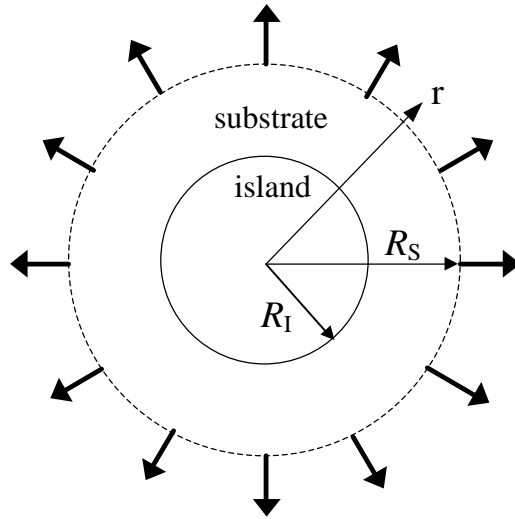


Figure 4.7 Schematic diagram (top view) of the modeled round island (radius  $R_I$ ) and substrate (radius  $R_S$ ) in the numerical modeling. Biaxial strain is applied radially outward from the edge of the substrate.

substrate stretching to 5% to study the final strain distribution in the islands after pressure release.

### 4.3.2 Strain distribution in planar islands

Fig. 4.8 shows a contour plot of the radial strain distribution in a structure with a 100- $\mu\text{m}$ -diameter planar island after stretching to 6% at the substrate boundary at room temperature (before being allowed to relax back to 4% stretching). Because the island is only 0.5- $\mu\text{m}$ -thick (the substrate is 50- $\mu\text{m}$ -thick), the island is too thin to be seen in Fig. 4.8. The strain in the island is expected to be the same as the top of the substrate at the island-substrate interface. The results show that the strains in the substrate are pinned to low values underneath the island by the high Young's modulus of the island (200 GPa, compared to that of 5 GPa of the substrate), but increase farther from the island and deep underneath it. For example, the strain on the surface of the substrate in the inter-island region is  $\sim 6\%$ . This confirms the qualitative concept of the islands described in Fig. 4.2. Indeed, for the rigid islands to be intact, the plastic deformation must occur in the substrate region away from the islands.

Fig. 4.9 shows the radial strain in a round 1- $\mu\text{m}$ -thick, 50- $\mu\text{m}$ -diameter amorphous silicon island as a function of position after deformation at 150°C to 6% average strain and then relaxation back to 5% average strain in the substrate. Note that the radial strain is largest (0.33% when pressure is on, 0.29% when pressure is off) at the island center and gradually decreases to near zero towards the island edge (because the island edge is free). Fig. 4.10 shows the calculated radial strain at the center of the island as a function of the island diameter for 0.5- $\mu\text{m}$ -thick silicon planar (island density ranging from 6.2% to 60%) and 0.5- $\mu\text{m}$ -thick mesa islands (before relaxation) on a 50-

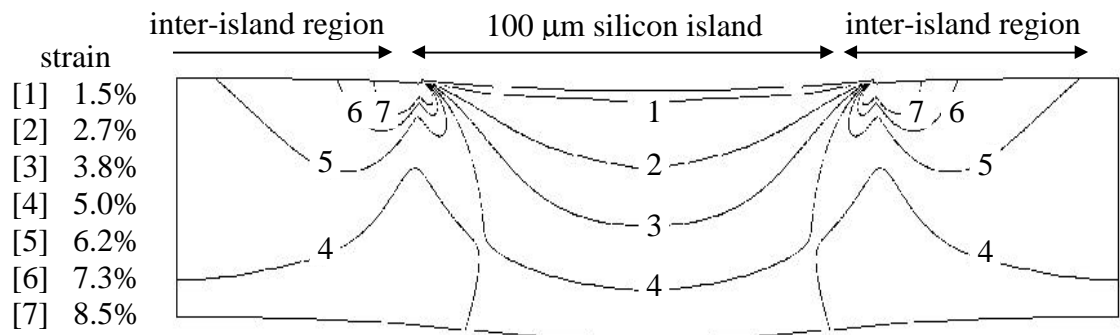


Figure 4.8 Contour plot of the radial strain distribution in a 50-μm thick polyimide substrate with a round silicon island (100 μm in diameter, 0.5-μm-thick) after stretching to average biaxial tension of 6% at room temperature. The modeled substrate size was a circle of 200 μm in diameter.

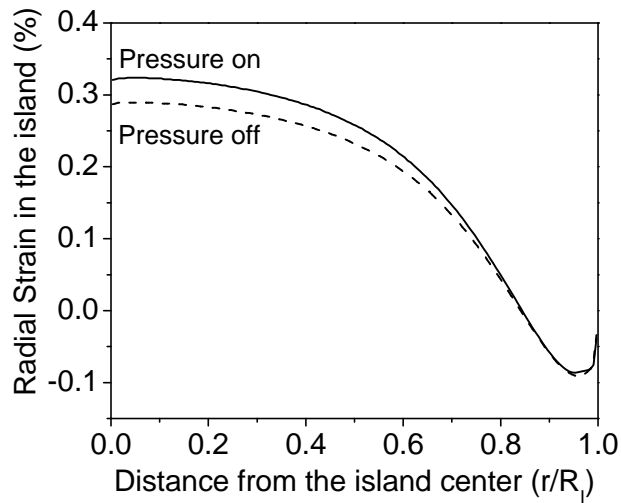


Figure 4.9 Predicted radial strain in a round amorphous silicon island (thickness = 1  $\mu\text{m}$ , diameter = 50  $\mu\text{m}$ ) after the polyimide substrate (50- $\mu\text{m}$  thick) is deformed with 6% strain and relaxed to 5% strain in the substrate as a function of position, using the estimated 150°C mechanical properties of polyimide of Table 3.2.

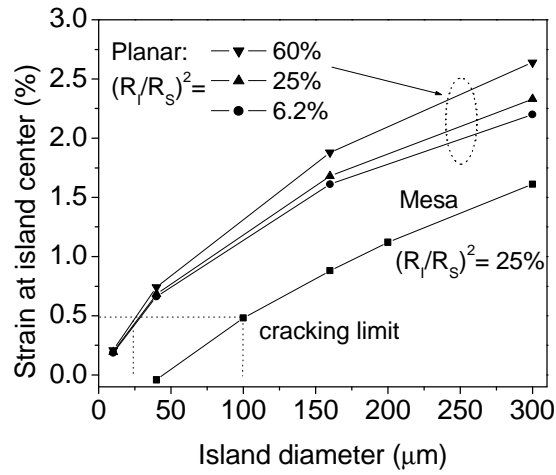


Figure 4.10 Strain at the island center (the maximum strain for planar islands) as a function of the island diameter for 0.5-μm- thick circular silicon islands (both planar and mesa islands) on a 50-μm-thick polyimide substrate stretched with 6% strain at room temperature.

$\mu\text{m}$ -thick polyimide substrate stretched with 6% strain for room temperature deformation. The strain in the islands increases as a function of the island diameter, explaining why larger islands crack. The strain in the island is a weak function of the island density, consistent with the experimental observation that the surface area coverage does not affect the yield of islands without cracks. Fig. 4.5(b) showed that only 20  $\mu\text{m}$  planar islands survived after room temperature deformation. Fig. 4.10 demonstrates that the strain at the planar island center (where the strain is the maximum) for 50  $\mu\text{m}$  planar islands is  $\sim 0.75\%$  and  $\sim 0.4\%$  for 20  $\mu\text{m}$  islands. Therefore, the critical strain at which the island breaks is between 0.4% and 0.75%.

The critical point remains how to prevent fracture in the device structures. Patterning “hard” device layers into islands limits the strain in the islands because the deformation takes place mostly in the “soft” substrate. One of the straightforward approaches to increase device island size is to make the device island “harder” by increasing the thickness of the island. Fig. 4.11 shows the predicted strain by numerical simulation of a circular silicon island (160  $\mu\text{m}$  in diameter) on a 50- $\mu\text{m}$ -thick polyimide substrate stretched with 5% average strain in the substrate with respect to the island thickness. The surface area coverage is fixed at 25%. The deformation condition is set at room temperature. It shows that for a 0.5- $\mu\text{m}$ -thick island, the strain at the island center is 1.5% when the substrate is stretched with 5% average strain. However, the critical strain at which the islands break is only  $\sim 0.3\%$ . Therefore, it is impossible to achieve a 160- $\mu\text{m}$ -wide, 0.5- $\mu\text{m}$ -thick island at room temperature. Nevertheless, when the island thickness is increased to 3  $\mu\text{m}$ , the strain in the island center is reduced to  $\sim 0.5\%$ . It demonstrates that it is feasible to achieve large islands.

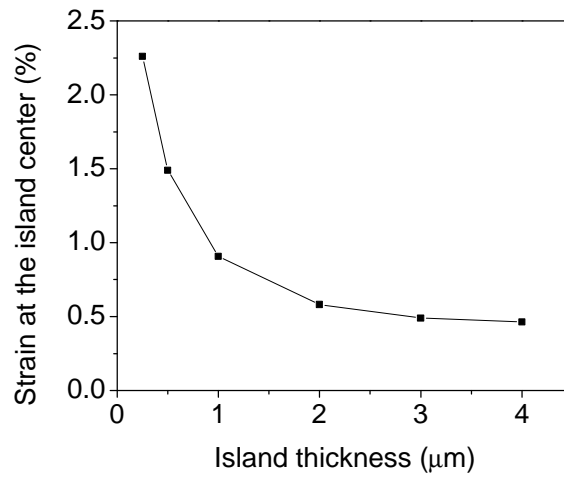


Figure 4.11 The predicted strain at the island center vs. island thickness for a circular silicon island (160  $\mu\text{m}$  in diameter) on a 50- $\mu\text{m}$ -thick polyimide substrate stretched with 5% strain at room temperature. The island density is 25%.

### 4.3.3 Strain distribution in mesa islands

Fig. 4.10 shows that mesa islands indeed have much lower strain than planar islands of similar geometry, which explains the experimental success in realizing larger intact islands with this approach. In the experiment, less than ~20% of 100  $\mu\text{m}$  mesa islands remained fracture-free after the substrate was deformed to a spherical dome with a  $66^\circ$  field-of-view ( $h/R=0.29$ ), when the pressure was on (Fig. 4.6(b)). Modeling shows for mesa islands of 100  $\mu\text{m}$ , the strain at the center of the island is  $\sim 0.5\%$  (Fig. 4.10). We conclude that the critical strain at which the islands break is approximately 0.5%. This is consistent with previous results in which amorphous silicon thin-film-transistors were subjected to uniaxial tension by cylindrical deformation [6,16].

Fig. 4.10 also shows that for mesa islands smaller than 40  $\mu\text{m}$ , the strain at the island center is smaller than zero when the pressure was on, implying that the island centers were in compression. That the islands could be in *compression* after stretching the substrate is surprising. To understand this, Fig. 4.12 shows the modeled radial strain as a function of radius in a round amorphous silicon island (thickness = 1  $\mu\text{m}$ , diameter = 50  $\mu\text{m}$ ) on 10- $\mu\text{m}$  polyimide mesa after the polyimide substrate (50- $\mu\text{m}$  thick) is deformed with 6% strain and relaxed to 4% average strain. It shows that the island center is under compression with compressive strain of  $\sim -0.09\%$  when pressure is applied. After the pressure is released, the strain magnitude is increased to  $\sim -0.11\%$ . The compression can be explained by the cross sections of the structure at different stages of the finite element analysis Fig. 4.13.

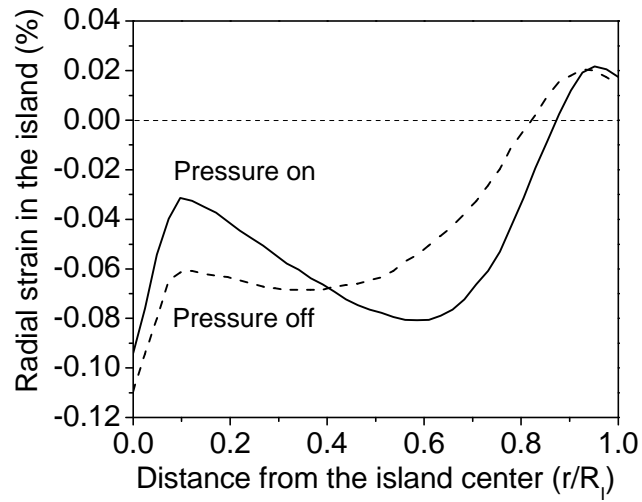


Figure 4.12 Predicted radial strain in a round amorphous silicon island (thickness = 1  $\mu\text{m}$ , diameter = 50  $\mu\text{m}$ ) on 10- $\mu\text{m}$  polyimide mesa after the polyimide substrate (50- $\mu\text{m}$  thick) is deformed with 6% strain and relaxed to 4% strain in the substrate as a function of position, using the room-temperature mechanical properties of polyimide of Table 3.2.

During deformation, the strain at the side of the polyimide pillars was so large that the lower mesa edge was permanently deformed. Even after the pressure was released, the mesa edge was still bent. Consequently, the island center was forced into compression even though the substrate as a whole on average was in tension. Note that the performance of amorphous silicon TFTs on mesa structures after deformation is consistent with that films being in compression (a reduction in mobility). The relationship between device performance and the island structure will be examined in detail in Chapter 5.

For applications such as displays on objects with arbitrary shapes, the substrate can be repeatedly deformed with different strain levels. Thus, it is highly desirable to fabricate devices with structures less sensitive to the substrate deformation to assure consistent electronic characteristics. Fig. 4.14 shows the calculated biaxial strain at the island center as a function of the island diameter for 1- $\mu\text{m}$ - thick circular silicon islands (both planar and mesa islands) on a 50- $\mu\text{m}$ -thick polyimide substrate stretched with 6% strain at the substrate boundary when pressure is on and after pressure release (4% strain at the substrate boundary) at room temperature. Note that by using a mesa design, it is feasible to design devices so that these devices endure less strain during the substrate deformation, compared to that in the planar structures.

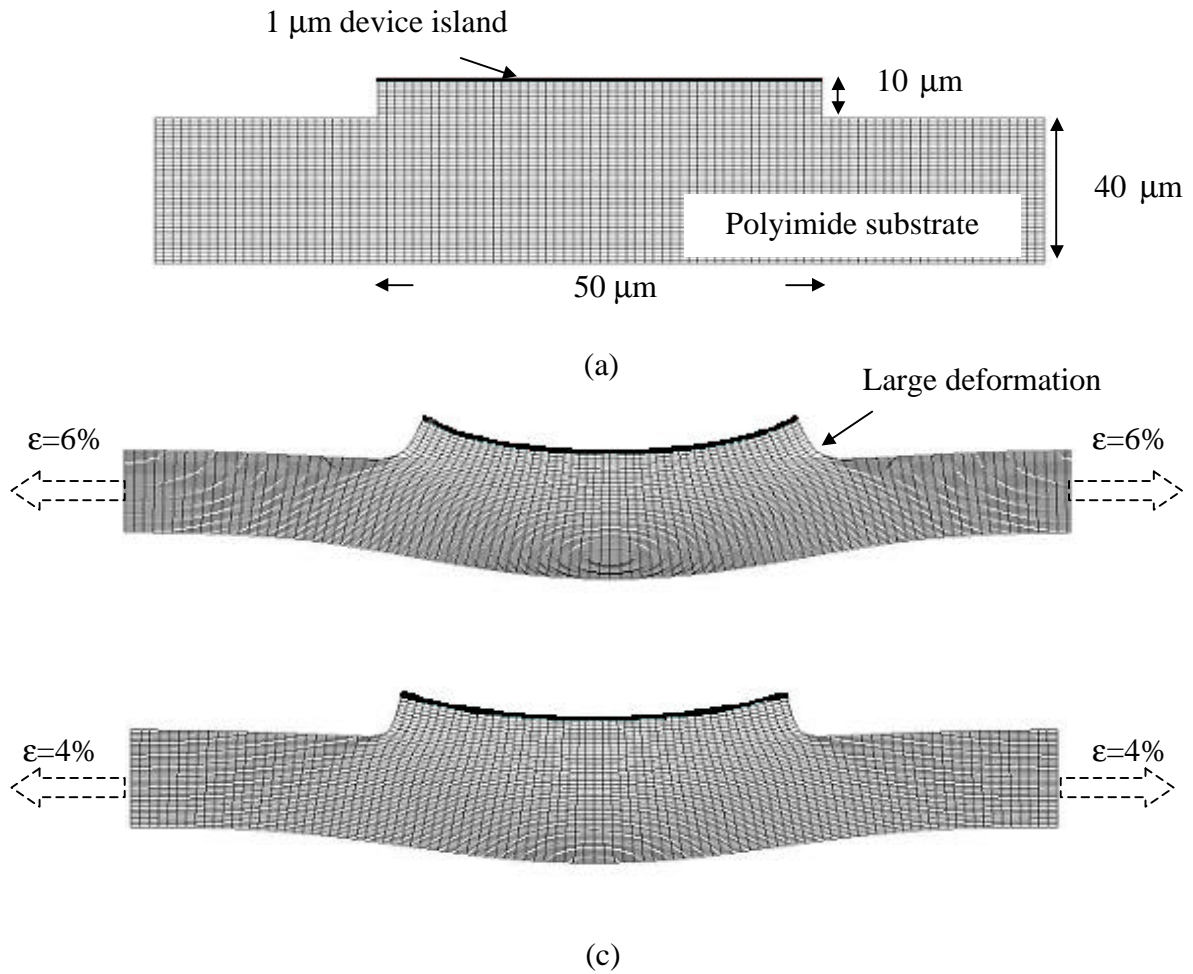


Figure 4.13 Structure of a 50- $\mu\text{m}$  round amorphous silicon island (thickness = 1  $\mu\text{m}$ ) on 10- $\mu\text{m}$  polyimide mesa: (a) before deformation, (b) during deformation (to 6% strain at the substrate boundary). The deformation at mesa edge is permanent, and (c) after pressure release (4% strain at the substrate boundary).

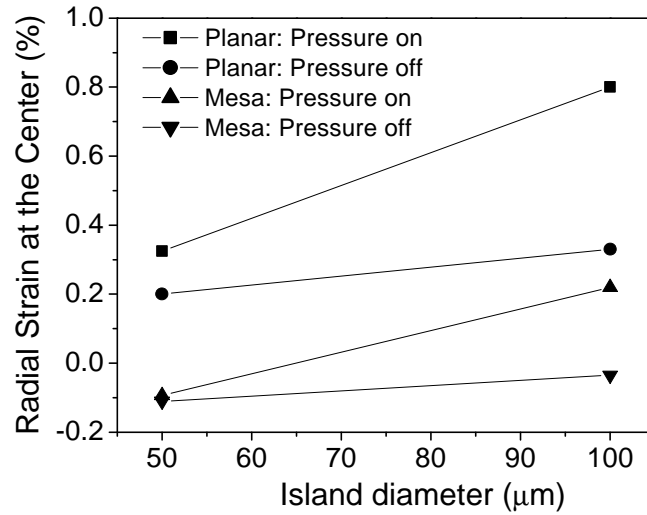


Figure 4.14 Predicted strain at the island center as a function of the island diameter for 1- $\mu\text{m}$ - thick circular silicon islands (both planar and mesa islands) on a 50- $\mu\text{m}$ -thick polyimide substrate stretched with 6% strain at the substrate boundary when pressure is on and after pressure release (4% strain at the substrate boundary) at room temperature. The island density is 50%.

## 4.4 Chapter Summary

This chapter explored, through experiments and finite element analysis, the ability to plastically deform thin film semiconductor structures on deformable substrates to spherical cap shapes without cracking the semiconductor layers. The major challenge involves contending with the large strain due to extreme deformation that will crack uniform “hard” layers such as silicon or silicon nitride. By patterning amorphous silicon and silicon nitride layers into islands, such problems can be avoided despite average strains in the substrate in excess of 5%. The strain in the island increases with the island size, but is only weakly dependent on island density when the substrate is soft. By etching into the substrate to create TFTs on a polyimide mesa device structure, the strain in the device layers was greatly reduced. Furthermore, the devices could be in compression even if the substrate was stretched due to the plastic deformation at the polyimide island edge. We will discuss the performance of electronic devices in these individual islands in the next chapter.

# Thin-Film Transistors on Spherical Domes

## 5.1 Introduction

Thin-film transistors (TFTs) are the most widely used devices in macroelectronics because of their good reproducibility and uniform characteristics on large-area substrates for applications such as liquid crystal displays (LCDs) and sensor arrays [32-35]. In this chapter, we review the fundamentals of the amorphous silicon TFTs (Section 5.2) and describe how to fabricate amorphous silicon TFTs on Kapton® polyimide substrates (Section 5.3). The polyimide substrate with finished devices is then permanently deformed into a spherical dome. Section 5.4 discusses the device characteristics of these TFTs after the deformation of the substrate. We present two device structures: TFTs on planar islands and TFTs on mesa islands. The results show a monotonic relationship between the change in the mobility of TFTs and the device island size, which suggests that the change in the mobility was due to the strain in the island. Section 5.5 discusses the relationship between biaxial strain (due to the spherical deformation of the substrate) and its effects on electrical properties of amorphous silicon devices.

## 5.2 Properties of Thin-film Transistors

Fig. 5.1 shows a hydrogenated amorphous silicon (a-Si:H) TFT with the bottom gate, back-channel etch structure on a flat polyimide substrate after fabrication. All TFT silicon layers were deposited at 150°C substrate temperature. The fabrication process is described in detail in Section 5.3. The (a) transfer and (b) output characteristics of such TFT is shown in Fig. 5.2. The TFT output characteristics are similar to the output characteristics of a single crystalline silicon metal-oxide-semiconductor field effect transistor (MOSFET) and can be reasonably well described by the standard MOSFET equations. However, the states which carriers occupy and their transport mechanisms are quite different. The static transistor characteristics of a TFT are determined by the localized electronic states that occur in the band gap of the undoped amorphous silicon, not by dopant levels. Essentially, the localized states in the amorphous silicon can be categorized into two types, tail states and deep states. The tail states are the silicon conduction band states broadened and localized by the disorder to form a tail of localized states just below the conduction band mobility edge. The deep states originate from defects in the amorphous silicon network. They mostly consist of silicon dangling bonds, which have a wide range of energies because of the variations in the local environments.

A positive voltage  $V_{gs}$  applied to the gate attracts majority carrier electrons to the amorphous silicon layer. When  $V_{gs}$  is small, most electrons are localized in the deep states and are not mobile. The TFT remains in OFF state. Further increasing the gate voltage causes the tail states to become occupied. When  $V_{gs}$  exceeds a threshold voltage ( $V_{th}$ ), a portion of the induced electrons is thermally excited to mobile states where they can carry current, and the transistor switches to ON state. Thus, the deep states, mostly

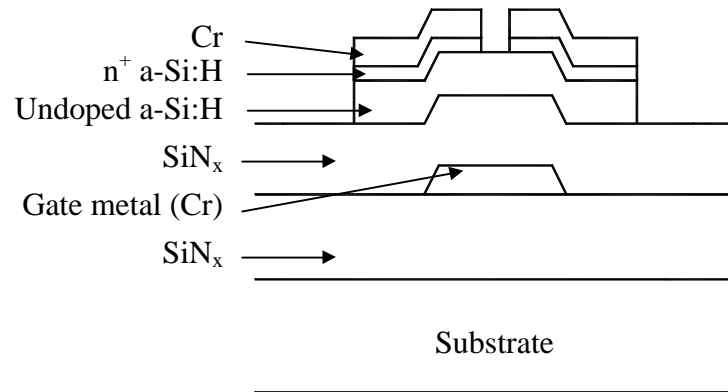
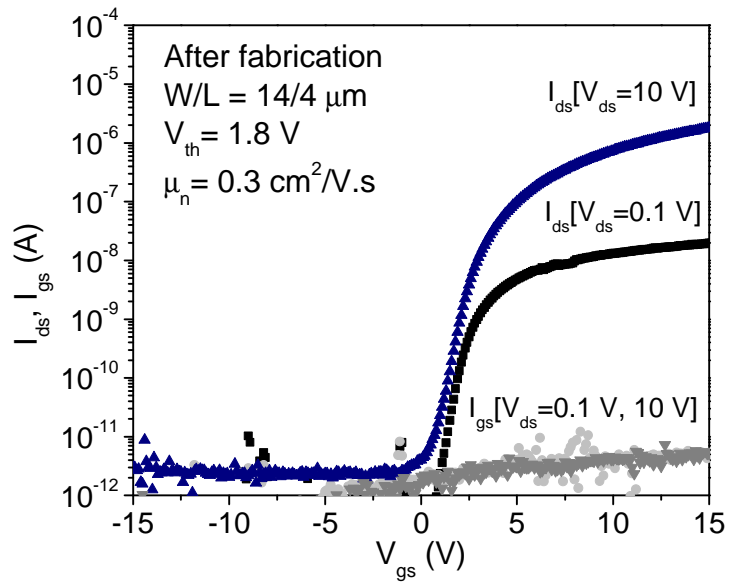
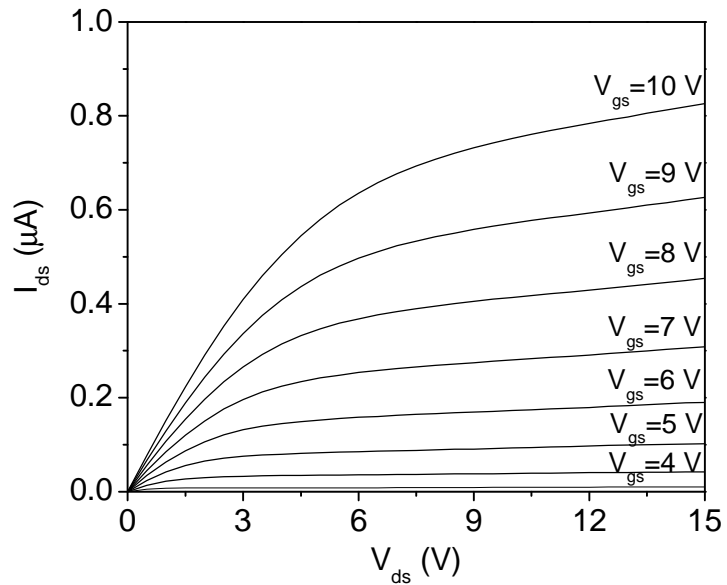


Figure 5.1 Cross-section of an a-Si:H TFT with the conventional staggered bottom-gate, back-channel-etch structure on a flat polyimide substrate. All TFT silicon layers were deposited at 150°C substrate temperature. The fabrication process is described in detail in Section 5.3.



(a)



(b)

Fig. 5.2 (a) Transfer and (b) output characteristics of an a-Si:H TFT on a flat polyimide substrate after fabrication.

consisting of Si dangling bonds, determine the threshold voltage. In amorphous silicon TFTs, the field-effect mobility is determined by frequent trapping in the conduction-band tail states [36,37]. The slopes of the conduction- and valence-band tails are correlated [38] and controlled by the amount of structural and thermal disorder. In our work, during the final substrate deformation, the device islands were subject to extreme mechanical strain, which could change the width of the band tails and other material properties. Consequently, the device characteristics changed after deformation. The relationship between the applied mechanical strain and the electrical performance (especially mobility) will be discussed in Section 5.5.

In our experiment, the threshold voltage ( $V_{th}$ ) and the electron mobility ( $\mu_n$ ) are calculated from the transfer characteristic in saturation at the drain-to-source voltage  $V_{ds}=10$  V using the MOSFET equations for the saturation region:

$$I_{ds} = \mu_n C_g \frac{W}{L} (V_{ds} - V_{th})^2, \quad V_{ds} \geq V_{gs} - V_{th} \quad (\text{saturation region}) \quad (5.1)$$

where  $I_{ds}$  is the drain-to-source current, and  $C_g$  is the gate capacitance per unit area.  $W$  is the width and  $L$  is the length of the channel region. The off-current ( $I_{off}$ ) is defined as the lowest  $I_{ds}$  at  $V_{ds}=10$  V, the on-current ( $I_{on}$ ) is the  $I_{ds}$  at  $V_{ds}=10$  V and  $V_{gs}=V_{th} + 10$  V. The gate leakage current is the  $I_{gs}$  at  $V_{ds} = 10$  V and  $V_{gs} = 20$  V. The subthreshold slope ( $S$ ) is obtained by fitting an exponential function to the subthreshold region of the transfer characteristic for  $V_{ds}=0.1$  V.

$$S = \frac{dV_{gs}}{d \log_{10} I_{ds}} \quad (5.2)$$

Amorphous silicon TFT device characteristics are known to drift with device operation [37]. The most important instability is the threshold voltage shift that is observed after the application of the gate voltage for long periods of time. It is due to two mechanisms; charge trapping in the silicon nitride gate insulation and metastable dangling bond state creation in the amorphous silicon [39,40]. Optimizing the amorphous silicon deposition process and annealing the final device structure in the forming gas could improve the TFT stability [41]. In our experiments, the TFT deposition condition was optimized accordingly [41] so that for the gate voltages and measurement times used here (I-V measurement sweep was done in less than 600 seconds), the change in device characteristics due to the instability of amorphous silicon was insignificant.

### 5.3 Thin-film Transistor Fabrication

From Chapter 4, we know that by patterning uniform semiconductor layers into isolated islands, small islands can be fracture-free after spherical deformation of the substrate. Thus, to achieve electronics on a spherical dome, a single device (or a small number of devices, if the island is large enough) must be fabricated on separate islands. Fig. 5.3 shows the structures of the a-Si:H TFTs fabricated in such islands with the conventional staggered bottom-gate, back-channel-etch structure. Before TFT fabrication, the polyimide foil was temporarily laminated to a 4-inch silicon wafer with a thin adhesive layer of silicone gel (Appendix A) to ensure substrate flatness during fabrication. The fabrication is a modified version of one used previously in our lab for a-Si:H TFTs on plastic substrates [27]. All amorphous silicon and silicon nitride layers were deposited using a three-chamber RF-excited plasma-enhanced chemical vapor

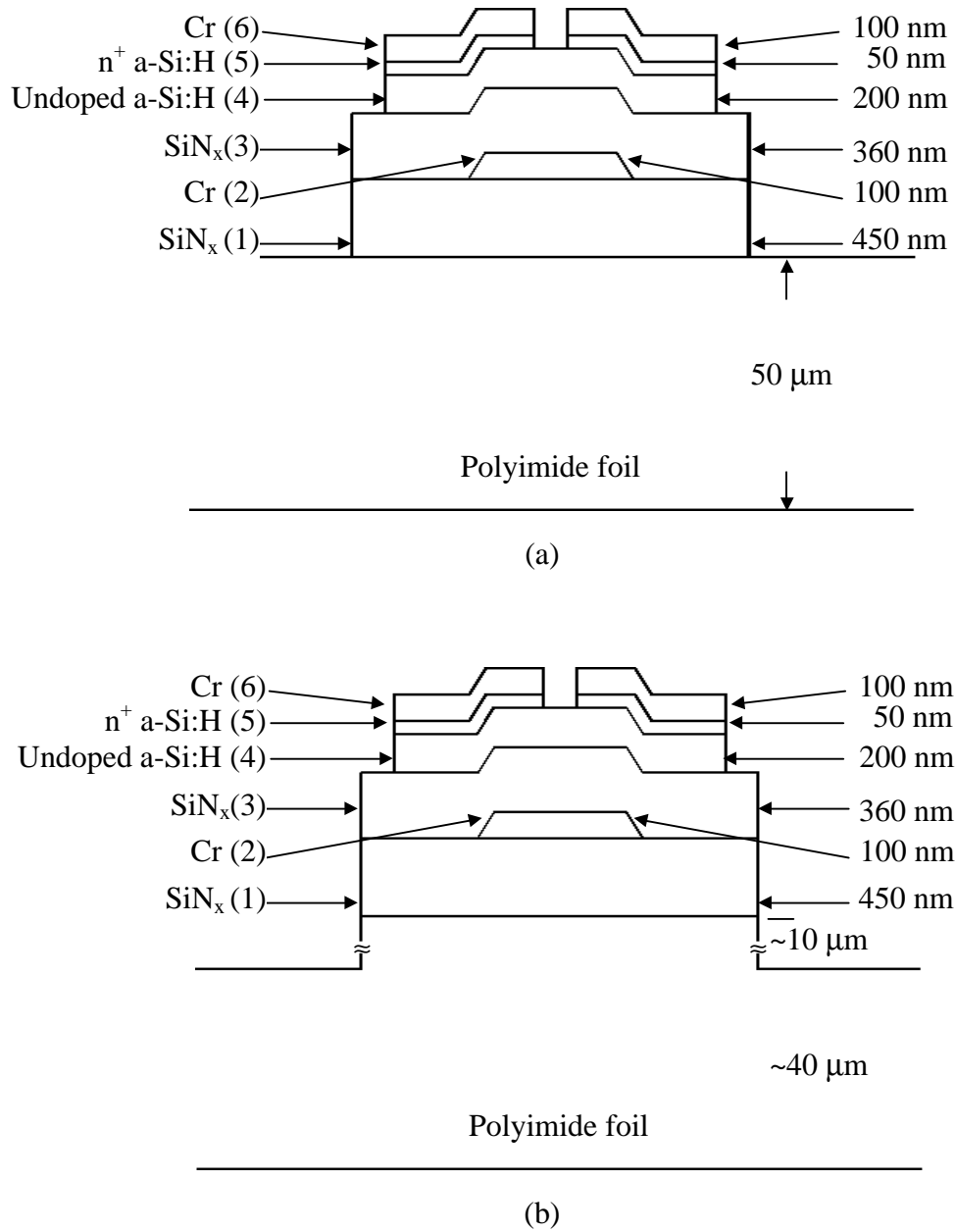
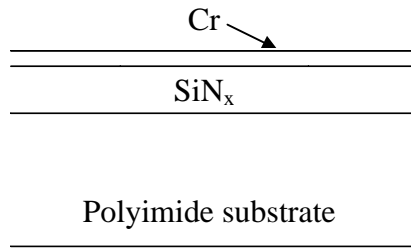
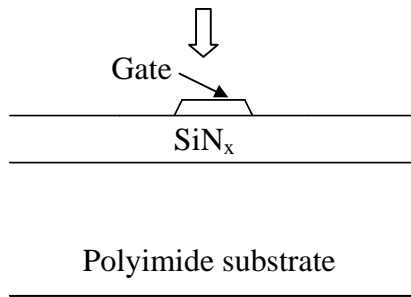


Fig. 5.3 (a) Cross section of the TFT planar island device structure, and (b) cross-section of the TFT-on-mesa structure.

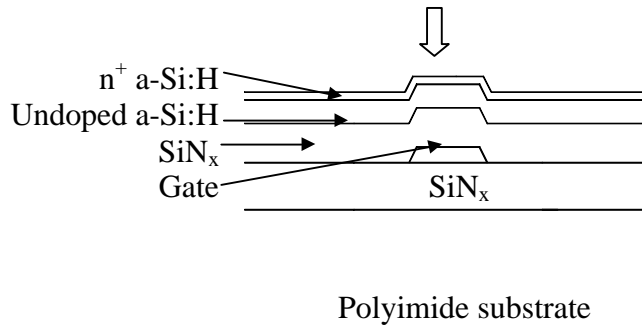
deposition system at 150°C substrate temperature (Appendix B). The polyimide substrate was first passivated with a 0.5- $\mu\text{m}$ -thick layer of  $\text{SiN}_x$  (layer 1) for planarization and chemical barrier. Next a 100-nm-thick Cr (layer 2) was thermally evaporated and wet-etched to create the gate electrode (Mask 1). The TFT tri-layer consisted of 360 nm of  $\text{SiN}_x$  (layer 3), 200 nm of undoped a-Si:H (layer 4), and 50 nm of  $\text{n}^+$  a-Si:H (layer 5). Another 100-nm-thick Cr layer (layer 6) was then evaporated and wet-etched to serve as the source-drain contact (Mask 2). The active region for the TFT was defined by reactive ion etching (RIE) of the  $\text{n}^+$  and undoped a-Si:H (layer 4 and 5) in a mixture of  $\text{SF}_6$  and  $\text{CCl}_2\text{F}_2$  using a photoresist mask. The transistors' channel regions were yet to be defined at this stage. The  $\text{SiN}_x$  (Layer 1 and 3) was then etched by RIE in a mixture of  $\text{CF}_4$  and  $\text{O}_2$ . Regions protected by photoresist then became isolated device islands, which would withstand the subsequent substrate expansion. This patterning step also etched windows into the  $\text{SiN}_x$  gate dielectric layer (layer 3) to create openings where the gate layer could be contacted. For TFTs on planar islands (Fig. 5.3(a)), after all device materials, including the nitride buffer layer (layer 1), were removed outside of the device island area, the channel region was then defined by removing  $\text{n}^+$  a-Si:H (RIE in  $\text{CCl}_2\text{F}_2$ ) between the source/drain contacts by using the initially defined Cr source/drain layer (layer 6) as a mask. The fabrication for planar TFTs was complete at this stage. The fabrication processes are illustrated in detail in Fig. 5.4. The top-view of a planar TFT is shown in Fig. 5.



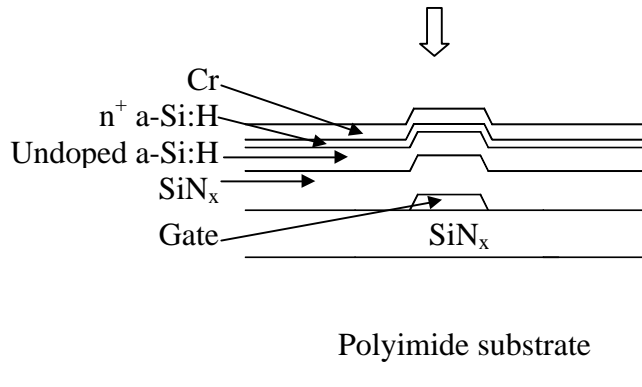
1.  $\text{SiN}_x$  deposition followed by Cr evaporation



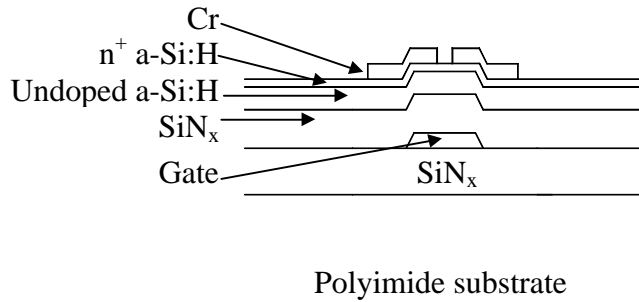
2. Cr patterned by wet etch to define the gate electrode (Mask 1)



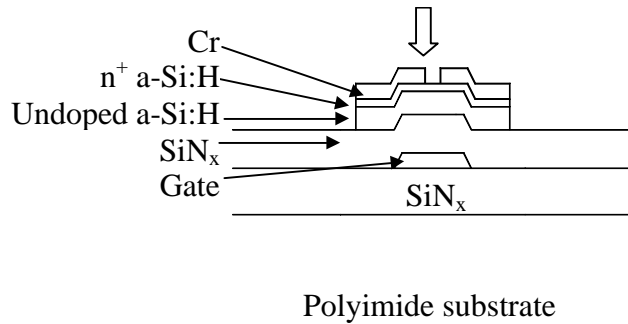
3.  $\text{SiN}_x$ , undoped a-Si:H,  $n^+$  a-Si:H deposition in PECVD



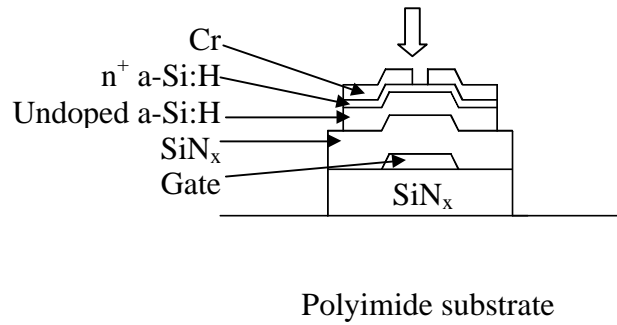
4. Cr evaporation



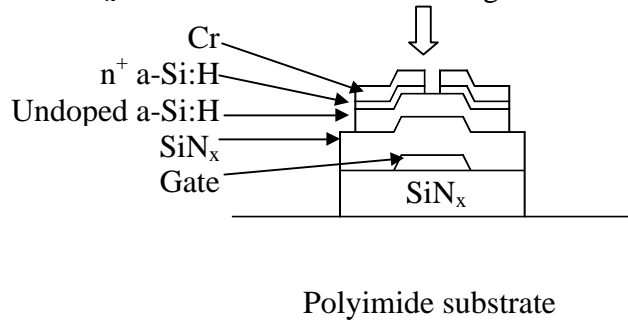
5. Cr patterned by wet etch to define the source and drain electrode (Mask 2)



6. a-Si:H and n+ a-Si:H patterned by RIE (Mask 3)



7. SiNx etched to create islands and gate contact hole (Mask 4)



8. n+ a-Si:H between the source/drain contacts dry etched to define channel region

Fig. 5.4 Fabrication process for TFTs on planar islands

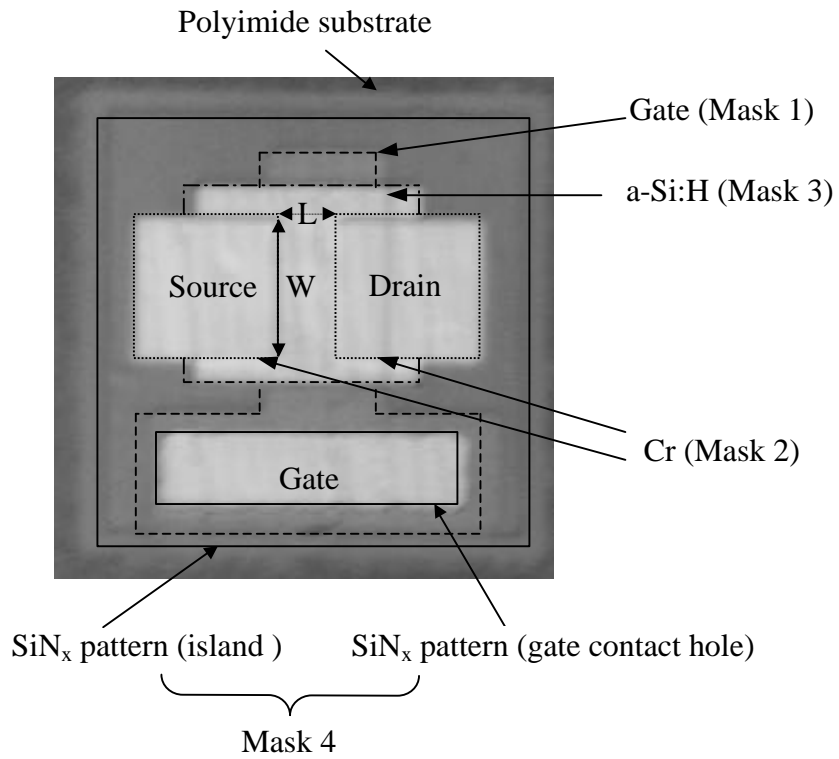


Figure 5.5 Top view of a TFT on a planar island.  $W$  is the channel width, and  $L$  is the channel length.

For TFTs on mesa islands (Fig. 5.3(b)), after gate nitride layer and buffer nitride were patterned to make device islands, the sample was etched with oxygen plasma to define the mesa pattern into the polyimide. The photoresist (from the previous  $\text{SiN}_x$  lithography step) and the device islands themselves served as masks.  $\sim 10\ \mu\text{m}$  deep polyimide pillars were etched. This step was followed by removing  $n^+$  a-Si:H in the channel region to complete the device fabrication process. The fabrication processes are illustrated in detail in Fig. 5.6. These flat devices were measured before the following deformation process.

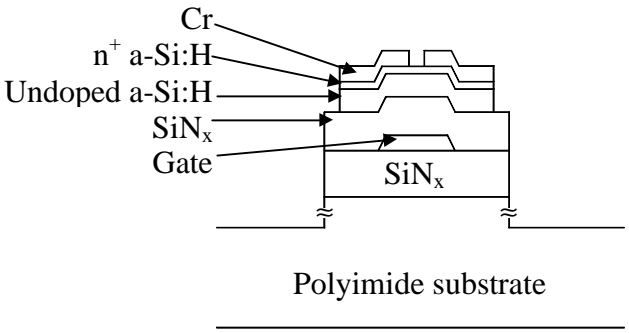
## 5.4 Amorphous Silicon Thin-Film Transistors on Spherical Domes

### 5.4.1 TFTs on planar islands

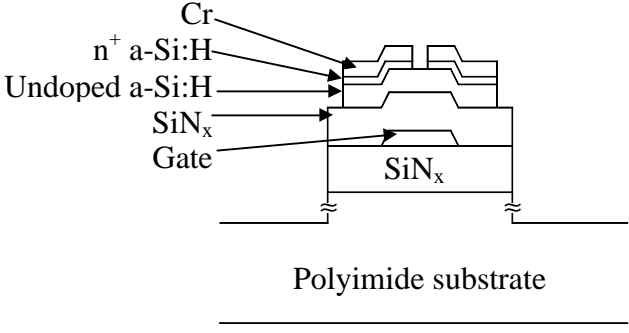
After device characteristics measurement, the sample was then peeled from the wafer and deformed at  $150^\circ\text{C}$  to a  $66^\circ$  field-of-view (one steradian) spherical dome, which corresponded to raising the center of the foil by  $\sim 0.90\ \text{cm}$ . After releasing the pressure, the height of the dome decreased to  $\sim 0.78\ \text{cm}$  due to the elastic relaxation of the substrate. After pressure release the dome curvature subtended a  $58^\circ$  field-of-view, corresponding to an average substrate radial strain  $\sim 4.5\%$ .

To measure the TFTs on a spherical dome, the deformed substrate was mounted on a solid spherical dome with the same shape to provide back support during measurement (See Appendix C). This is required because the probe tip can deform the soft hollow sphere dome during measurement when contacting the sample. To first order, the transistors are little affected by the deformation process [28]. Fig. 5.7 shows the transfer and gate leakage characteristic of the TFTs before and after deformation. All devices were measured near the top of the dome, where the strain in the substrates is the

Step 1~7: The same as the planar TFTs

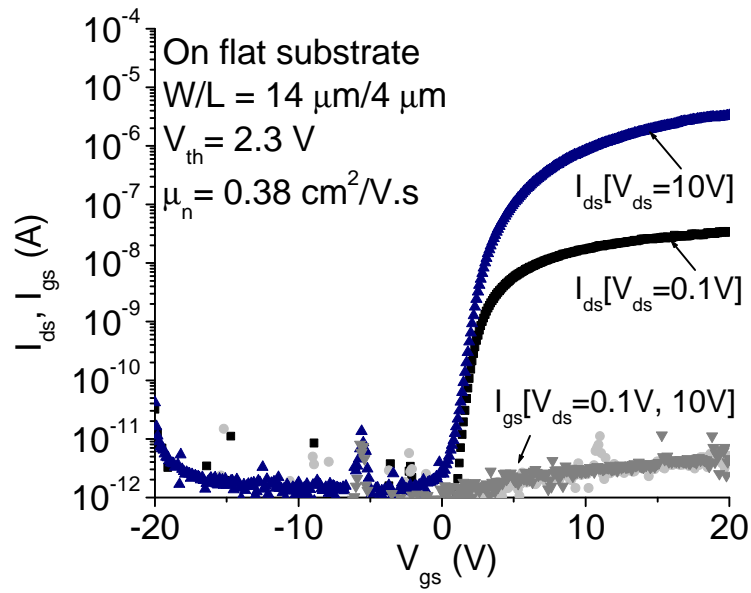


8. Polyimide substrate etched to create mesa islands

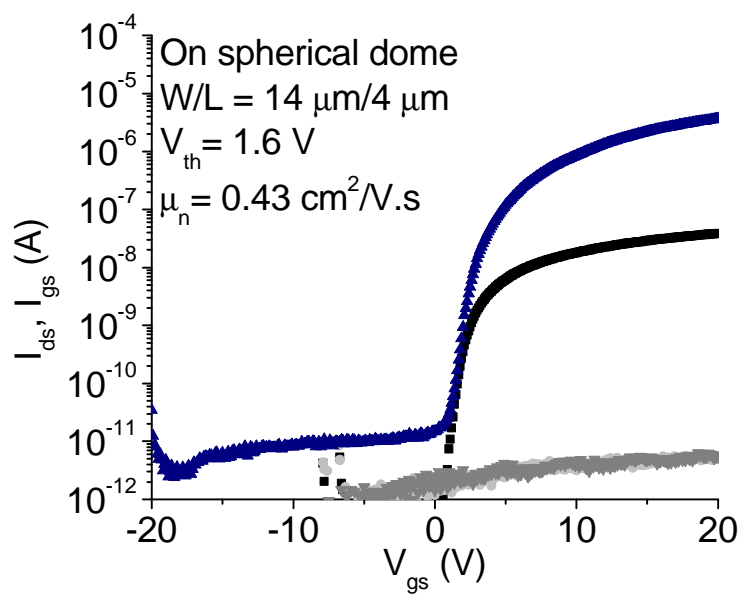


9. n+ a-Si:H between the source/drain contacts dry etched to define channel region

Fig. 5.6 Fabrication process for TFTs on mesa islands



(a)



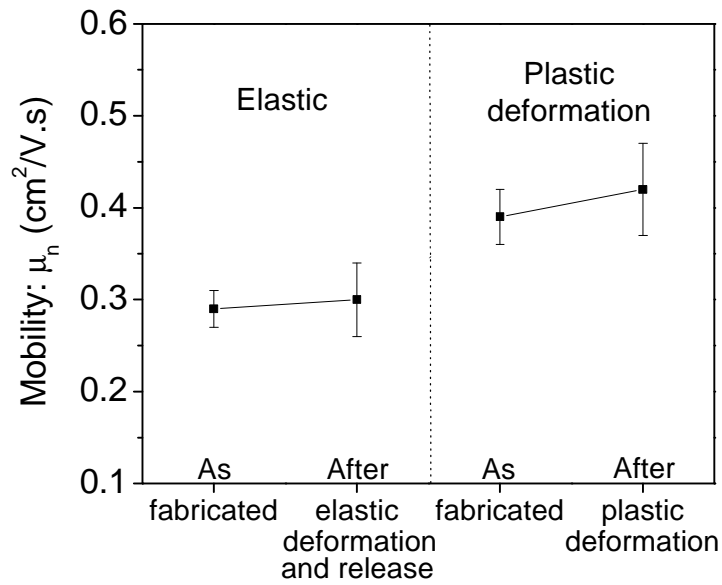
(b)

Fig. 5.7 TFT characteristics of the same planar a-Si:H TFT on a 40  $\mu\text{m}$   $\text{SiN}_x$  island with gate length  $L = 4 \mu\text{m}$  and gate width  $W = 14 \mu\text{m}$ , (a) after fabrication, and (b) after 150°C substrate deformation (to a height of  $\sim 0.78 \mu\text{m}$  after pressure release)

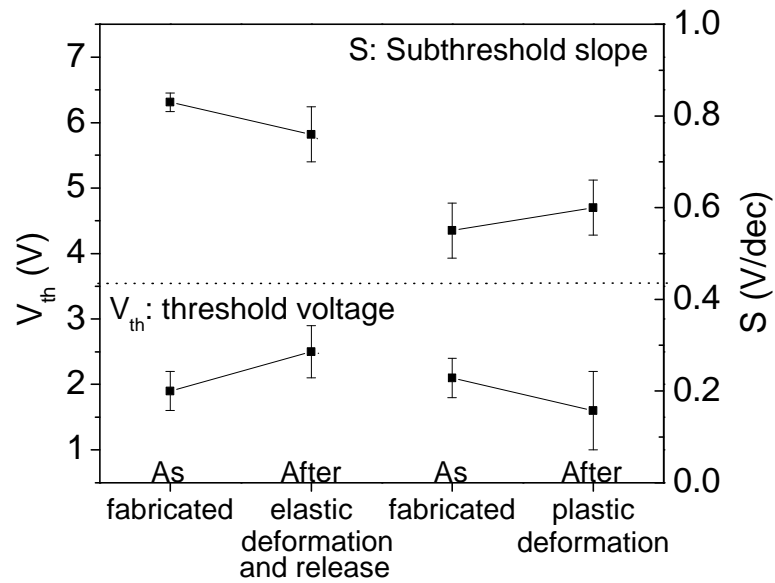
maximum and biaxial (Fig. 3.5). Deformation raised the average mobility (of 5 devices tested) from  $0.39 \text{ cm}^2/\text{Vs}$  to  $0.42 \text{ cm}^2/\text{Vs}$  (an increase of  $\sim 8\%$ ), and reduced the average threshold voltage from  $2.1\text{V}$  to  $1.6\text{V}$ . The subthreshold slope changed from  $0.55\text{V}/\text{dec}$  to  $0.60\text{V}/\text{dec}$ . The gate currents remained below  $1 \times 10^{-11} \text{ A}$  ( $< 2 \times 10^{-13} \text{ A}/\mu\text{m}^2$ ).

To further probe the effects of deformation, a polyimide substrate with a separate batch of similarly fabricated devices was deformed into a spherical dome with a  $30^\circ$  field-of-view, which corresponded to raising the center of the foil by  $\sim 0.40 \text{ cm}$  (average radial strain in the substrate  $\sim 1\%$ ) when the pressure was applied. Because the strain was low, the deformation of the substrate was elastic, and could be done at room temperature. After the pressure was released, the substrate returned to its original shape. In this case, the threshold voltage changed from  $1.9\text{V}$  to  $2.5\text{V}$ , and the mobility changed from  $0.29 \text{ cm}^2/\text{Vs}$  to  $0.30 \text{ cm}^2/\text{Vs}$  (average of 5 devices), an increase of only  $3\%$ , which was less than the accuracy of the measurement, showing that the effect of elastic substrate deformation was reversible. This demonstrates that the change in mobility in the previous case (spherical deformation) is due to the plastic substrate deformation. These results are summarized in Fig 5.8. (The difference in initial as-fabricated characteristics for these three groups is within the normal variability of research-grade TFT processing from substrate to substrate in our single substrate deposition system.)

Note that mobility showed less scatter and was more reproducible than the threshold voltage. It could be due to the fact that the mobility depends on the properties of amorphous silicon, which are more reproducible than the causes of trapping in silicon nitride and of the dangling bond instability, which will affect the threshold voltage.



(a)



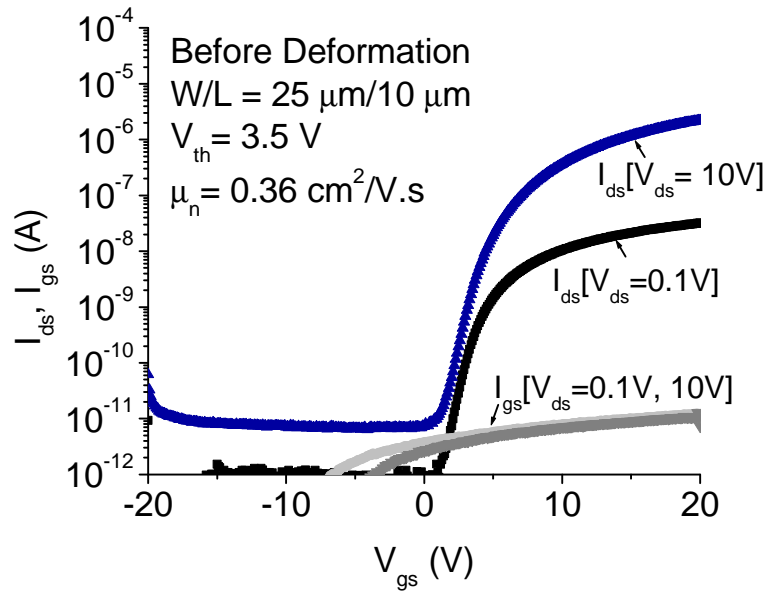
(b)

Fig. 5.8 Comparison of TFT ( $40\mu\text{m}$  device islands) characteristics (average of 5 devices): (a) electron mobility ( $\mu_n$ ), (b) threshold voltage ( $V_T$ ) and subthreshold slope (S). The first sample was elastically deformed and released, and the second sample was plastically deformed (to a height of  $\sim 0.78$  cm after pressure release) at  $150^\circ\text{C}$ .

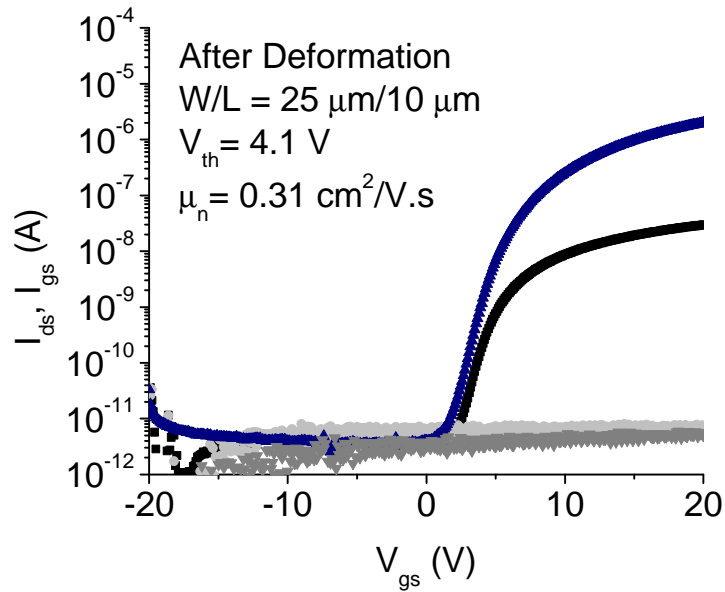
### 5.4.2 TFTs on mesa islands

To study the effects of the mechanical strain alone, it was desirable to design a device structure with lower strain so the plastic substrate deformation could be done at room temperature. The solution we used here was the mesa island structure (Fig. 5.3(b)). The spherical deformation (a height of  $\sim 1.00$  cm, which is a  $74^\circ$  field-of-view, corresponding to an average radial strain  $\sim 7\%$ ) was done at room temperature. After pressure release, the dome relaxed back to a spherical dome of a height of  $0.75$  cm (a  $56^\circ$  field-of-view, corresponding to an average substrate radial strain  $\sim 4\%$ ). TFTs with  $\text{SiN}_x$  islands smaller than  $90\ \mu\text{m}$  remained crack-free after deformation. Fig. 5.9 shows the transfer and gate leakage characteristic of a TFT on a  $90\ \mu\text{m}$   $\text{SiN}_x$  island before and after deformation. The off-current and leakage current did not change significantly (for an average of 5 devices), but the electron mobility decreased (4%) and the threshold voltage increased (14%) after deformation (Fig. 5.10).

The fact that only smaller islands remained intact after deformation indicated that strain in the island increased with its size. Therefore, if the changes in the electrical properties after deformation were due to the resulting mechanical strain, islands of different sizes would be expected to behave differently. Fig. 5.10 (a) summarized the changes in electron mobility after deformation for islands of different sizes. (Such measurements vs. island size were not possible in the case of planar islands because with planar islands, only one island size ( $40\ \mu\text{m}$ ) was large enough for TFTs with probe pads and consistently did not crack, even with deformation at  $150^\circ\text{C}$ .) Some of the islands had different device lengths and widths, which might affect a comparison of the absolute mobilities due to differences between actual device dimensions and those on the mask.

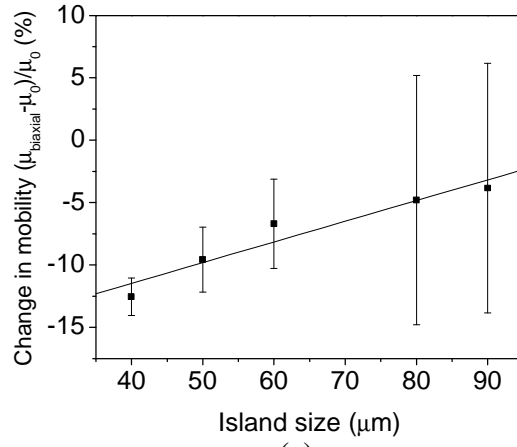


(a)

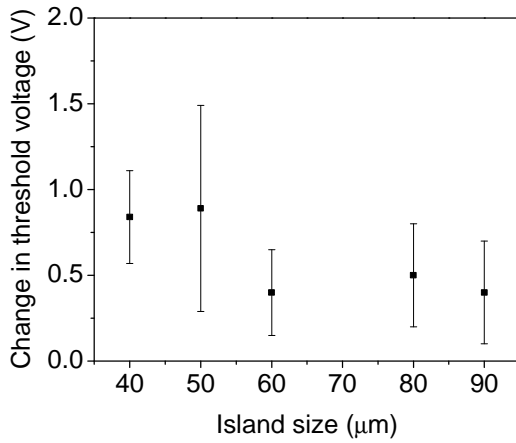


(b)

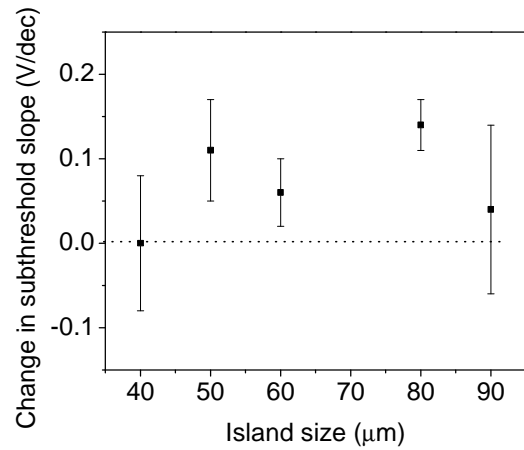
Fig. 5.9 Mesa TFT characteristics, for a device on a  $90 \mu\text{m}$   $\text{SiN}_x$  island with gate length  $L = 10 \mu\text{m}$  and gate width  $W = 25 \mu\text{m}$ , (a) after fabrication, and (b) after room temperature deformation (to a height of  $\sim 0.75 \text{ cm}$  after pressure release).



(a)



(b)



(c)

Island size (μm)	40	50	60	80	90
Gate width W (μm)	14	20	20	25	25
Gate Length L (μm)	4	6	10	10	10

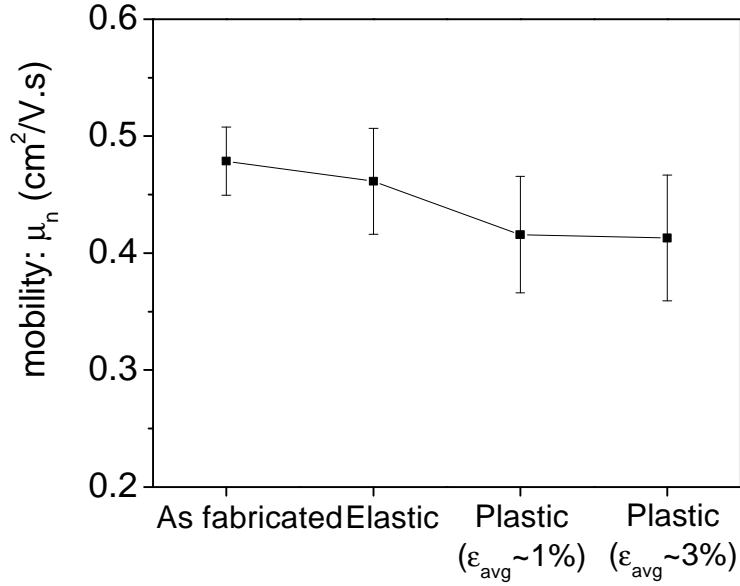
Fig. 5.10 Change in (a) electron mobility of mesa TFTs after deformation for islands of different sizes, (b) threshold voltage, and (c) subthreshold slope. (average of 5 devices)

However, this would not affect the relative change in each device due to deformation, which is shown in Fig. 5.10. The data demonstrate that the mobility decreased after deformation, and that on average, the decrease was larger in smaller islands.

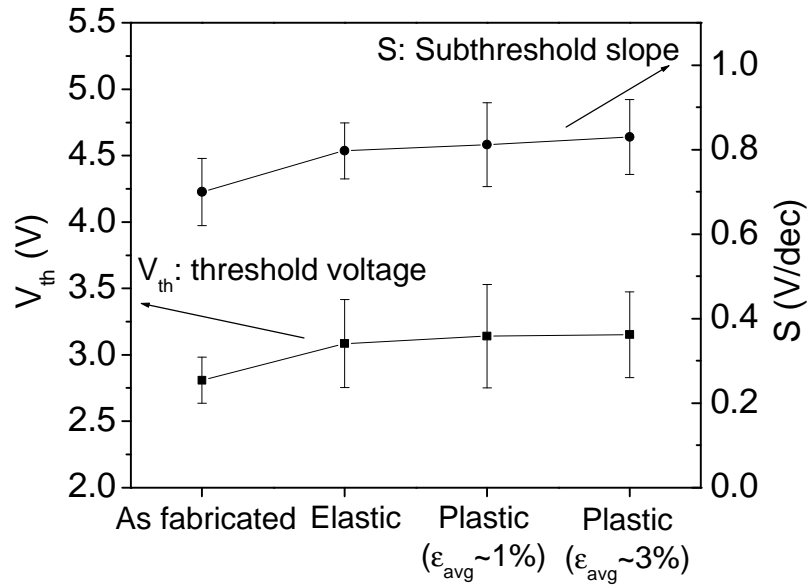
Fig. 5.10(b) and Fig. 5.10(c) show that though there is no clear trend with island size, the threshold voltage and subthreshold slope increased after deformation. Although we are not certain, we assume that the increase in the threshold voltage and the subthreshold slope reflected the usual dangling-bond instability of a-Si:H TFTs [39] since the threshold voltage and subthreshold slope changed significantly even for elastically deformed sample. That the mobility changed more consistently with deformation was also observed in the planar TFTs in the previous section. Therefore our discussion on mobility of the effect of strain on device characteristics (Sec. 5.5) will focus on mobility, which does have a consistent trend with strain.

To study the effects of strain on mobility due to multiple deformations, a separate set of devices of mesa structures was fabricated [42]. The polyimide pillars for this sample were  $\sim 8 \mu\text{m}$  deep. The same sample was deformed 3 times. In the first experiment, we deformed the substrate into a spherical dome with a height of  $\sim 0.45 \text{ cm}$  (a  $36^\circ$  field-of-view, corresponding to average strain  $\sim 1.5\%$ ) when the pressure was applied. Because the strain was low, the deformation in the substrate was elastic. After the pressure was released, the substrate returned to its original planar shape. The TFT characteristics after this elastic deformation were measured. The substrate was then deformed again into a spherical dome with a height of  $\sim 0.65 \text{ cm}$  (a  $50^\circ$  field-of-view, corresponding to average strain  $\sim 3\%$ ). The deformation was permanent with a height of  $0.40 \text{ cm}$  (a  $30^\circ$  field-of-view, corresponding to average strain  $\sim 1\%$ ) after pressure release.

Again the TFT characteristics were measured. Finally, the substrate was deformed into a spherical dome a height of ~0.90 cm (a 66° field-of-view, corresponding to average strain ~6%). After pressure release, the dome was with a height of ~0.65 cm (a 50° field-of-view, corresponding to average strain 3%) and the TFTs were measured again. The results are summarized in Fig. 5.11 (The devices shown here are all on a 40  $\mu\text{m}$   $\text{SiN}_x$  island with gate length  $L=4\ \mu\text{m}$  and gate width  $W=14\ \mu\text{m}$ ). The mobility ( $\mu_n$ ) decreased very slightly, and the threshold voltage ( $V_{th}$ ) increased after the first elastic deformation. After the last deformation, ~10% increase in  $V_{th}$  and ~14% decrease in  $\mu_n$  were observed. Note that while the device-to-device variation of the mobility before deformation was large (standard deviation =  $0.03\ \text{cm}^2/\text{Vs}$ , which was 6% of the average), the decrease in mobility in each device was more consistent. For example, the average decrease was  $0.07\ \text{cm}^2/\text{Vs}$  or 14%, with standard deviation of  $0.05\ \text{cm}^2/\text{Vs}$ . No substantial changes in the  $I_{off}$  and the gate-leakage current were recorded.



(a)



(b)

Fig. 5.11 Mesa TFT characteristics after elastic deformation, first spherical deformation (a height of  $\sim 0.40$  cm after pressure release), and second spherical deformation (a height of  $\sim 0.65$  cm after pressure release) (average of 10 devices): (a) electron mobility ( $\mu_n$ ), and (b) threshold voltage ( $V_{th}$ ) and subthreshold slope (S).

## 5.5 Discussion of TFT Electrical Performance Under Mechanical Strain

In Section 5.4, we demonstrated two device structures; TFTs on planar islands and TFTs on mesa islands. The mobility of TFTs on 40- $\mu\text{m}$  planar islands increased  $\sim 8\%$  (Fig. 5.11(a)), but the mobility of TFTs on 50- $\mu\text{m}$  mesa islands (10- $\mu\text{m}$  tall pillars) decreased  $\sim 10\%$  after substrate deformation (Fig. 5.10(a)). Furthermore, the change in the mobility of TFTs on mesa islands showed a monotonic trend with the device island size, which suggested that the change in the mobility was due to the strain in the island. The change in mobility with strain can be explained by the fact that the mechanical strain changes the structural disorder of the amorphous silicon, which affects the effective mobility of the electrons. In this section, we will first review previous work on the relationship between one-dimensional strain and its effects on electrical properties of amorphous silicon devices [43-45]. In the second half of the section, we will discuss, through experimental data and finite element analysis, the change in electrical characteristics of our a-Si:H TFTs due to spherical deformation (biaxial strain).

### 5.5.1 Amorphous silicon TFTs under uniaxial strain

Gleskova et al. reported that the electron mobility of a-Si:H TFTs similar to those used in this study depended on the applied uniaxial strain under cylindrical bending (remaining within elastic limits) [45]. The devices were measured while the elastic strain was applied, not after it was released as in Sec. 5.4 in this work (where negligible change was seen after the release of the elastic deformation (Fig. 5.8)).

The electron field-effect mobility increased under tension, and decreased under compression. The relation is linear:

$$\mu_{uniaxial} = \mu_0(1 + 26\epsilon) \quad (6.1)$$

where  $\mu_0$  is the mobility without strain (devices as fabricated).  $\epsilon$  represents the uniaxial strain in amorphous silicon, which is parallel to the direction of the source-drain current. The strain was calculated from the geometry of bending using Eq. 2.1. The tensile strain has a positive sign. The change in the device characteristic is reversible. The mobility went back to its original value after the release of strain. Gleskova et al. reported that the change in the mobility is slightly smaller for TFTs when the strain is perpendicular to the direction of the current in the channel [45].

The change in the mobility of a-Si:H TFTs under external strain is similar to the changes in the dark conductivity of blanket a-Si:H films due to the piezoresistive effect. The conductance of a-Si:H films increases with increasing uniaxial tensile strain and decreases with compressive strain. The magnitude of the change depends on the directions of the applied strain with respect to the current path. The maximum change occurs when the strain is parallel to the current path [46].

a-Si:H TFTs consist of several layers. Gleskova et al. concluded that the change in the mobility after deformation could be explained by the change in contact resistance between doped and undoped a-Si:H layers and the broadening of the conduction band tail of the a-Si:H channel material under compression due to the strain-induced disorder, although it was not clear which of these two explanations was the dominant effect [45].

Although there was a monotonic trend in the  $\mu_{uniaxial}$  as a function of applied strain, Gleskova et al. reported there was no clear trend in the change of the threshold voltage ( $V_{th, uniaxial}$ ) and the subthreshold slope ( $S_{uniaxial}$ ): the subthreshold slope increased when the TFTs were subject to compression, and the  $V_{th, uniaxial}$  slowly increased even

when the tensile strain was gradually decreased [46]. The consistent behavior of mobility and inconsistent behavior of the threshold voltage were similar to our work. Further study is needed to determine the primary mechanism causing the reversible mobility changes and to detect concurrent changes in the threshold voltage, and the subthreshold slope.

### 5.5.2 Amorphous silicon TFTs under biaxial strain

In this section, we will compare the mobility changes in devices after plastic spherical deformation (and release) with the resulting final strain in the TFTs. From the previous discussion on TFTs under uniaxial strain, we learned that applying strain either parallel or perpendicular to the direction of the source-drain current could change the field-effect mobility, with the parallel direction having slightly larger effects. For simplicity, we assume the effects of biaxial strain on the mobility is the superimposition of the effects due to uniaxial strain in the parallel and the perpendicular directions, and that the effect in the perpendicular direction is equal to that described in Eq. 6.1 for the parallel direction:

$$\mathbf{m}_{biaxial} = \mathbf{m}_0(1 + 52\epsilon) \quad (6.2)$$

where  $\mu_0$  is the mobility without strain (devices as fabricated), and  $\epsilon$  represents the biaxial strain in the channel region. Because amorphous silicon is a continuous random network with no structural order extending beyond second-nearest-neighbor distances, direct measurement of the strain distribution is difficult. We used finite element numerical modeling (Chapter 4) to calculate the strain distribution in the semiconductor island in the following discussion.

### 5.5.2.1 Planar devices and tensile strain

In Chapter 4, we modeled a round 1- $\mu\text{m}$ -thick, 50- $\mu\text{m}$ -diameter amorphous silicon island on a 50- $\mu\text{m}$ -thick polyimide substrate to represent a planar silicon island deformed at 150°C. The condition was set that the substrate was stretched to 6% average strain in the radial direction and then relaxation back to 5% average strain in the substrate after pressure release. Fig. 5.12 shows the radial and circumferential strain in the silicon island as a function of position. The radial strain at the center of the island at the maximum deformation is ~0.33% (tension) while pressure is applied. After the pressure is unloaded the strain is reduced to ~0.29%. Note strain is at maximum (and also biaxial) at the center of the island (channel region of the device).

Assuming the earlier relation of  $m_{biaxial} = m_0(1 + 52\epsilon)$  for biaxial strain in amorphous silicon (Eq. 6.2), the relative increase of mobility for a biaxial strain of 0.29% along the direction of the channel is 14%. While of the correct sign and order of magnitude, this result is 1.75 times larger than our experimental results of planar structures (devices with an increase of ~8% in mobility after deformation).

Three reasons could cause this discrepancy. First, the substrate deformation of the planar devices was done at 150°C, and such heating could also change the dependence of mobility on strain from that at room temperature as was measured by Gleskova et al. [45]. (As described in Chapter 4, deforming devices at room temperature is not possible with this structure because the fracture free islands are too small (only 20- $\mu\text{m}$  islands) for device characterization). Second, due to the uncertainties in the mechanical properties of device materials used in the finite element analysis, and the simplicity of the model (e.g. round islands in the numerical model vs. square islands in

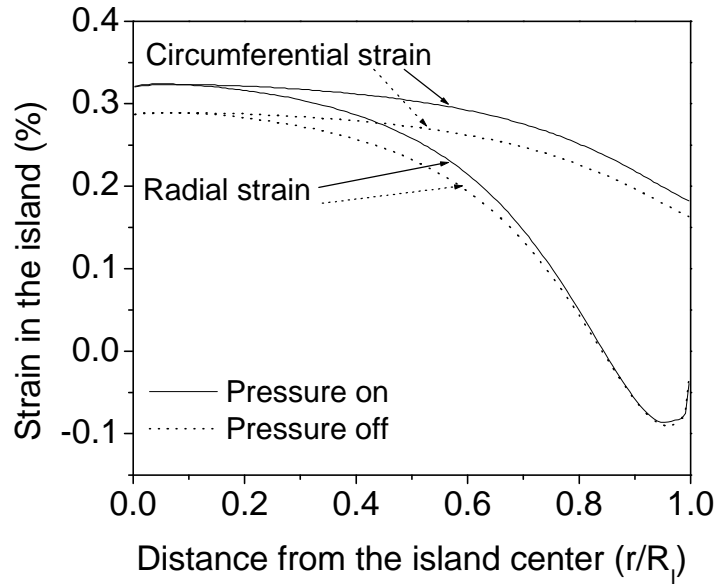


Figure 5.12 Predicted strain in a round amorphous silicon island (thickness = 1  $\mu\text{m}$ , diameter = 50  $\mu\text{m}$ ) after the polyimide substrate (50- $\mu\text{m}$  thick) is deformed with 6% strain and relaxed to 5% strain in the substrate as a function of position, using the estimated 150°C mechanical properties of polyimide of Table 3.2.

the experiment), the exact strain in the device is uncertain. The device is also not uniform over the island as assumed in the model. Third, the simple assumption of Eq. 6.2 that the applied strain parallel and perpendicular to the current path has equal effects could be incorrect. We conclude that qualitatively, the planar devices are in tension; however, at present not enough is known to quantitatively predict the mobility change of the planar a-Si:H TFTs from the predicted strain.

### **5.5.2.2 Mesa devices and compressive strain**

In Chapter 4, we learned that mesa islands could be in compression even if the substrate was stretched to 6% average strain due to the extreme deformation at the polyimide mesa edge. It is our conclusion that compression is the cause of the decrease of the mobility in the mesa island devices after deformation as opposed to the increase in mobility for planar devices. Fig. 4.12 shows the modeled radial strain as a function of radius in a round amorphous silicon island (thickness = 1  $\mu\text{m}$ , diameter = 50  $\mu\text{m}$ ) on a 10- $\mu\text{m}$  polyimide mesa after the polyimide substrate (50- $\mu\text{m}$  thick) is deformed with 6% strain and relaxed to 4% average strain. The negative radial strain at the center indicates that the islands are in compression during deformation for the mesa structure. The radial strain is  $\sim -0.09\%$  (compression) when pressure is applied. After the pressure is released, the strain changes sign and its magnitude is increased to  $\sim -0.11\%$ .

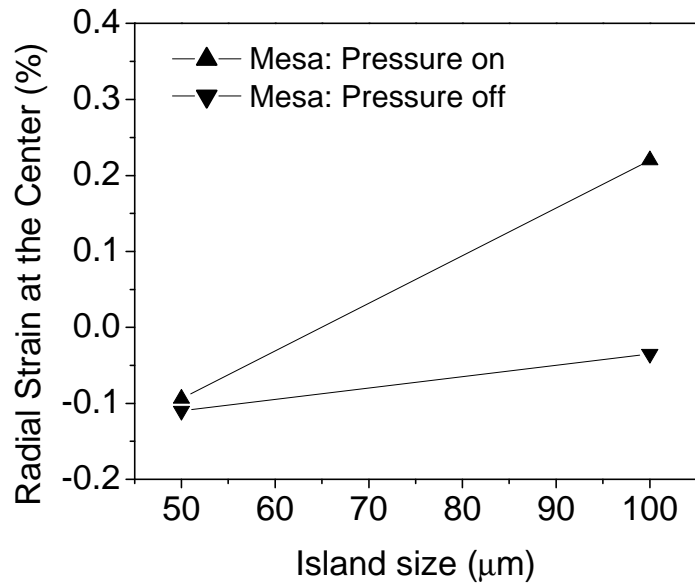
Fig. 5.10(a) shows experimental data showing that the mobility of TFTs on such mesa pillars decreased after deformation, with a larger decrease observed on smaller islands than on larger islands (e.g. 5% reduction in mobility on 100  $\mu\text{m}$  islands vs. 12% reduction in 40  $\mu\text{m}$  islands.). This is qualitatively consistent with the results from numerical modeling. Fig. 5.13(a) shows that strain from finite element analysis depends

monotonically on island size and smaller mesa islands have a higher compressive strain. Fig. 5.13(b) shows the change in mobility predicted by the modeled radial strain vs. island size and the experimental data under the assumption that the mobility due to biaxial strain is the superimposition of the effect of uniaxial strain in the parallel and the perpendicular directions (Eq. 6.2). The correlation of a more pronounced mobility reduction in small islands is clear, although the quantitative agreement is not good. Reasons for a lack of better quantitative agreement could include modeling limitations (i.e., uncertainties in the mechanical properties of device materials, the differences in the strain of a complicated TFT structure vs. that of the round single-layer island model, etc), and the uncertainties in the piezoelectric effects of amorphous silicon TFTs under biaxial strain.

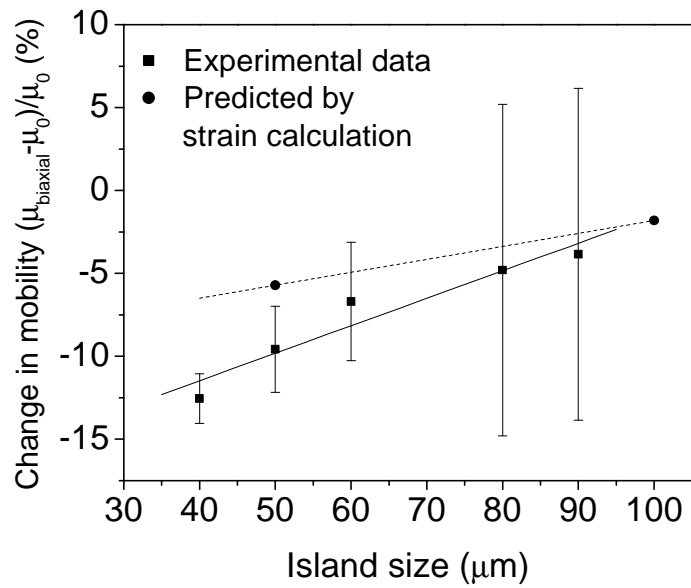
### 5.5.2.3 Elastic deformation of TFTs under biaxial strain

Fig. 5.8 and Fig. 5.11 showed that elastic deformation had little effect on the electron mobility. For planar devices with 40- $\mu\text{m}$  islands, the mobility increased by only 3% compared to the 8% increase in mobility after the spherical deformation (to 66° field-of-view) of the substrate (Fig. 5.8). For mesa devices ( $\sim 8\text{-}\mu\text{m}$  tall polyimide pillars) with 40- $\mu\text{m}$  islands, the mobility decreased by only 4% compared to the 10% decrease in mobility after the spherical deformation (to 66° field-of-view) of the substrate (Fig. 5.11) and mesa structures (decreased by only 4%). We conclude that elastic deformation at room temperature does not significantly permanently alter mobility, which is consistent with previous work on uniaxial cylindrical deformation [5].

In our experiments, there was no clear relationship between island size and changes in the threshold voltage and subthreshold slope. Previous work on blanket a-Si:H films showed that compressive hydrostatic pressure reduced the optical band gap [47]. While it has been shown that a decreased optical band gap leads to a reduced mobility [48] in a-Si:H, there is no clear correlation between the optical band gap and changes in the threshold voltage [49]. This demonstrates that the relationship between threshold voltage shift and strain is not understood, and requires further investigation.



(a)



(b)

Fig. 5.13 (a) Finite element analysis of the radial strain in the center of a 1-μm thick island on a 10-μm polyimide mesa as a function of the island size, both as pressure is applied to achieve 6% strain in the substrate and after pressure release (4% strain in the substrate), and (b) experimental data of the change in mobility and that predicted by modeled strain at island center in (a).

## 5.6 Chapter Summary

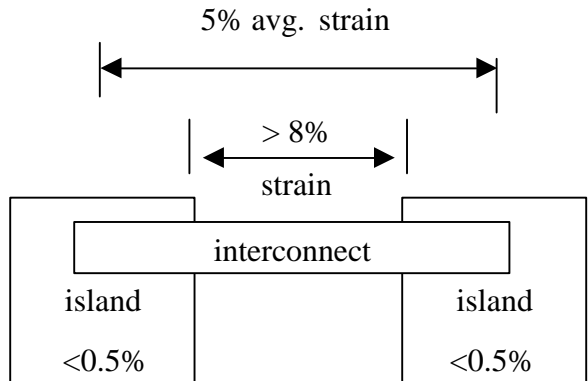
This chapter discussed the effects of spherical deformation of the plastic substrates on TFTs. We presented two device structures: TFTs on planar islands and TFTs on mesa islands. TFTs on planar islands have to be deformed at high temperature (150°C) to increase the size of crack-free islands after deformation. TFTs on mesa islands could be deformed at room temperature with island size as large as 90  $\mu\text{m}$ . In the majority of the TFTs, the off-current and gate leakage current do not change substantially, and the devices were still well-behaved after deformation. The mobility of TFTs on 40- $\mu\text{m}$  planar islands increased  $\sim 8\%$  after substrate deformation, but the mobility of TFTs on 40- $\mu\text{m}$  mesa islands decreased  $\sim 12\%$  after substrate deformation and demonstrated a linear trend with island size. The threshold voltage and subthreshold slope of TFTs on mesa islands increased after substrate deformation, and such increase so far seemed to be independent of island size.

The strain in device islands after such spherical deformation is biaxial, and is related to the island geometry. Though the substrate is plastically expanded to a spherical dome, device islands can experience either tension or compression depending on the deformation conditions: In mesa type structure, silicon films on top of the pillars could be in compression after the dome deformation, leading to a decrease in mobility after deformation. Tensile strain caused higher mobility in planar structures. We related the change in mobility to the mechanical strain due to the spherical deformation and had good agreement qualitatively.

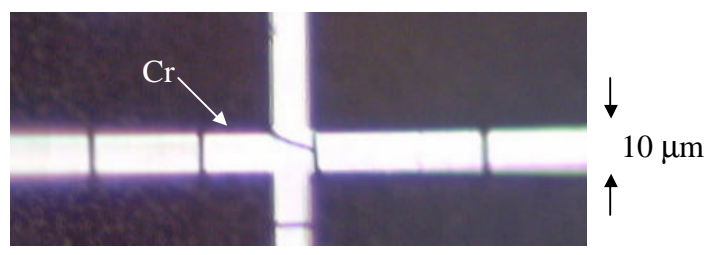
# Circuits on Spherical Domes

## 6.1 Introduction

The fabrication of circuits over large areas requires metal interconnects between device islands. Because most of the deformation takes place between the device islands, the local strain in the region between the islands far exceeds the average value (Fig. 4.8). In the present experiment, the local strain between islands is more than 8%. Consequently, metal interconnect lines made between device islands before deformation would fracture during deformation (Fig. 6.1). If the metals were deposited on the foil after deformation, a straightforward approach to patterning it would require photolithography and alignment on the sphere, for which no simple technology exists. This obstacle was overcome with a lift-off approach in which photoresist patterned before deformation was used to pattern metal deposited after deformation. This lift-off process was used to make simple circuits, such as inverters. The results demonstrate that the concept of stiff circuit islands fabricated on deformable foil substrates is a promising approach to electronics on surfaces with arbitrary shapes.



(a)



(b)

Figure 6.1 Interconnect problem: (a) Schematic diagram showing that the local strain between islands is more than 8%. (b) Cr interconnect lines ( $\sim 0.15 \mu\text{m}$  thick) deposited before deformation fracture during deformation.

## 6.2 Interconnect Patterning by Lift-off Process Using Deformed Photoresist

Because metal interconnect lines made before deformation fracture during deformation, it is desirable to put the metal layer onto the substrate after the substrate is already deformed. However, it is challenging to pattern metal layers on a spherical dome using conventional planar technologies. We noticed that the photoresist layer was soft and could be deformed with the substrate without cracking. Therefore, we adapted this “lift-off” method to achieve circuits on a spherical dome [28]. We first fabricated planar TFTs (Fig. 5.3 (a)). After the devices were fabricated, a layer of photoresist was patterned by conventional photolithography on the flat substrates. The substrate was then deformed at 150°C to a 60° field-of-view spherical dome (which corresponded to raising the center of the foil by ~0.80 cm). After pressure release, the dome curvature was reduced to a 50° field-of-view due to the elastic relaxation of the substrate.

During the deformation process, the photoresist underwent a large plastic deformation (8%) without cracking. A 450-nm-thick Al layer was thermally evaporated on the dome after deformation, and then patterned using the lift-off techniques by stripping the photoresist (using Baker PRS 1000 positive photoresist stripper). The pull-down and pull-up transistors on different islands were connected through this process to form an inverter circuit (Fig. 6.2). The characteristics of an inverter made on a spherical dome are shown in Fig. 6.3(b). The transfer curve of the inverter begins to switch at input voltage of ~2V, corresponding to the threshold voltage of the pull-down transistor as expected. The drop of the output voltage for high input voltage is limited by the fact

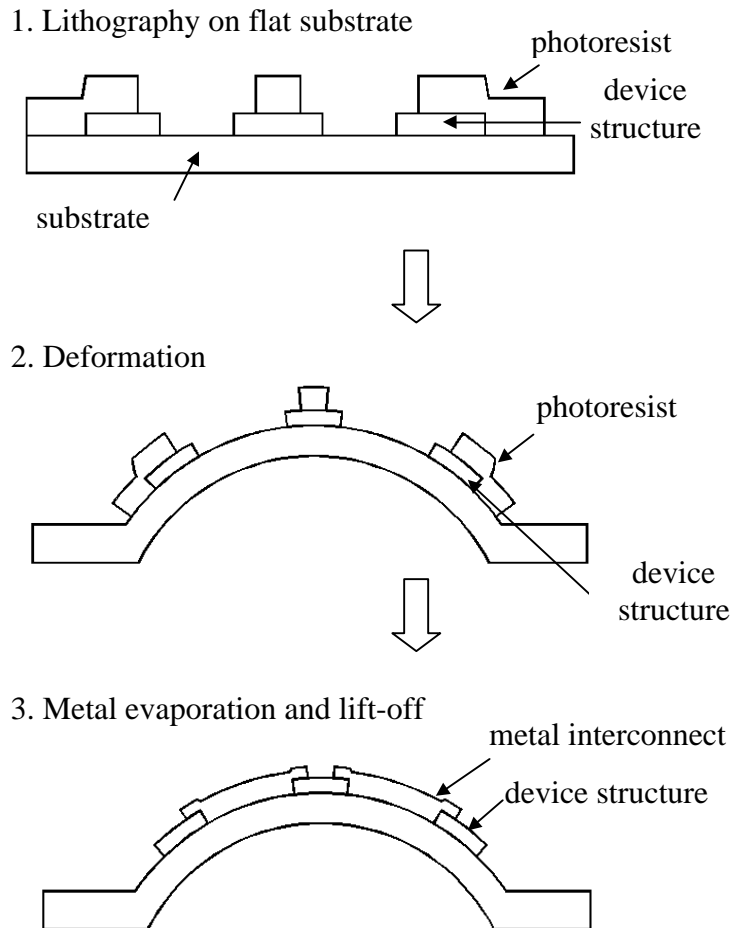
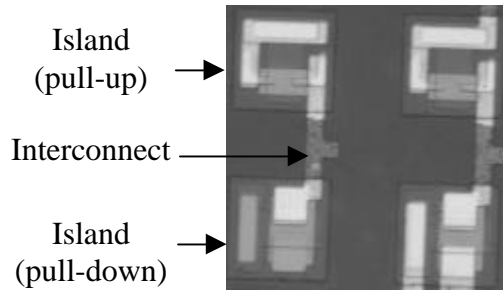
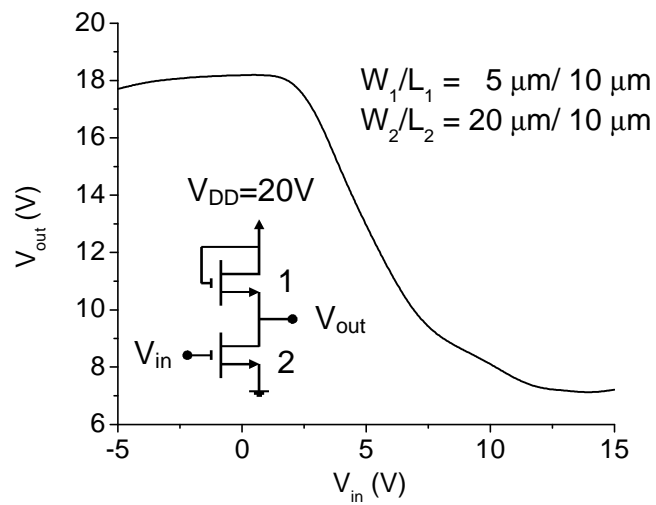


Fig. 6.2 Lift-off process for patterning metal deposited *after* deformation to  $\sim 60^\circ$  field-of-view using conventional *planar* lithography for photoresist patterning *before* deformation. The TFTs metallization and contact hole on the device islands are not shown for simplicity.



(a)



(b)

Fig. 6.3 Inverter pairs: (a) TFTs interconnected by lift-off process described in Fig. 6.2, and (b) transfer curve of inverters on spherical dome [28].

that the pull-up transistor does not turn off when the input is high as it does in CMOS circuit with a p-channel pull-up.

## 6.3 Other Schemes for Interconnect Fabrication

### 6.3.1 X-Y crossovers

The interconnects made by lift-off using pre-patterned photoresist that is deformed plastically together with the substrate demonstrate a viable approach for achieving electronics on arbitrary surfaces. However, only one metal layer can be patterned with this technique. Interconnect crossovers in horizontal and vertical directions would not be possible. For more complicated circuits, other interconnect schemes have to be explored. To enable crossovers with a single level of metal, R. Bhattacharya et al. demonstrated that an X-Y interconnect matrix could be made by a revised lift-off method (Fig. 6.4) [50]. Interconnect islands were added to the existing design and patterned with the device islands. The crossover is made using a buried metal layer embedded in the interconnect islands, not in the deformed inter-island region. This is made before deformation using a conventional process. After the device fabrication, a sacrificial layer of photoresist could be patterned by conventional photolithography on the flat substrate. The substrate was then deformed to a spherical dome. An aluminum layer was thermally evaporated on the dome after deformation, and then patterned by lift-off through stripping the photoresist. Long interconnect lines (~ 58 mm long) across the substrate could be achieved by this method [50].

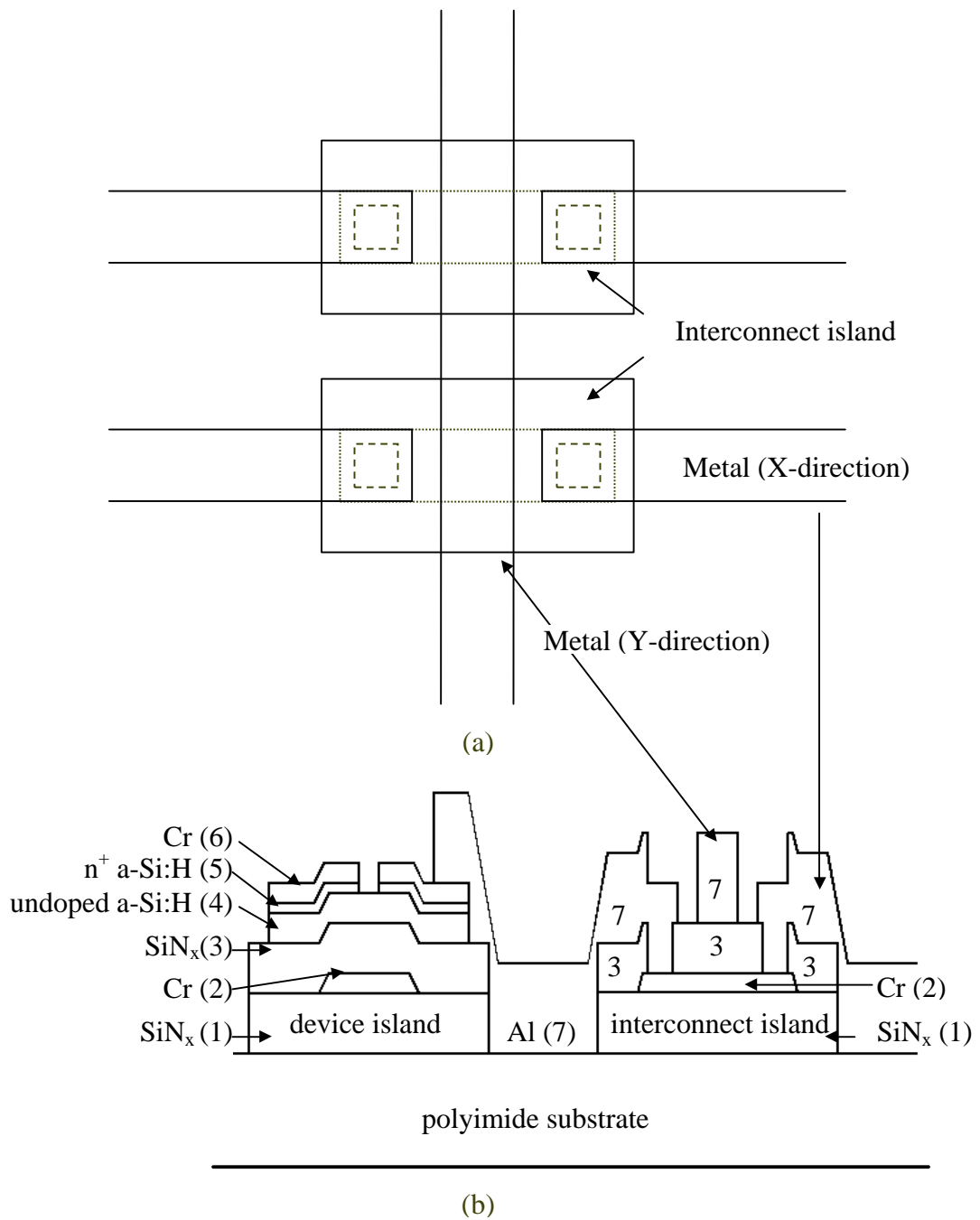


Fig. 6.4 X-Y interconnect matrix. (a) top-view, and (b) cross-section of a device island connected with an interconnect island. The Al layer (7) is evaporated after the substrate deformation and patterned by lift-off method [50].

### 6.3.2 Direct Printing onto Spherical Surfaces

Many groups are today exploring printing techniques for lithography or direct deposition of patterned semiconductor- or polymer-based devices [51]. The central goal of printing as it relates to device fabrication is to create low cost methods for fabricating microstructures on large area substrates. It is possible to print directly on a spherical dome for pattern definition such as the patterning of metal layers using a letterpress technique [52]. This technique used a topologically patterned printing plate. The ink (polystyrene in this case) was deposited onto the raised features by bringing them into contact with a molten polystyrene layer. When the printing plate is pulled away, it is “wetted” with polystyrene. In this way, the process resembled rubber-stamping, with the resolution improved by several orders of magnitude [53]. In the results described here [52], the letterpress stamps were made on a polyimide substrate with mesa structures (substrate etched by oxygen plasma) as the raised features of the stamp. We first deformed a polyimide substrate into the shape of a spherical cap as the target workpiece. We then made a hole at the apex of this cap to allow air to escape during the subsequent printing step (although this step would not be necessary if the process were done in vacuum), as shown in Fig. 6.5(a). Next, the pre-inked letterpress stamp was loaded into the deformation apparatus with the raised features facing up. The spherical workpiece was placed above the stamp, with the concave side facing down, and the two were clamped in position. The printing was accomplished, as illustrated in Fig. 6.5(b), by increasing the air pressure on the stamp’s lower surface to achieve contact at the apex of the workpiece, which was observed to be the last point of contact. The sample was then heated to transfer the polymer ink. The air pressure was decreased and the surfaces

spontaneously separate as the elastic part of the stamp deformation relaxes. A spherically deformed stamp can be reused by re-applying ink with the same process used for printing, replacing the workpiece with a polymer-ink coated foil. S. Miller et al. applied this letterpress technique described above for sphere-to-sphere printing with a target polyimide workpiece coated with 10 nm Cr (for adhesion) and 90 nm Au, and reported that the printed polystyrene films were good resists for both wet chemical etching and reactive ion etching (RIE). 20 x 20  $\mu\text{m}$  gold islands could be patterned by this technique [53]. Though further work is necessary to develop methods for alignment of the mask and existing features on the target workpiece, it indicates that direct printing is a promising approach for patterning electronics with 3-D shapes.

### 6.3.3 Stretchable Interconnects

In Section 6.2, the substrate was deformed to a 3-D shape only once. For applications such as e-textiles, the device/substrate structure has to withstand stretching-then-relaxing many times. S.P. Lacour et al. proposed a reversibly stretchable interconnect scheme, which consists of thin, wavy metal lines (Au) on polydimethylsiloxane (PDMS) substrates [54]. These metal lines were of sinusoidal shape (100 nm thick, 0.25 mm wide, and 22 mm in total length), and the substrate was 1 mm thick. The substrate was then constantly stretched, and the resistance was measured in situ. The results showed that these thin gold films retain electrical conduction at elongation up to ~22%. Though the mechanism behind such stretching was not yet understood, it demonstrated another promising approach for stretchable interconnects.

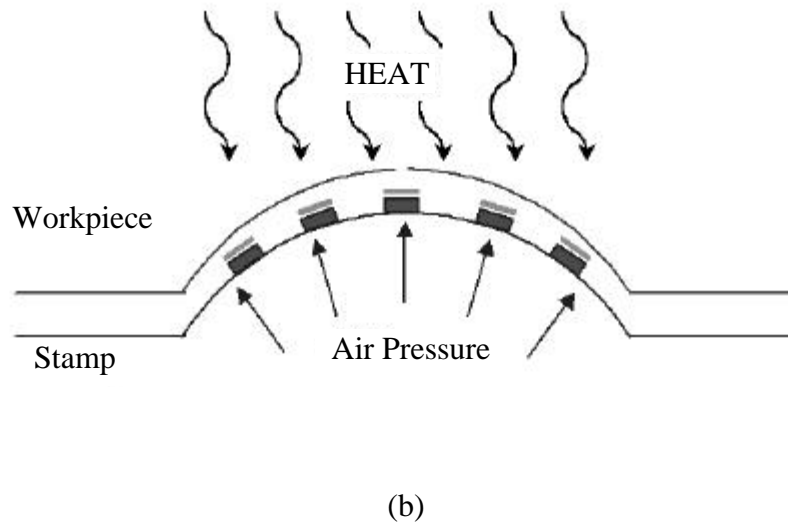
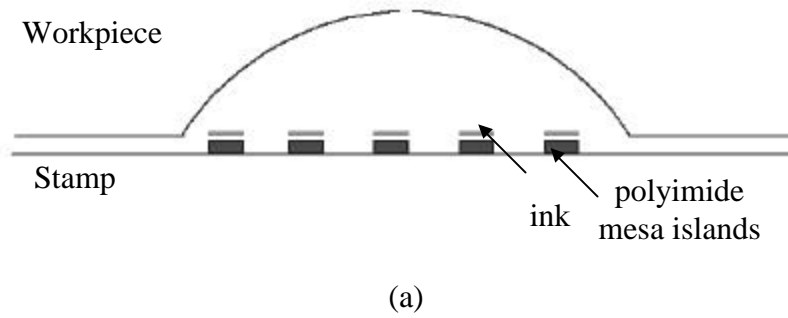


Fig. 6.5 Schematic of the spherical printing process. (a) The workpiece and stamp prior to printing; the air release hole is indicated at the apex. (b) The workpiece and stamp during printing. In both panels the workpiece and stamp are in contact at the edges, the separation illustrated is only for graphical clarity [52].

## 6.4 Chapter Summary

To achieve electronics on a spherical dome, thin-film transistors were fabricated by first making the devices with conventional processes in islands on a flat polyimide substrate and then plastically deformed the substrate into a spherical dome. With this approach, the strain in the device island was greatly reduced. However, since the deformation took place mostly in the region between islands, the tensile strain was concentrated in the inter-island regions. Metal interconnect lines made before deformation would fracture during deformation. One solution to overcome this difficulty is to deform the substrate with pre-patterned photoresist, and evaporate the metal layer after the deformation. Simple circuits could be made after photoresist removal (lift-off). In this chapter, we also discussed other interconnect schemes such as direct printing. It demonstrated that it is possible to overcome the mechanical limitation to achieve 3-D electronic surfaces.

# Conclusion

## 7.1 Summary

The applications of traditional large-area electronics are limited by the fact that glass substrates are rigid and easily breakable. Future large-area electronics applications, such as electronic paper, sensor skin, and electrotiles, require building electronic devices on flexible and deformable substrates. One major challenge is that while substrates (for example, organic polymers and stainless steel foils) can be deformed into arbitrary shapes, inorganic semiconductor device materials, such as amorphous silicon and silicon nitride, are brittle, and crack easily when substrates are deformed. Therefore, to achieve electronics on surfaces with arbitrary shapes, it is crucial to reduce the strain in the devices. The most common type of deformation is to roll a thin foil substrate into a cylinder. For such deformation, the strain in any devices on the substrate or foil surface can be minimized by using thin substrates. Previous work [12,16] has demonstrated that transistors on thin metal or plastic foil substrates can be rolled around a cylinder down to 2-mm radius of curvature with no adverse effects.

In this thesis we explored the feasibility of building electronics on surfaces with three-dimensional shapes. Our approach was to fabricate first on flat substrates, and then permanently deform the final device structure, using pressurized nitrogen, into a spherical dome subtending up to  $\sim 66^\circ$  field-of-view (one steradian). Annealed stainless steel and plastic sheets are suitable candidates for the substrate materials because they can easily be plastically deformed. In contrast to rolling, with spherical deformation, the surface is in tension on both the concave and convex sides of the substrate and thinning the substrate cannot be used to significantly reduce the strain. Consequently, blanket device layers such as silicon or silicon nitride fractured after substrate deformation. By patterning amorphous silicon and silicon nitride layers into islands, such problems can be avoided despite average strains in the substrate in excess of 5%, and isolated device islands could remain fracture-free after substrate deformation.

The strain in the island increases with the island size, but is only weakly dependent on island density when the substrate is soft. We presented two device structures: TFTs in planar islands and TFTs in mesa islands. Planar islands were in tension like the substrate. Deep mesa islands were created by etching into the substrate underneath the hard device islands. These mesa islands could actually be in compression even if the overall substrate strain was as high as 5% tension. The TFTs are still well-behaved after substrate deformation, and the off-current and gate leakage current do not change substantially. The mobility of TFTs in 40- $\mu\text{m}$  planar islands increased  $\sim 8\%$  after substrate deformation, but the mobility of TFTs in 40- $\mu\text{m}$  mesa islands decreased  $\sim 12\%$  after substrate deformation and demonstrated a linear trend with island size. The sign and magnitude of the change in the mobility of a-Si TFTs tracked the sign and magnitude

of the island strain, with compression leading to a lower mobility and tension to a higher mobility. Our work demonstrates that it is possible to fabricate devices with structures less sensitive to substrate deformation so that the device endures little or no strain even if the substrate is expanded. The concept of controlling and tuning the strain and its sign (either tension or compression) during deformation will be useful for other smart materials and devices in electronic skins.

Interconnects between the device island could be made by depositing metal after deformation and patterning it by lift-off methods with photoresist patterned before deposition. Novel interconnect schemes such as direct printing are also promising approaches for fabricating circuits on substrates with spherical dome shapes. The results demonstrate that the concept of stiff circuit islands fabricated on deformable foil substrates is a promising approach to achieve electronics on surfaces with arbitrary shapes.

## 7.2 Future Work: Active Matrix Display or Sensor Arrays on Arbitrary Shaped Surfaces

Displays and sensor arrays are made of pixels. In an active-matrix addressing scheme, each pixel has a switch and a device for the pixel function. Amorphous silicon TFTs are the most common switching elements in these two applications. For optical sensor arrays, the pixel device could be a photodiode [32]. Fig 7.1 shows a basic image sensor pixel, which consists of an a-Si:H TFT and a p-i-n photodiode. The horizontal lines provide the data and bias connections, and the vertical select line is connected to the TFT gate. The TFTs hold the charge on the pixel when the TFT is off and allow rapid charge

transfer to the data lines when the TFT is on. From Chapter 4, we learned that by patterning uniform semiconductor layers into isolated islands, islands could remain crack-free after substrate deformation. Fig. 7.1 shows a cross-section of one structure for integrating a sensor pixel with photodiode and TFT on a single island. It is also possible to fabricate interconnects between the pixels by the x-y interconnect method described in Fig. 6.4. Therefore, achieving optical sensor arrays on arbitrary shaped surfaces should be entirely feasible.

An active-matrix display pixel is similar to the sensor pixel, but the photodiode is replaced by devices such as liquid crystals or light-emitting diodes (LEDs) [12,55]. Similarly, as long as we can fit the entire pixel onto a single device island, it should be possible to fabricate active-matrix displays on three-dimensional surfaces. Organic LEDs (OLEDs) might soon replace liquid crystals as the leading technology in panel display applications because they have sufficient brightness, wide viewing angle, and full color range. Most importantly, they can be fabricated on compliant substrates [56]. It makes the OLED display lightweight and flexible [57,58]. It has already been demonstrated that OLED display or OTFTs circuits can be rolled into a cylindrical shape [2,3]. Organic pixels consisting of organic TFT switching elements and organic LEDs might be a promising starting point to achieve flexible displays on three-dimensional surfaces. However, the challenges remain. For example, assuming a transparent substrate, the lower electrode of the OLED (typically the anode) should be transparent so that the light can be emitted. If the substrate is not transparent, a transparent top electrode must be used. (Similarly, the top electrode of the sensor photodiode in Fig. 7.1 has to be transparent in order to detect the incoming illumination). The most common materials

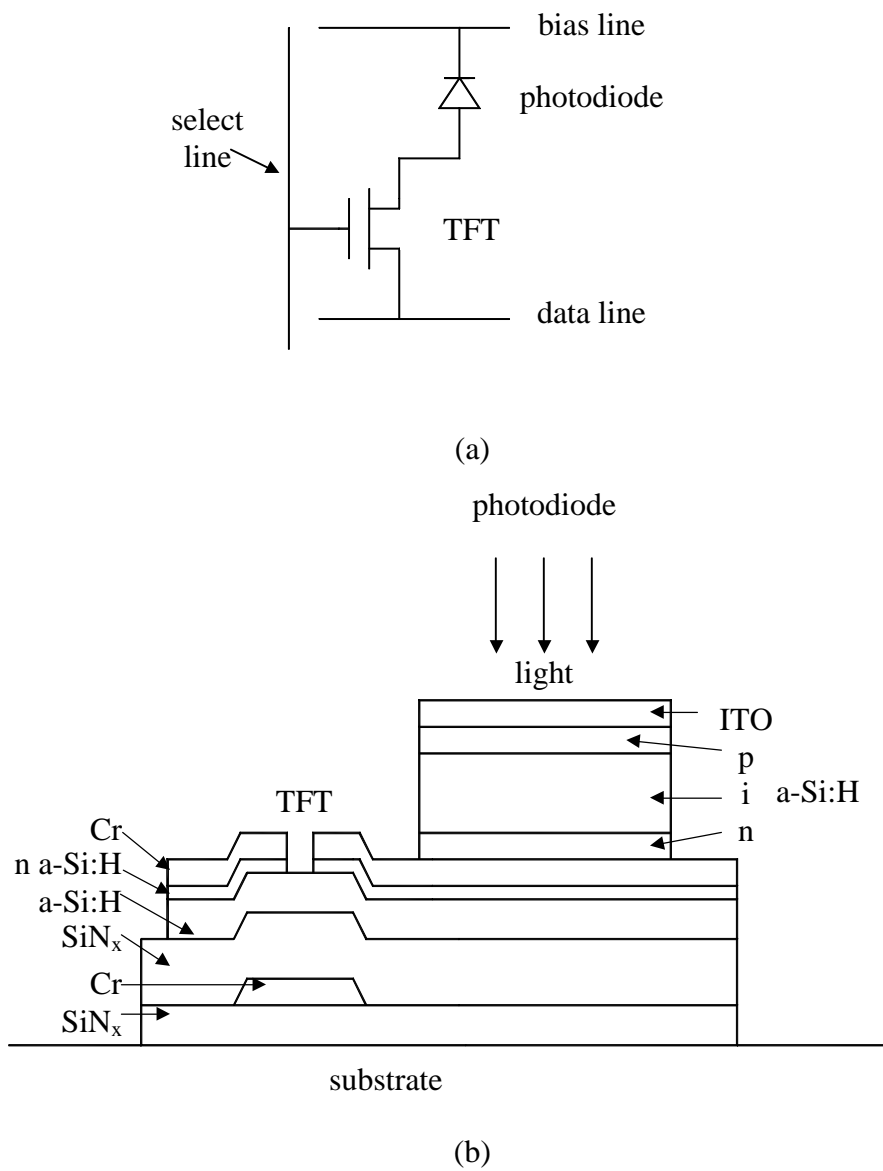


Figure 7.1 (a) Schematic diagram demonstrating a basic image sensor pixel consisting of a TFT and a p-i-n light sensor. (b) Schematic cross-section of the sensor pixel.

for this layer are transparent conducting oxides such as indium tin oxide (ITO). However, ITO is brittle [59]. It cracks when the applied tensile strain is greater than  $\sim 1$  % [60]. Further investigation on soft conducting polymers is required [61].

From this thesis, we learned that the first step towards electronics on arbitrary shapes is to reduce the strain in the device structure. We are confident that an active-matrix display or sensor arrays on arbitrarily shaped surfaces could be achieved in the near future.

# Bibliography

---

- [1] Y. Chen, J. Au, P. Kazlas, A. Ritenour, H. Gates, and M. McCreary, “Flexible active-matrix electronic ink display,” *Nature*, vol. 423, pp. 136, 2003.
- [2] <http://www.universaldisplay.com/foled.php>
- [3] H. Klauk, D.J. Gundlach, J.A. Nichols, C.D. Sheraw, M. Bonse, and T. N. Jackson, “Pentacene organic thin-film transistors and ICs,” *Solid State Technol.*, vol. 43, pp. 63-77, 2000.
- [4] V.J. Lumelsky, M.S. Shur, and S. Wagner, “Sensitive skin,” *IEEE Sensors J.*, vol. 1, pp. 41-51, 2001.
- [5] H. Gleskova, and S. Wagner, “Failure resistance of amorphous silicon transistors under extreme in-plane strain,” *Appl. Phys. Lett.*, vol. 75, pp. 3011-3013, 1999.
- [6] Z. Suo, E.Y. Ma, H. Gleskova and S. Wagner, “Mechanics of rollable and foldable film-on-foil electronics,” *Appl. Phys. Lett.*, vol. 74, pp. 1177-1179, 1999.
- [7] I. Sample, “An all-around better camera,” *New Scientist Mag.*, vol. 170, pp. 23, 2001.
- [8] N. Takeda, “Ball semiconductor technology and its application to MEMS,” *IEEE Micro Electro Mechanical Systems Proc.*, pp. 11-16, 2000.
- [9] L. Wang, D.G. Ast, P. Bhargava, and A.T. Zehnder, “Curved silicon electronics,” *Mater. Res. Soc. Symp. Proc.*, vol. 769, pp. H2.8.1-H2.8.9, 2003.

- [10] Y. Chen, J. Au, P. Kazlas, A. Ritenour, H. Gates, and J. Goodman, "Ultra-thin, high-resolution, flexible electronic ink displays addressed by a-Si active-matrix TFT backplanes on stainless steel foil," *Tech. Dig. Int. Electron Devices Meet.*, pp. 389-392, 2002.
- [11] J. Engel, J. Chen, C. Liu, B.R. Flachsbar, J.C. Selby, and M.A. Shannon, "Development of polyimide-based flexible tactile sensing skin," *Mater. Res. Soc. Symp. Proc.*, vol. 736, pp. D4.5.1-D4.5.6, 2003.
- [12] E.Y. Ma, S.D. Theiss, M.H. Lu, C.C. Wu, J.C. Sturm, and S. Wagner, "Thin film transistors for foldable displays," *Tech. Dig. Int. Electron Devices Meet.*, p. 535-538, 1997.
- [13] A. Constant, S.G. Burns, H. Shanks, C. Gruber, A. Landin, D. Schmidt, C. Thielen, F. Olympie, T. Schumacher, J. Cobbs, "Development of thin film transistor based circuits on flexible polyimide substrates," *Electrochem. Soc. Proc.*, Vol. 94-35, pp.392-400, 1994.
- [14] D.B. Thomasson, M. Bonse, J.R. Huang, C.R. Wronski, T.N. Jackson, "Tri-layer a-Si:H integrated circuits on polymeric substrates," *Tech. Dig. Int. Electron Devices Meet.*, pp. 253-256, 1998.
- [15] P. Mach, S.J. Rodriguez, R. Nortrup, P. Wiltzius, and J.A. Rogers, "Monolithically integrated, flexible display of polymer-dispersed liquid crystal driven by rubber-stamped organic thin-film transistors," *Appl. Phys. Lett.*, vol. 78, pp. 3592-3594, 2001.

- [16] H. Gleskova and S. Wagner, "Electron mobility in amorphous silicon thin-film transistors under compressive strain," *Appl. Phys. Lett.*, Vol. 79, pp. 3347-3349, 2001.
- [17] <http://www.llnl.gov/IPandC/tech/op2000/08/8k-sil.html>
- [18] Virginia Semiconductor Inc.: 1501 Powhatan Street, Fredericksburg, VA 22401.
- [19] P.I. Hsu, M. Huang, S. Wagner, Z. Suo, and J.C. Sturm, "Plastic deformation of thin foil substrates with amorphous silicon islands into spherical shapes," *Mater. Res. Soc. Symp. Proc.*, vol. 621, Q8.6.1-Q8.6.6, 2000.
- [20] S. Timoshenko and S. Woinowsky-Krieger, *Theory of Plates and Shells*. New York: McGraw-Hill, 1959, ch. 13.
- [21] A. Hermida, "Deflection of Circular Membrane Under Differential Pressure," NASA Tech Briefs, vol. 22, pp. 78, 1998.
- [22] L. Howell, *Compliant Mechanisms*. New York: Wiley, 2001, ch. 2.
- [23] T. Serikawa, and F. Omata, "High-mobility Poly-Si TFT's fabricated on flexible stainless-steel substrates," *IEEE Electron Device Lett.*, vol. 20, pp. 574-576, 2000.
- [24] M. Wu, X.Z. Bo, J.C. Sturm, and S. Wagner, "Complementary metal-oxide-semiconductor thin-film transistor circuits from a high-temperature polycrystalline silicon process on steel foil substrates," *IEEE Trans. on Electron Devices*, vol. 48, pp. 1993-2000, 2002.
- [25] A. Kreuz, S.N. Milligan, and R.F. Sutton, DuPont Films Technical Paper 3/94, Reorder No. H54504
- [26] DuPont Films Technical Paper 8/97, Reorder No. H-38492-2.

- [27] H. Gleskova, S. Wagner, V. Gašparík, and P. Kovác, “150°C amorphous silicon thin-film transistor technology for polyimide substrates,” *J. Electrochem. Soc.*, vol. 148, G370-G374, 2001.
- [28] P.I. Hsu, R. Bhattacharya, H. Gleskova, M. Huang, Z. Xi, Z. Suo, S. Wagner, and J.C. Sturm, “Thin-film transistor circuits on large-area spherical surfaces,” *Appl. Phys. Lett.*, vol. 81, pp. 1723-1725, 2002.
- [29] P.I. Hsu, M. Huang, H. Gleskova, Z. Xi, Z. Suo, S. Wagner, and J.C. Sturm, “Effects of mechanical strain on thin-film transistors on spherical domes,” submitted to *Trans. on Electron Devices*.
- [30] ABAQUS, Version 5.8, Hibbitt, Karlsson & Sorensen, Inc., Rhode Island, 1999.
- [31] F. Jansen and M.A. Machonkin, “Thermomechanical properties of glow discharge deposited silicon and silicon oxide films,” *J. Vac. Sci. Technol. A*, vol. 6, pp.1696, 1988.
- [32] R.A. Street, “Large area electronics, applications and requirements,” *Phys. Stat. Sol. (a)*, vol. 166, pp. 695-705, 1998.
- [33] S. Tomiyama, T. Ozawa, H. Ito, and T. Nakamura, “Amorphous silicon thin film transistors and application to image sensors,” *J. Non-Crystalline Solids*, Vol. 198-200, pp. 1087-1092, 1996.
- [34] J.P. Lu, K.V. Schuylenbergh, J. Ho, Y. Wang, J.B. Boyce, and R.A. Street, “Flat panel imagers with pixel level amplifiers based on polycrystalline silicon thin-film transistor technology,” *Appl. Phys. Lett.*, vol. 80, pp. 4656-4658, 2002.

- [35] K.S. Karim, A. Nathan, and J.A. Rowlands, "Amorphous silicon active pixel sensor readout circuit architectures for medical imaging," *Mater. Res. Soc. Symp. Proc.*, vol. 715, A4.2.1-A4.2.6, 2002.
- [36] M. Shur and M. Hack, "Physics of amorphous silicon based alloy field-effect transistors," *J. Appl. Phys.*, vol. 55, pp. 3831-3842, 1984.
- [37] M. J. Powell, "The physics of amorphous-silicon thin-film transistors," *IEEE Trans. on Electron Devices*, vol. 36, pp. 2753 -2763, 1989.
- [38] S. Sherman, S. Wagner, and R.A. Gottscho, "Correlation between the valence- and conduction-band-tail energies in hydrogenated amorphous silicon," *Appl. Phys. Lett.*, vol. 69, pp. 3242-3244, 1996.
- [39] R. B. Wehrspohn, S.C. Deane, I.D. French, I. Gale, J. Hewett, M.J. Powell, and J. Robertson, "Relative importance of the Si-Si bond and Si-H bond for the stability of amorphous silicon thin film transistors," *J. Appl. Phys.*, vol. 87, pp. 144-154, 2000.
- [40] C.S. Yang, L.L. Smith, C.B. Arthur, and G.N. Parsons, "Stability of low-temperature amorphous silicon thin film transistors formed on glass and transparent plastic substrates," *J. Vac. Sci. Technol. B*, Vol. 18, pp. 683-689, 2000.
- [41] H. Gleskova, and S. Wagner, "DC-gate-bias stressing of a-Si:H TFTs fabricated at 150°C on polyimide foil," *IEEE Trans. on Electron Devices*, vol. 49, pp. 1667-1671, 2001.
- [42] P.I. Hsu, H. Gleskova, M. Huang, Z. Suo, S. Wagner, and J.C. Sturm, "Amorphous Si TFTs on Plastically-Deformed Spherical Domes," *J. Non-Crystalline Solids*, Vol. 299-302, pp. 1355-1539, 2002.

- [43] M. Utsunomiya, and A. Yoshida, "Effect of mechanical strain on electrical characteristics of hydrogenated amorphous silicon junctions," *J. Appl. Phys.*, vol. 66, pp. 308-311, 1989.
- [44] R. Jones, T. Johnson, W. Jordan, S. Wagner, J. Yang and S. Guha, "Effects of mechanical strain on the performance of amorphous silicon triple-junction solar cells," *29th IEEE Photovoltaic Specialists Conf. Proc.*, pp. 1214-1217, 2002.
- [45] H. Gleskova, S. Wagner, W. Soboyejo, and Z. Suo, "Electrical response of amorphous silicon thin-film transistors under mechanical strain," *J. Appl. Phys.*, vol. 92, pp. 6224-6229, 2002.
- [46] W.E Spear, and M. Heintze, "The effects of applied and internal strain on the electronic properties of amorphous silicon," *Phil. Mag. B*, vol. 54, pp. 343-358, 1986.
- [47] B. Welber, and M.H. Brodsky, "Optical absorption in amorphous Si films at high pressure," *Phys. Rev. B*, vol. 16, pp. 3660-3664, 1977.
- [48] S. Sherman, P.Y. Lu, R.A Gottscho, and S. Wagner, "TFT performance-material quality correlation for a-Si:H deposited at high rates," *Mat. Res. Soc. Proc.*, vol. 377, pp. 749-753, 1995.
- [49] R. B. Wehrspohn, S. C. Deane, I. D. French, I. G. Gale, M. J. Powell, and R. Brüggemann, "Urbach energy dependence of the stability in amorphous silicon thin-film transistors," *Appl. Phys. Lett.*, vol. 74, pp. 3374-3376, 1999.
- [50] R. Bhattacharya and S. Wagner, "Island edge coverage by metal interconnects for three dimensional circuits," *Mat. Res. Soc. Proc.*, vol. 769, pp. H.10.5.1-H.10.5.6, 2003.

- [51] J.C. Sturm, P.I. Hsu, M. Huang, H. Gleskova, M. Wu, R. Bhattacharya, S.M. Miller, A. Darhuber, S. Wagner, Z. Suo, and S.M. Troian, "Technologies for large-area electronics on deformable substrates," *Electrochem. Soc. Proc.*, vol. 2001-2, pp. 506-517, 2001.
- [52] J.C. Sturm, P.I. Hsu, S.M. Miller, H. Gleskova, A. Darhuber, M. Huang, S. Wagner, S.M. Troian, and Z. Suo, "Three-dimensional electronic surfaces," *Mat. Res. Soc. Proc.*, vol. 636, pp. D11.4.1-D11.4.12, 2000.
- [53] S.M. Miller, S.M. Troian and S. Wagner, "Direct printing of polymer microstructures on flat and spherical surfaces using a letterpress technique," *J. Vac. Sci. Technol. B*, vol. 20, pp. 2320-2327, 2002.
- [54] S.P. Lacour, S. Wagner, Z. Huang, and Z. Suo, "Stretchable gold conductors on elastomeric substrates," *Appl. Phys. Lett.*, vol. 82, pp. 2404-2406, 2003.
- [55] E. Lueder, "Trends of research in active addressing of LCDs," *Mat. Res. Soc. Proc.*, vol. 377, pp. 847-858, 1995.
- [56] P. E. Burrows, G. Gu, V. Bulovic, Z. Shen, S.R. Forrest, and M.E. Thompson, "Achieving full-color organic light-emitting devices for lightweight, flat-panel displays," *IEEE Trans. on Electron Devices*, vol. 48, pp. 1993-2000, 2002.
- [57] M.G. Kane, J. Campi, M.S. Hammond, F.P. Cuomo, B. Greening, C.D. Sheraw, J.A. Nichols, D.J. Gundlach, J.R. Huang, C.C. Kuo, L. Jia, H. Klauk, and T.N. Jackson, "Analog and digital circuits using organic thin-film transistors on polyester substrates," *IEEE Electron Device Lett.*, vol. 21, pp. 534-536, 2000.
- [58] S.R. Forrest, P.E. Burrows, and M.E. Thompson, "The dawn of organic electronics," *IEEE Spectrum*, vol. 32, pp. 29-34, 2000.

- [59] D.R. Cairns, R.P. Witte II, D.K. Sparacin, S.M. Sachsman, D.C. Paine, G.P. Crawford, and R.R. Newton, "Strain-dependent electrical resistance of tin-doped indium oxide on polymer substrates," *Appl. Phys. Lett.*, vol. 76, pp. 1425-1427, 2000.
- [60] Z. Chen, B. Cotterell, and W. Wang, "The fracture of brittle thin films on compliant substrates in flexible displays," *Engineering Fracture Mechanics*, vol. 69, pp. 597-603, 2002
- [61] W.H. Kim, A.J. Mäkinen, N. Nikolov, R. Shashidhar, H. Kim, and Z.H. Kafafi, "Molecular organic light-emitting diodes using highly conducting polymers as anodes," *Appl. Phys. Lett.*, vol. 80, pp. 3844-3846, 2002.

# Kapton<sup>®</sup> Polyimide Substrate Preparation

## A.1 Substrate Cleaning

1. Cut Kapton<sup>®</sup> polyimide Tab-E substrates into ~ 4.5”x 4.5” squares.
2. Put the substrates on a substrate holder so that each piece is separated during cleaning. Leave the holder and substrates in a stainless steel container.
3. Fill the container with DI water. Drop a few droplets of soap into the container.
4. Heat up the container until water boils.
5. Put the container into ultra-sound bath for 30 minutes.
6. Pour out the soapy water. Rinse the substrates and refill the container with fresh DI water.
7. Repeat step 4 and 5.
8. Repeat step 6 and 7.
9. Pour out the hot water. Refill the container with fresh DI water. Leave the substrates in the container until ready for experiments. Before experiments, use nitrogen gun to carefully blow-dry the substrates.

## A.2 Substrate Lamination

To ensure surface flatness, it is essential to laminate the substrate to a hard piece of support (for example, a piece of silicon wafer or glass substrate) during fabrication. In our experiments, polyimide substrates were first laminated to a piece of 4-inch silicon wafer using GE silicone RTV 6166 as the adhesive layer. It is compatible with our fabrication process, and we could easily peel off the polyimide substrate from the supporting wafer once the fabrication was done. To prepare for the silicone gel mixture:

1. RTV 6166 comes with two components. Weight out equal amounts of the A and B components. With a clean spatula, thoroughly mix A and B components together in a large beaker, scraping the sides and bottom of the beaker carefully to produce a homogeneous mixture.
2. Leave the beaker in a vacuum chamber (25 mm mercury) to remove the entrapped air from the mixture.
3. The silicon gel is ready to use. Note that RTV 6166 has a pot-life of 2 hours in room temperature. It is crucial to finish the substrate lamination in two hours.

To laminate the polyimide substrates to silicon wafers:

1. Use spinner to spin-on the silicone gel onto the supporting silicon wafer. Drop (about the size of a quarter coin) silicone gel onto the center of the wafer and spin (ramp: 500 rpm/sec, speed: 200 rpm, time: 20 seconds).
2. Put the wafer with silicon gel, polyimide substrate in a paper envelope (Fig. A.1), and send the “sandwich” into the laminator.
3. Note that the polyimide substrate has to be bigger than the supporting silicon wafer because the polyimide substrate can shift around during rolling in the

laminator. If the polyimide substrate and the silicon wafer are of the exact same size, the polyimide substrate and the silicon wafer will be “mis-aligned” after lamination, and one edge of the wafer will not be covered with the polyimide substrate while the other edge will have polyimide substrate outside the wafer area.

4. RTV 6166 can be cured in room temperature (in 24 hours). Wait for 24 hours after lamination and carefully cut the extra polyimide substrate to trim it to a 4-inch wafer size.
5. After device fabrication is complete, use a pair of tweezers to slowly peel the polyimide substrate off from the wafer.

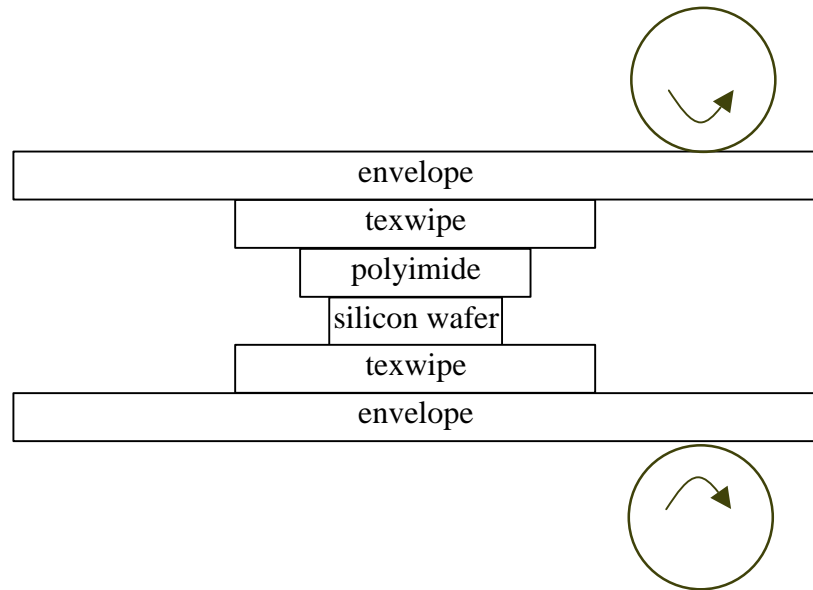


Fig. A.1 The “sandwich” for lamination. The texwipes ensure the surface cleanness of the substrate, and the envelope provides a back support for lamination.

# Recipes for TFT fabrication

## B.1 PECVD Deposition

The recipes below are for the Solarex Model S900 multi-chamber plasma-enhanced deposition system:

Cycle: execution time, in seconds.

Power: RF power in Watts, the forward power minus reflected power.

Pressure: chamber pressure, in mTorr.

The set-point for top-left, top-right, and bottom heaters, is 200 °C. The actual deposition temperature in the chamber after calibration is estimated to be 150 °C.

### B.1.1 360 nm SiN<sub>x</sub> deposition

Step	Descripton	Cycle	Pressure	Power	Ar	H <sub>2</sub>	H <sub>2</sub> dil	SiH <sub>4</sub>	NH <sub>3</sub>
1	Ar flush	120	500		50	-	-	-	-
2	Ar plasma	180		6	50	-	-	-	-
3	H flush	90			-	200	-	-	-
4	SiH <sub>4</sub> flush	120			-	200	20	5	-
5	NH <sub>3</sub> flush	150			-	-	220	5	50
6	Deposition	2400		12	-	-	220	5	50
7	NH <sub>3</sub> flush	60			-	-	220	5	50
8	Pause	10	5		-	-	-	-	-
9	H flush	5	100		-	20	-	-	-
10	H flush	120	500		-	100	-	-	-

### B.1.2 200 nm a-Si:H deposition

Step	Descripton	Cycle	Pressure	Power	Ar	H <sub>2</sub>	H <sub>2</sub> dil	SiH <sub>4</sub>	PH <sub>3</sub>
1	H <sub>2</sub> flush	60	500		-	20	-	-	-
2	SiH <sub>4</sub> flush	120			-	20	-	20	-
3	Deposition	1450		6	-	20	-	20	-
4	SiH <sub>4</sub> flush	120			-	20	-	20	-
5	H <sub>2</sub> flush	120			-	50	-	-	-

### B.1.3 50 nm (n+) a-Si:H deposition

Step	Descripton	Cycle	Pressure	Power	Ar	H <sub>2</sub>	H <sub>2</sub> dil	SiH <sub>4</sub>	PH <sub>3</sub>
1	SiH <sub>4</sub> flush	120	500		-	-	-	50	-
2	PH <sub>4</sub> flush	60			-	-	-	44	6
3	Deposition	750		4	-	-	-	44	6
4	SiH <sub>4</sub> flush	120			-	-	-	50	-
5	H <sub>2</sub> flush 1	10	100		-	20	-	-	-
6	H <sub>2</sub> flush 2	120	50		-	50	-	-	-

## B.2 Reactive Ion Etching

### B.2.1 PlasmaTherm 720 SLR Series RIE System

Thickness in nm, pressure in mTorr, power in Watts, and time in seconds.

Material	Thickness	Gas (sccm)		Pressure	Power	Time
SiN <sub>x</sub>	360	CF <sub>4</sub> (70)	O <sub>2</sub> (10)	100	100	40
a-Si:H	200	SF <sub>6</sub> (60)	CCl <sub>2</sub> F <sub>2</sub> (20)	100	100	180
(n <sup>+</sup> ) a-Si:H	50	O <sub>2</sub> (10)	CCl <sub>2</sub> F <sub>2</sub> (90)	100	100	480
Photoresist	(descum)	O <sub>2</sub> (60)		100	50	600

### B.2.2 PlasmaTherm 790 RIE System

Thickness in nm, pressure in mTorr, power in Watts, and time in minutes.

Material	Thickness	Gas (sccm)		Pressure	Power	Time
Polyimide	8000	O <sub>2</sub> (40)		105	250	20

## B.3 Photolithography

1. Apply photoresist (AZ 5214-E) on substrate.
2. Spinning speed is set to 4000 rpm for 40 seconds. This gives a photoresist coating about ~1.4  $\mu\text{m}$ .
3. Prebake on hot plate at 95°C for 60 seconds.
4. Use Karl Suss MA6 Mask Aligner to expose the sample at 2.5 mW/cm<sup>2</sup> for 30 seconds (hard contact).
5. Develop with AZ-312MIF Developer (diluted 1:1 with DI water) for 60 seconds.
6. Rinse.
7. Postbake at 115°C for 10 minutes in a convection oven.

### Back Support for Spherical Dome Electrical Measurement

To measure the TFTs on a spherical dome, the deformed substrate was mounted on a solid spherical dome with the same shape to provide back support during measurement. This is required because the probe tip can easily deform the soft, hollow dome during measurement when contacting the sample. This solid spherical dome can be made of plaster.

1. Mix two parts of dry plaster powder with one part by weight of warm water in a bottle.
2. Shake vigorously for 2 minutes.
3. Flip the deformed spherical dome over and fill the inside of the dome (Fig. C.1)
4. Let plaster dry for an hour.
5. The plaster support has the exact same shape as the deformed spherical dome.

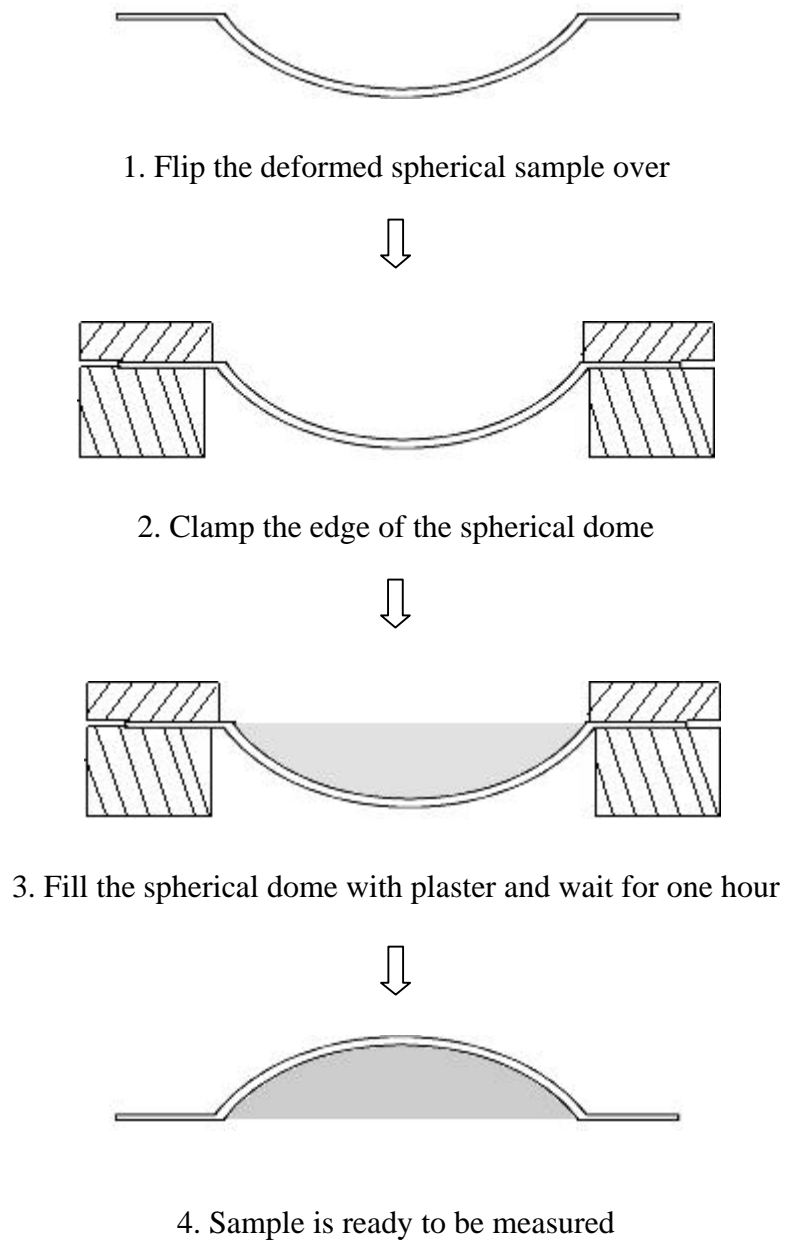


Fig. C.1 Plaster back support for the spherical domes.

# Publications and Presentations Resulting from this Work

## D.1 Publications

- [1] P.I. Hsu, M. Huang, Z. Xi, S. Wagner, Z. Suo, and J.C. Sturm, “Spherical deformation of compliant substrates with semiconductor device islands,” submitted to *J. Appl. Phys.*
- [2] P.I. Hsu, M. Huang, H. Gleskova, Z. Xi, Z. Suo, S. Wagner, and J.C. Sturm, “Effects of mechanical strain on thin-film transistors on spherical domes,” submitted to *IEEE Trans. on Electron Devices*.
- [3] P.I. Hsu, R. Bhattacharya, H. Gleskova, M. Huang, Z. Xi, Z. Suo, S. Wagner, and J.C. Sturm, “Thin-film transistor circuits on large-area spherical surfaces,” *Appl. Phys. Lett.*, vol. 81, pp. 1723-1725, 2002.
- [4] P.I. Hsu, H. Gleskova, M. Huang, Z. Suo, S. Wagner, and J.C. Sturm, “Amorphous Si TFTs on plastically-deformed spherical domes,” *J. Non-Crystalline Solids*, Vol. 299-302, pp. 1355-1539, 2002.

- [5] P.I. Hsu, H. Gleskova, Z. Suo, S. Wagner, and J.C. Sturm, "Amorphous Si TFTs on plastically-deformed substrates with 3-D shapes," *the 59th Device Research Conf. Tech. Dig.*, 2001.
- [6] J.C. Sturm, P.I. Hsu, M. Huang, H. Gleskova, M. Wu, R. Bhattacharya, S.M. Miller, A. Darhuber, S. Wagner, Z. Suo, and S.M. Troian, "Technologies for large-area electronics on deformable substrates," *Electrochem. Soc. Proc.*, vol. 2001-2, pp. 506-517, 2001.
- [7] J.C. Sturm, P.I. Hsu, S.M. Miller, H. Gleskova, A. Darhuber, M. Huang, S. Wagner, S.M. Troian, and Z. Suo, "Three-dimensional electronic surfaces," *Mat. Res. Soc. Proc.*, vol. 636, pp. D11.4.1-D11.4.12, 2000.
- [8] P.I. Hsu, M. Huang, S. Wagner, Z. Suo, and J.C. Sturm, "Plastic deformation of thin foil substrates with amorphous silicon islands into spherical shapes," *Mater. Res. Soc. Symp. Proc.*, vol. 621, Q8.6.1-Q8.6.6, 2000.

## D.2 Presentations

- [1] P.I. Hsu, H. Gleskova, R. Bhattacharya, M. Huang, Z. Xi, Z. Suo, S. Wagner, and J.C. Sturm, "Thin-film transistor circuits on large-area 3-D surfaces," *presented at the 3rd Annual Flexible Microelectronics and Displays Conference, Phoenix, AZ, USA, February 2003.*
- [2] P.I. Hsu, H. Gleskova, R. Bhattacharya, Z. Xi, Z. Suo, S. Wagner, J.C. Sturm, "Thin film transistors on 3-d shapes: electrical performance under mechanical strain," *presented at the 2002 Material Research Society Spring Meeting, San Francisco, CA, USA, April 2002.*

- [3] P.I. Hsu, S. Wagner, H. Gleskova, and J.C. Sturm, "Three dimensional deformable electronic surfaces," *presented at the Center for Photonics and Optoelectronic Materials Annual Review, Princeton University, Princeton, NJ, USA, November, 2001.*
- [4] P.I. Hsu, H. Gleskova, M. Huang, Z. Suo, S. Wagner, and J.C. Sturm, "Amorphous Si TFTs on plastically-deformed spherical domes," *presented at the 19th International Conference on Amorphous and Microcrystalline Semiconductors, Nice, France, August 2001.*
- [9] P.I. Hsu, H. Gleskova, Z. Suo, S. Wagner, and J.C. Sturm, "Amorphous Si TFTs on plastically-deformed substrates with 3-D shapes," *presented at the 59th Device Research Conference, South Bend, IN, USA, June 2001.*
- [5] P.I. Hsu, M. Huang, S. Wagner, Z. Suo, and J. C. Sturm, "Plastic deformation of thin foil substrates with amorphous silicon islands into spherical shapes," *presented at the 2000 Material Research Society Spring Meeting, San Francisco, CA, USA, April 2000.*